University College of Southeast Norway
Faculty of Technology, Natural Sciences and Maritime Sciences
—
Doctoral dissertation Nr 29

Cuong Hung Nguyen

Interdigital-Electrode Thin-Film Piezoelectric Microactuators

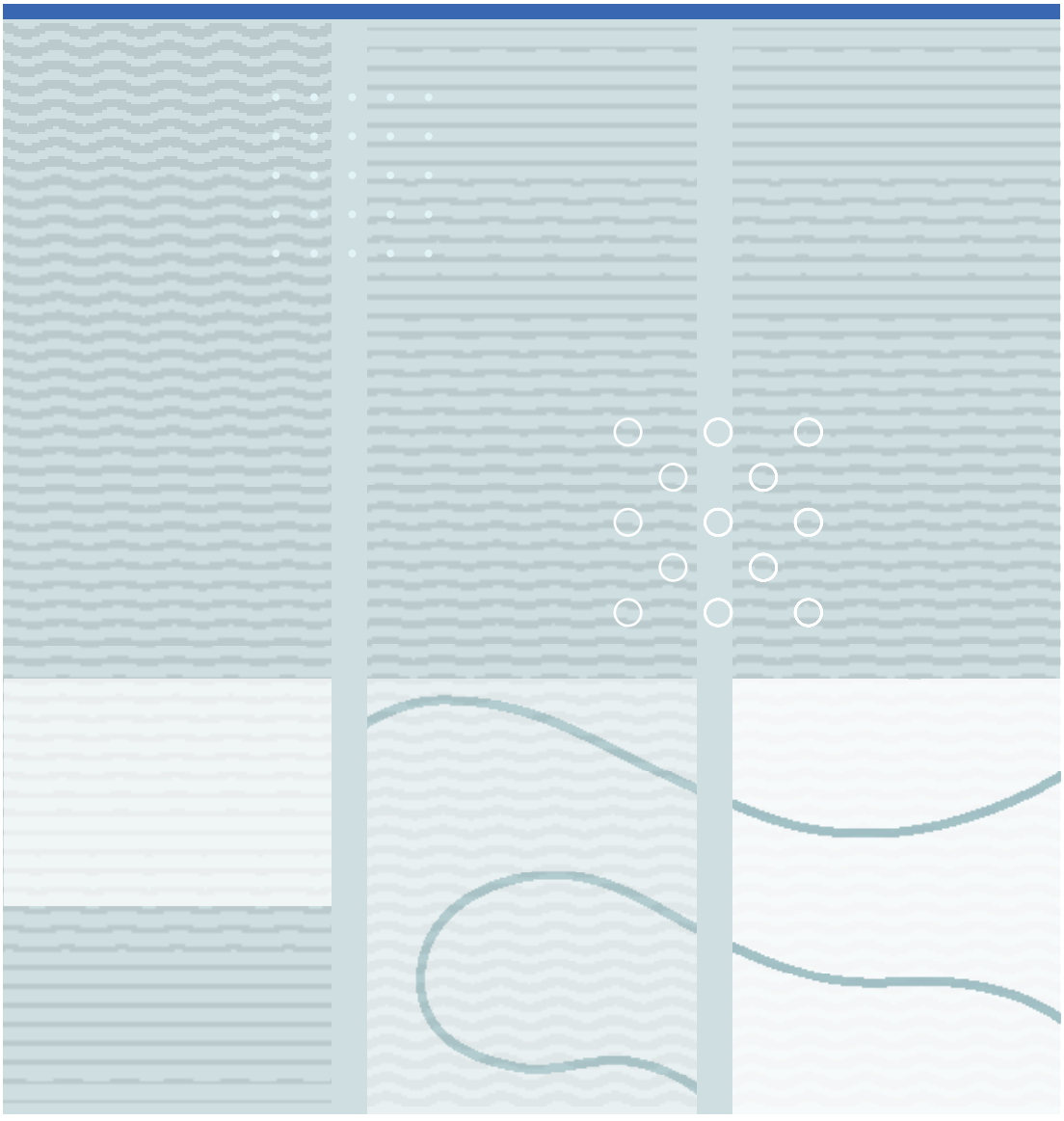

HSN

Cuong Hung Nguyen

Interdigital-Electrode Thin-Film Piezoelectric Microactuators

A PhD dissertation in
Applied Micro- and Nanosystems

Faculty of Technology, Natural Sciences and Maritime Sciences
University College of Southeast Norway
Borre, 2018

Doctoral dissertations at the University College of Southeast Norway no. 29

ISSN: 2464-2770 (print)
ISSN: 2464-2483 (electronic)
ISBN: 978-82-7860-310-9 (print)
ISBN: 978-82-7860-311-6 (electronic)

Print: University College of Southeast Norway

Preface

This thesis is submitted in partial fulfilment of the requirement for the degree of Philosophiae Doctor at the University College of Southeast Norway (USN).

The work has been conducted from September 2014 to September 2017 at the Department of Microsystems, USN, Horten, Norway under supervision of Professor Einar Halvorsen and Professor Ulrik Hanke. I spent the entire period of my PhD studies at USN, except for a two-month period, November - December 2016, when I was at the Electroceramic Thin Film Group at the École Polytechnique Fédérale de Lausanne (EPFL) as a visiting researcher.

The research was supported from the Research Council of Norway under grant number 235210 for the project *Beat the Human Eyes*.

Acknowledgements

I would like to express my sincere gratitude to all those who supported me toward completing this thesis.

First and foremost, my sincere gratitude goes to my supervisors, Professor Einar Halvorsen and Professor Ulrike Hanke. Their expertise and and enthusiasm have inspired my passionate interest in every subject matter. Professor Einar Halvorsen guided me to gain a big picture in research. He provided me great advices and encouragements whenever I had challenges. Professor Ulrike Hanke was care on details. He helped me to recognize and connect important pieces of information. Many discussions on late Friday evening for solving challenges will always my best memories.

I am grateful to all members of the Piezoelectric Devices Group for their useful discussions and presentations, Professor Muhammad N. Akram and Research Fellow Mahmoud A. Farghaly.

I would like to express my appreciation to the Department of Microsystems at the University College of Southeast Norway (USN) for their useful facilities and administrative assistance.

I would like to express my appreciation to Dr. Jon Ulvensøen who have created a great collaboration between USN, NTNU and Polight AS via the Beat The Human Eyes project. In addition, I would like to thank scientists from Polight AS, Dr. Lars Henriksen, Dr. Vladimir Kartashov and Dr. Adriana Cozma for their helpful discussion and support.

My gratitude goes to Professor Paul Mural for providing me a chance to research at the Electroceramic Thin Film Group at the École Polytechnique Fédérale de Lausanne (EPFL), Lausanne, Switzerland. I would like to thank Dr. Robin Nigon for his cooperation.

Finally, I especially thank my family and friends for their sharing, encouragement and motivation. My best appreciation goes to my wife and my little daughter for their love and unconditional support.

Abstract

Along with microsensors, microactuators are the most important components of microelectromechanical systems. Many microactuators use piezoelectric coupling mechanisms because they allow these actuators to generate high levels of force to perform fast switching with low power consumption. Two different coupling are typically used to drive microactuators: the d_{31}-transversal and d_{33}-longitudinal couplings. In practice, a specific coupling is selected through the electrode configuration used in the actuator design, where a top and bottom electrode (TBE) configuration is used for the d_{31} coupling and an interdigitated electrode (IDE) configuration is used for the d_{33} coupling.

Simple considerations indicate that the longitudinal piezoelectric effect is expected to be twice as strong as the transverse effect because the piezoelectric coupling constant d_{33} has a value that is approximately double that of the d_{31} constant for most piezoceramics. However, because of the effects of inhomogeneous electric fields and passive regions that cannot be actuated, the performance of IDE actuators can be worse than that of the TBE type and is difficult to predict. In addition, publications in the literature on the d_{33} coupling are relatively scarce when compared with those on the d_{31} coupling. Therefore, there is a need for greater understanding of the properties of IDE actuators. This thesis thus focuses on the modelling, simulation and characterization of piezoelectric actuators using the IDE configuration. Both beam- and plate-type microactuators are investigated.

Using the linear constitutive relationship of piezoelectricity as a starting point, bending models of these actuators are first established, and a new governing equation is derived for the bending of the beam-type actuator. This governing equation leads to the establishment of a linear two-port model for the transducer. This model of the two-port parameters helps us to understand the effects of the materials electromechanical coupling factor on the transducer's electrical properties, e.g., its capacitance, and its mechanical properties, e.g., stiffness and flexural rigidity. The most challenging aspect of modelling of the IDE transducer is the inhomogeneous electric field. Unlike the case of a normal dielectric without piezoelectricity, the Laplace equation cannot be applied directly to solve for the electric field in this case because the mechanical stress has an additional effect on the electric field. However, if the piezoelectric layer is thin, certain simplifications can be made. We therefore establish suitable models of both the inhomogeneous electric field and the free capacitance. These new models are then used to characterize a thin ferroelectric material. When compared with the current state-of-art characterization methods, more consistent curves are obtained for the ferroelectric material's properties, such as the CV and PV and the stress-field loops. Additionally, we found that while the permittivity of the ferroelectric material is dependent on the electric field, the permittivity distribution can be treated homogeneously.

Finally, circular plate actuators with different electrode configurations, including

top and bottom, interdigitated, spiral, and radial electrodes, are investigated. A comparison of the deflection properties of these different electrode configurations is presented and the IDE and TBE actuators are shown to be the best in terms of bending. In an equal-voltage comparison, the IDE actuators are deflected less than the TBE actuators because of their inhomogeneous electric fields. However, in an equal-field comparison, the IDE actuators can produce higher deflections than the TBE actuators.

Contents

Preface i

Acknowledgements iii

Abstract v

Contents vii

List of Figures ix

List of Tables xiii

1 Introduction 1
- 1 Field of study . . . 1
  - 1.1 Microactuators . . . 1
  - 1.2 Piezoelectric microactuators . . . 4
- 2 Motivation . . . 8
- 3 The IDE configuration . . . 10
- 4 Choice of research area . . . 12
- 5 Thesis outline . . . 13

2 Beam actuators 15
- 1 Modelling of the piezoelectric layered beam . . . 15
  - 1.1 The general form of two-port model . . . 15
  - 1.2 Governing equations . . . 16
- 2 Two-port model of the TBE transducer . . . 18
- 3 Governing equation of d_{33} coupling beams . . . 20
  - 3.1 Governing equation . . . 20
  - 3.2 Case studies . . . 22
- 4 Two-port model of the IDE transducer . . . 23
- 5 Deflection of the piezoelectric layered beam . . . 26
  - 5.1 Comparison between piezoelectric beams with the TBE and IDE configurations . . . 26
  - 5.2 Discussion . . . 29
- 6 Effect of the non-uniform field on the IDE beam . . . 30
  - 6.1 Capacitance model in an anisotropic piezoelectric material . . . 31
  - 6.2 Electric field and coupling constant for the symmetric IDE configuration . . . 34
  - 6.3 Capacitance model for the the asymmetric IDE configuration . . . 38
- 7 Electromechanical coupling factor of the TBE and the IDE transducers 41

7.1 TBE beam . . . 42
7.2 IDE beam . . . 44
7.3 Comparison between TBE and IDE . . . 44
8 Characterization of the thin PZT film with IDE . . . 45
8.1 Analysis of the IDE devices with homogeneous dielectric distribution . . . 46
8.2 Results . . . 52
8.3 Inhomogeneous distribution of dielectric . . . 56

3 Plate actuators 63
1 Structural description . . . 63
2 Actuation of the piezoelectric layered plate . . . 63
2.1 Governing equations . . . 63
2.2 Plate with TBE configuration . . . 65
2.3 Plate with d_{33} coupling . . . 69
2.4 Plate with IDE configuration . . . 71
3 Deflection comparison between plate actuators . . . 74
4 Electrode configurations for microactuators . . . 75
4.1 The electrode configurations . . . 75
4.2 Electromechanical performance . . . 77

4 Conclusion 81

Bibliography 83

Appendix 93

List of Figures

1.1 Different concepts for magnetically-based microactuators [28]. (a) The magnetic field is generated by the current in the coil magnetizes and deforms beam. (b) The current in the planar inductor generates a magnetic field and actuates the permanent magnet. (c) The magnetic field from the permanent magnet generates Lorentz force on a current-carrying wire. (d) A magnetostrictive core is displaced due to a magnetic field generated by current-carrying coil. 2

1.2 Different configurations of the thermal microactuators, the arrows show the motion direction. (a) The actuator includes two material with different thermal expansion coefficients [29]. (b) The actuator have several angled beams that expand when heated [30, 31]. (c) The actuator has asymmetric arms to create flexural motion when heated [32]. 3

1.3 Different configurations of the electrostatic microactuators, the arrows show the motion direction. (a) and (b) are gap closing configurations [33--36], (c) and (d) are constant gap configurations [24, 37--40]. . . . 3

1.4 Three common coupling coefficients of PZT (a) d31 coupling, (b)d33 coupling and (c) d15 coupling . The axes on the left show the material coordinate. The black layers are electrode, the gray layer are PZT. The black arrow inside PZT material shows the polarization (P) direction. 6

1.5 Actuator configuration with d_{31} coupling (a) and (b), and with d_{33} coupling (c) and (d). 7

1.6 The piezoelectric based tunable lens configuration [63]. (a) The lens focuses at infinity at 0 voltage. (b) The lens focuses at a finite distance under an applied voltage. (c) The focusing principle of the lens similar to human's eye [64], the actuator acts as the muscle while the polymer acts as the crystalline. 9

2.1 Piezoelectric layered cantilever with d_{31} (a) and d_{33} (b) coupling. The arrows inside the piezoelectric layer (plotted in grey) show the direction of the polarization. 16

2.2 Cross section of layered beam structure. An example of the TBE device with M layers. 17

2.3 The potential V is applied to kept electric field strength at $E =$ 1MV/m in both case of coupling mode and $t_b + t_p = 40\mu$m. 22

2.4 Tip deflection of piezoelectric actuator at different thickness of the substrate and piezoelectric material $t_b/(t_p + t_b)$ and $t_b + t_p = 40\mu$m. . 24

2.5 Homogeneous field distribution assumption inside active regions. . . . 24

2.6 The total electric charge on an electrode is found by integrating the normal component of the electric displacement vector around the contour. 25
2.7 IDE and TBE cantilever actuators comparison. For the IDE, the finger spacings and finger widths are a = b = T/2. The thickness of the piezoelectric layer is t_p = 2um. 27
2.8 TBE (a) and IDE (b) clamped-clamped beam actuators. 28
2.9 IDE and TBE cantilever actuators comparison. For the IDE, the finger spacings and finger widths are a = b = T/2. The transducer length is Ropt = 270um. The thickness of the piezoelectric layer is t_p = 2um. 29
2.10 Inhomogeneous field distribution inside piezoelectric sheet. 30
2.11 Two configurations of the IDE (a) without interconnection lines and (b) with interconnection lines. The dark areas are metal electrodes. . 31
2.12 Capacitance per unit width of the symmetric IDE piezoelectric beam. The finger spacings and finger widths are a = 3b = 3T/4=30um. The thickness of the substrate layer is fixed t_p = 20um. 34
2.13 A representative segment of IDE. The imaginary axis is at the centre of the electrode fingers while the real axis is on the interface between piezoelectric material and the electrodes. 35
2.14 The conformal mapping series [90] to transform the representative segment of the IDE to a parallel strip lines. 36
2.15 Different models of the electric field along the insets dotted line at the middle of the piezoelectric layer 37
2.16 Fitting parameters of the phenomenological quadratic model electric field model (PQ model) with 2D-FEM and CMT model (a) and the comparison between PQ models and CMT (b). 37
2.17 The coupling constant of the symmetric IDE piezoelectric narrow beam with different electric field model. 38
2.18 Conformal mapping flow to transform a polygon into parallel strip lines. 39
2.19 Capacitance C_n is split into two different partial capacitances C_{n1} and C_{n2}. Each of these has uniform polarization direction as it is shown. . 40
2.20 Capacitance per overlap width B of the symmetric - asymmetric IDE device at $g = 5\mu$m. 40
2.21 Capacitance per overlap width B of the asymmetric IDE device with different end gaps g. 41
2.22 Electromechanical coupling factor of the TBE device 42
2.23 Electromechanical coupling factor of the IDE device 44
2.24 Electromechanical coupling factor ratio between the IDE and the TBE transducers 45
2.25 The geometry of the IDE transducer. 46
2.26 Comparison between different capacitance models in case of only a piezoelectric layer (a) and the effect of the SiO_2 layer and the floating electrode on the total capacitance (b). 47
2.27 The electrostatic field inside the dielectric stack is presented. The contour show the equipotential lines. The length and direction of the arrows indicate the strength and direction of the electric field. The simulation is of the FEM model in Fig.2.25 with $a = 4\mu$m and $b = 6\mu$m. 48

2.28 The equivalent circuit (a) and its simplified version (b) of the IDE representative segments. For clarity, in (b), we only show the equivalent electrode for one finger. 49

2.29 The comparison between the analytic (2.110) and FEM model of the total capacitance. (a) Both are normalized with (2.105), (b) Capacitance ratio of (2.110) with the effective electrode width (2.106) to the FEM results 50

2.30 Different normalized models of the electric field at the center of the gap. The structure is shown in the inset, the floating electrode is not taken into account. 51

2.31 Electric field in longitudinal direction. The inset with the cut line of the electric field with $a = 4\mu$m, $b = 6\mu$m 51

2.32 Characteristic curves of the PZT film with the IDE on tops. The raw data is measured and reported in [118]. The arrow direction indicates the increasing gap. In (a) and (b), the curves are with the parallel plate capacitance model (2.105) and $E = V/a$. The parasitic capacitance C_p is not subtracted yet. In (c) and (d), the permittivity are with the simplified Gevorgian model (2.111), the electric field is rescaled to $E = V/(a + \Delta a_1)$, the parasitic capacitance is subtracted by using the fitting method. The Figure (c) and (d) correspond to Fig.15c and Fig.15d in [81]. In (e) and (f), the permittivity are with the simplified Igreja model (2.118), the electric field is rescaled to $E = V/(a + \Delta a_2)$, the parasitic capacitance model C_p (2.107) is used to subtract parasitic contributions. 53

2.33 Characteristic curves of the PZT film with the IDE on tops. The curves are with the simplified Igreja model (2.118) and $E = V/(a+\Delta a_2)$. The parasitic capacitance C_p is subtracted. The arrow direction indicates the increasing gap. 54

2.34 The small signal coupling constant. 55

2.35 The relation between the permittivity and the electric field. 56

2.36 The distribution of the dielectric inside the ferroelectric material for $a = 4\mu$m. The color bar indicates the relative permittivity value. . . . 57

2.37 The relative permittivity and electric field in Fig.2.36 at the material's cut-line as in Fig.2.31 for two different gaps: $a = 4\,\mu$m (a),(b) and $a = 20\,\mu$m (c),(d). 58

2.38 The electric field with $a = 20\mu$m in both cases of homogeneous and inhomogeneous dielectric distribution when the floating electrode is not taken into account. 59

2.39 The capacitance in both cases of homogeneous and inhomogeneous distribution. 59

2.40 The correction factor ϑ for the electric field. The second order polynomial (2.132) (faces) is fitted with the FEM results (black dots). . . 60

2.41 The CV and PV loops of the PZT film with IDE on tops. 60

2.42 The FEM model of the IDE device with piezoelectric coupling coefficient taken into account. The arrow show the direction of the polar axis. 61

2.43 The capacitance per unit width multiplied by the effective gap distance $(a + \Delta a_2)$ of the piezoelectric layer in both cases of zero and non-zero piezoelectric coupling coefficients. The piezoelectric material is treated as homogeneous distribution with the permittivity of $\varepsilon_r\varepsilon_0 = \varepsilon_{33}^T = \varepsilon_{11}^T = 1000\varepsilon_0$. 62

3.1 A circular plate piezoelectric actuator with an IDE electrode configuration. Different color correspond to different material i.e., black: electrodes, grey: piezoelectric layer, blue: diffusion layer and white: elastic substrate. 64
3.2 The circular multi-layered plate with conventional direction in the polar coordinate system 65
3.3 Circular plate actuator with the TBE configuration, the voltage difference between the electrodes is $V_{\rm TBE}$. 66
3.4 (a) Deflection of the TBE actuator at different piezoelectric layer thicknesses = 1 - 4μm and opening radius R_o= 500 μm. (b) The deflection shapes of the TBE actuator at R_i=220μm, the piezoelectric thickness t_p=2μm, the applied potential is $V_{\rm TBE}$ = 2V. 69
3.5 Circular plate actuator with the NPE configuration. The electrodes are patterned on two edges of the piezoelectric layer. The voltage difference $V_{\rm NPE}$ is applied between these electrodes. 70
3.6 Deflection of the NPE actuator at different piezoelectric layer thicknesses t_p=1-4 μm and opening radius R_o= 500 μm. 71
3.7 a) Circular plate actuator with the IDE configuration, the voltage difference between the neighbouring electrodes is $V_{\rm IDE}$. (b) The definition of R_n, R_n is the distance from the center of the plate to the start of the n^{th} gap. 72
3.8 Deflection of the IDE actuator. The piezoelectric layer thickness is t_p=2μm and the pitch is T= 20μm. 74
3.9 Comparison between actuators with different electrode configurations: (a) ratio of maximum deflections between NPE and TBE actuator, the piezoelectric layer thickness is t_p= 2 μm. (b) IDE plate actuator deflection at different gap a=10- 18 μm. The pitch and piezoelectric thickness are fixed at T=20μm and t_p= 2μmm. The IDE deflection has a tendency to approach the NPE deflection when the gap is increased. 75
3.10 Comparison of the maximum deflection between the IDE and TBE actuators at (a) t_p= 2 μm and (b) $0 < t_p \leq 4\mu$m. 76
3.11 (a) Four electrode configurations, (b) The polarization direction inside the spiral configuration, d_{33} coupling, is oriented differently in a same piezoelectric sheet. 76
3.12 Four different polarization regions have uniform poling assumption. . 77
3.13 Centre deflection and curvature at sag vertex for the actuators with different values of the active region N at 1MV/m 78
3.14 Comparison between the actuators with different electrode configuration at different opening radius R_i at 1MV/m. (a) The centre deflection and curvature at sag vertex, (b) The volume change. . . . 79

List of Tables

1.1 The tensor coefficients of some typical piezoelectric material 5
1.2 Comparison between different tunable lens concepts [61] [62] 8

2.1 $PbZr_{0.53}Ti_{0.47}O_3$ parameters calculated from [50--52] 23
2.2 The FOM's pre-factor of different piezoelectric material 30
2.3 Analytic model summary 43

Chapter 1

Introduction

1 Field of study

1.1 Microactuators

Microelectromechanical systems (MEMS), or microsystems, are miniature systems that can perform sensing, signal processing, display, actuation, and control functions [1]. The beginnings of MEMS development dates as far back as the 1950s to the discovery of the piezoresistive effect in silicon and germanium [2]. Starting with the development of strain gauges for use as pressure sensors [3], MEMS technology now has a wide range of different uses, including aerospace, automotive, telecommunications, healthcare and environmental applications. In the future, with the development and associated requirements of the Internet of Things (IoT), the demand for MEMS will continue to increase.

Microsensors and microactuators are the two most notable elements in MEMS. They act as the interfaces between an engineering machine and the physical world. Microsensors detect physical quantities such as thermal, mechanical, chemical, magnetic, and optical signals and convert them into readable signals such as electrical signals. After the development of the first strain gauges for pressure sensing, increasing numbers of commercial microsensors have appeared, such as accelerometers, gyroscopes, microphones and microbolometers. Microactuators use an energy source to create motion for control purposes. Early applications of microactuators required either relatively large-scale movements or mechanical contact with another structure, such as a microrelay [4] or a microrobot [5]. However, the requirements for large-scale movement and/or mechanical contact usually led to reliability problems. Other applications for microactuators at this time were found in microfluidic systems such as microvalves and micropumps [6, 7]. These pioneering applications of microactuators thus faced problems with either their own reliability or use in working environments which are hard to control such as fluidics. Therefore, there were fewer noteworthy commercial events for microactuators when compared with those for microsensors. The first remarkable commercialization of the microactuators was their use in the thermal inkjet printer, which was introduced in 1985 by Hewlett Packard [8]. At present, the optical, acoustic and radio-frequency MEMS are the most prominent application fields for microactuators. Examples of devices in optical MEMS include tunable lenses [9--13], scanning mirrors [14--17], and optical stabilizer systems [18,19]. Devices in the acoustic and radio-frequency MEMS fields include surface acoustic wave (SAW) devices [20, 21], ultrasound devices [22, 23] and resonators [24--27].

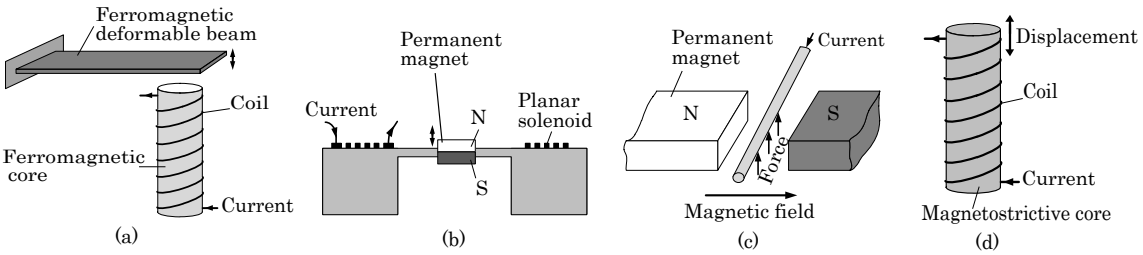

Figure 1.1: Different concepts for magnetically-based microactuators [28]. (a) The magnetic field is generated by the current in the coil magnetizes and deforms beam. (b) The current in the planar inductor generates a magnetic field and actuates the permanent magnet. (c) The magnetic field from the permanent magnet generates Lorentz force on a current-carrying wire. (d) A magnetostrictive core is displaced due to a magnetic field generated by current-carrying coil.

Many of the applications mentioned above have been commercialized successfully. For example, in Norway, the TLens from Polight AS is currently the world's fastest focusing actuated lens. Kongsberg Norspace is a world leading supplier of SAW devices for use in satellite applications and GE Vingmed Ultrasound is a world leader in the production of ultrasound systems for medical applications.

In this study, the types of microactuators that generate acoustic waves are not studied. We focus on microactuators that can generate either a relative structural movement or structural deformation. The operating principles of these microactuators can be classified into the following categories.

Magnetic

In these devices, actuation is generated via interactions among different magnetic elements. These elements can include magnetizable materials, permanent magnets, external magnetic fields, magnetostrictive materials and current-carrying conductors. The principle of the magnetically-based microactuator is dependent on the usage of these magnetic elements. Figure 1.1 shows examples of the different concepts for magnetically-based microactuators.

Thermal

In these devices, actuation is generated via thermal expansion processes. Thermal sources can be generated either electrically by resistive heating or optically using incident light. When heat is supplied, the environment around the heater, which can be composed of solids, liquids or gases, will expand or contract and thus cause the required deformation. Typical thermal actuator configurations for the solid environment are shown in Fig.1.2.

Electrostatic

In these devices, actuation is caused by Coulomb attraction between two oppositely charged bodies or plates. The actuation energy is dependent on the stored energy. If the applied potential is fixed, the stored energy is then directly proportional to the capacitance. Because the capacitance is dimensionally dependent, smaller distances between the charged plates lead to higher capacitance values, and the resulting actuation energy is thus also greater. For this reason, the electrostatic principle

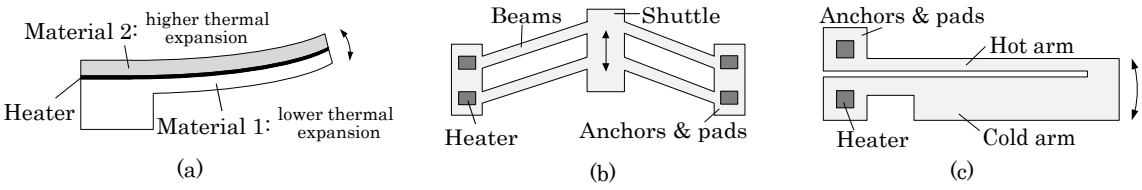

Figure 1.2: Different configurations of the thermal microactuators, the arrows show the motion direction. (a) The actuator includes two material with different thermal expansion coefficients [29]. (b) The actuator have several angled beams that expand when heated [30,31]. (c) The actuator has asymmetric arms to create flexural motion when heated [32].

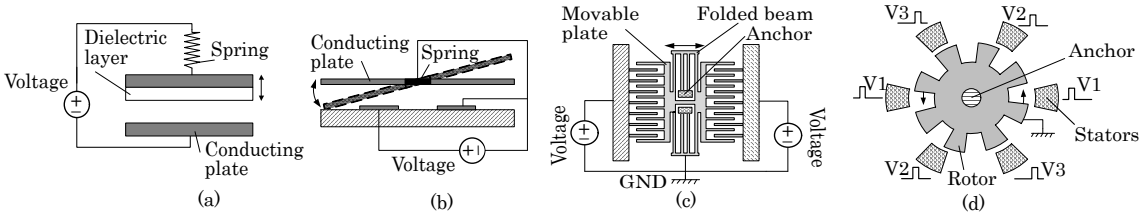

Figure 1.3: Different configurations of the electrostatic microactuators, the arrows show the motion direction. (a) and (b) are gap closing configurations [33--36], (c) and (d) are constant gap configurations [24, 37--40].

is most interesting for application to microscopic-scale devices. Different potential configurations for these devices are shown in Fig.1.3.

Piezoelectric

In these devices, actuation is generated via the piezoelectric effect. Piezoelectricity, which will be discussed more fully in the next section, is a bi-directional effect. Piezoelectric actuation is based on a converse piezoelectric effect that involves the induction of stress and strain under an applied electric field. While the electrostatic principle is largely structurally dependent, piezoelectric actuation is dependent on the piezoelectric material. Different materials can produce different actuation strengths. However, even within the same material, the actuation is also dependent on the direction of the electric field.

In most applications, we would expect a microactuator to offer low energy consumption and reduced fabrication complexity. Additionally, the microactuator must be able to provide high mechanical force, large mechanical displacements and rapid adaptability. It is thus challenging to design a microactuator that can satisfy all these requirements. The designers generally need to make some trade-offs and these trade-offs are usually determined by the application requirements. For example, from an energy consumption perspective, piezoelectric and electrostatic mechanisms consume the least energy. The energy that is supplied to actuate piezoelectric and electrostatic microactuators is stored inside each devices own capacitors. Ideally, these capacitors do not consume energy. In addition, piezoelectric actuation offers fast adaptability. However, the fabrication of piezoelectric microactuators is often a complex process. This is not such a challenge with electrostatic actuators, which are compatible with most conventional fabrication processes. However, electrostatic actuation also provides challenges with its potential for nonlinear behavior and pull-in effects. In addition, electrostatic actuators cannot provide high force output with

low power dissipation [41]. Magnetically-based actuation has been found to provide a more robust mechanism for microactuators when compared with electrostatic actuators [42]. However, it is challenging to implement magnetic actuation at the micro scale [28]. Some thermally-based microactuators such as shape memory alloy (SMA) actuators, state change actuators, and solid or fluid expansion actuators can provide the highest available mechanical force [43]. However, thermal actuators often require high operating temperatures (ranging from 200°C to 600°C) that may be undesirable for more temperature-sensitive applications [44]. A more comprehensive survey of the performances of the different actuation mechanisms for different purposes can be found in [43].

1.2 Piezoelectric microactuators

Piezoelectricity

Piezoelectricity, which is a bi-directional effect, appears in certain classes of crystal symmetry. In one direction, if one of these crystals is mechanically stressed, an electric polarization is produced. This is called the direct piezoelectric effect and was discovered by the Curie brothers in 1880. In the other direction, if we apply an electric field to the same crystal, mechanical stress or strain is created within the crystal. This is called the converse piezoelectric effect. This converse effect was discovered mathematically by Lippman in 1881 and was later experimentally confirmed by the Curies. In other words, piezoelectricity acts as a coupling mechanism between the mechanical domain, i.e., stress and strain, and the electrical domain, i.e., the electric field and electric displacement. This coupling phenomenon can be expressed based on the different forms of the constitutive equations when using matrix notation together with Voigt's notation [45]:

$$\text{d-form:} \quad \begin{pmatrix} \mathbf{S} \\ \mathbf{D} \end{pmatrix} = \begin{pmatrix} \mathbf{s^E} & \mathbf{d} \\ \mathbf{d_t} & \boldsymbol{\varepsilon}^{\mathbf{T}} \end{pmatrix} \begin{pmatrix} \mathbf{T} \\ \mathbf{E} \end{pmatrix}, \tag{1.1}$$

$$\text{e-form:} \quad \begin{pmatrix} \mathbf{T} \\ \mathbf{D} \end{pmatrix} = \begin{pmatrix} \mathbf{c^E} & -\mathbf{e} \\ \mathbf{e_t} & \boldsymbol{\varepsilon}^{\mathbf{S}} \end{pmatrix} \begin{pmatrix} \mathbf{S} \\ \mathbf{E} \end{pmatrix}, \tag{1.2}$$

$$\text{g-form:} \quad \begin{pmatrix} \mathbf{S} \\ \mathbf{E} \end{pmatrix} = \begin{pmatrix} \mathbf{s^D} & \mathbf{g} \\ -\mathbf{g_t} & \boldsymbol{\beta}^{\mathbf{T}} \end{pmatrix} \begin{pmatrix} \mathbf{T} \\ \mathbf{D} \end{pmatrix}, \tag{1.3}$$

$$\text{h-form:} \quad \begin{pmatrix} \mathbf{T} \\ \mathbf{E} \end{pmatrix} = \begin{pmatrix} \mathbf{c^D} & -\mathbf{h} \\ -\mathbf{h_t} & \boldsymbol{\beta}^{\mathbf{S}} \end{pmatrix} \begin{pmatrix} \mathbf{S} \\ \mathbf{D} \end{pmatrix}, \tag{1.4}$$

where $\mathbf{S}$ and $\mathbf{T}$ are 6 by 1 matrices of mechanical strain and stress, $\mathbf{E}$ and $\mathbf{D}$ are 3 by 1 matrices of electric field and electric displacement. Depend on the forms, those matrices are the stimuli to or the responses of the crystal. Their relation is determined by the crystal coefficients, i.e., $\mathbf{s}$ and $\mathbf{c}$ are 6 by 6 elastic matrices, $\mathbf{d}$, $\mathbf{e}$, $\mathbf{g}$ and $\mathbf{h}$ are are 6 by 3 piezoelectric coupling matrices while $\mathbf{d_t}$, $\mathbf{e_t}$, $\mathbf{g_t}$ and $\mathbf{h_t}$ are their transpose, $\boldsymbol{\varepsilon}$ and $\boldsymbol{\beta}$ are 3 by 3 dielectric matrices. The superscript $^{\mathbf{E}}$,$^{\mathbf{D}}$,$^{\mathbf{T}}$ and $^{\mathbf{S}}$ denote the boundary condition of zero $\mathbf{E}, \mathbf{D}, \mathbf{T}$ or $\mathbf{S}$ respectively. For example, $\mathbf{s^E}$ is an elastic compliance matrix of the crystal at the zero electric field condition while $\boldsymbol{\varepsilon}^{\mathbf{T}}$ is the dielectric constant matrix at the zero stress condition.

Each of equations (1.1)-(1.4) is a set of nine equations. Under a given stimulus, the material's response can be known if all the piezoelectric material's coefficient

matrices are given. Not all of these 81 coefficients have independent values. Because of the crystal symmetry, many of the coefficients are zero or are dependent on other coefficients. For example, in a tetragonal crystal with $4mm$ symmetry, the six by three piezoelectric coupling matrices contain only three independent components, and the d-form expansion of this crystal symmetry is given by

$$\begin{pmatrix} S_1 \\ S_2 \\ S_3 \\ S_4 \\ S_5 \\ S_6 \\ D_1 \\ D_2 \\ D_3 \end{pmatrix} = \begin{pmatrix} s_{11}^E & s_{12}^E & s_{13}^E & 0 & 0 & 0 & 0 & 0 & d_{31} \\ s_{12}^E & s_{11}^E & s_{23}^E & 0 & 0 & 0 & 0 & 0 & d_{31} \\ s_{13}^E & s_{23}^E & s_{33}^E & 0 & 0 & 0 & 0 & 0 & d_{33} \\ 0 & 0 & 0 & s_{55}^E & 0 & 0 & 0 & d_{15} & 0 \\ 0 & 0 & 0 & 0 & s_{55}^E & 0 & d_{15} & 0 & 0 \\ 0 & 0 & 0 & 0 & 0 & s_{66}^E & 0 & 0 & 0 \\ 0 & 0 & 0 & 0 & d_{15} & 0 & \varepsilon_{11}^T & 0 & 0 \\ 0 & 0 & 0 & d_{15} & 0 & 0 & 0 & \varepsilon_{11}^T & 0 \\ d_{31} & d_{31} & d_{33} & 0 & 0 & 0 & 0 & 0 & \varepsilon_{33}^T \end{pmatrix} \begin{pmatrix} T_1 \\ T_2 \\ T_3 \\ T_4 \\ T_5 \\ T_6 \\ E_1 \\ E_2 \\ E_3 \end{pmatrix}. \quad (1.5)$$

Here, we follow the IEEE standard on piezoelectricity [45], where the 3-axis is the poling axis of the material. Other crystallographic properties and their constitutive equations can be found in [46]. Table 1.1 lists some of the properties of piezoelectric materials from the literature.

Table 1.1: The tensor coefficients of some typical piezoelectric material

Notation Unit	s_{11}^E	s_{12}^E	s_{13}^E	s_{33}^E	d_{33}	d_{31}	$\varepsilon_{33}^T/\varepsilon_0$	References
		$((\mathrm{TPa})^{-1})$			(pm/V)		1	
AlN	3.53	-1.01	-0.76	3.0	5.53	-2.65	9.5	[47, 48]
ZnO	7.86	-3.43	-2.21	6.94	11.67	-5.43	10.2	[49]
$BaTiO_3$	8.05	-2.35	-5.24	15.7	85.6	-34.5	168	[49, 50]
PZT 5H	16.5	-4.78	-8.45	20.7	593	-274	3400	[49]
PZT 53/47	13.8	-4.07	-5.8	17.1	224.2	-116.7	1180	[50--52]
PZN-PT	82	-28.5	-51.0	108	2000	-970	5200	[53]
PMN-PT	69	-11.1	-55.7	119.6	2820	1330	8200	[54]

A high coupling between the electrical and mechanical domains is important for MEMS devices. Normally, piezoelectric materials with ferroelectricity provide higher coupling than a material with purely piezoelectric properties [55]. Inside the ferroelectric material, connected regions that all have the same polarization are called the ferroelectric domain. If there are no applied fields, these domains are arranged to ensure that the averaged piezoelectric coupling constants are zero. Ferroelectricity enables switching of these electric polarizations using an electric field. In Table.1.1, $BaTiO_3$, lead zirconate titanate (including the varieties PZT-5H and PZT-53/47), lead zinc niobate-lead titanate (PZN-PT) and lead magnesium niobate-lead titanate (PMN-PT) are the ferroelectric materials. Ferroelectricity does not appear in piezoelectric materials such as aluminium nitride (AlN) and zinc oxide (ZnO) because the polarization cannot be re-aligned by application of an electric field in these materials. The alignment should be considered during the manufacturing process.

Single crystal materials such as PZN-PT and PMN-PT have the highest piezoelectric coupling coefficients. These materials have been integrated into devices

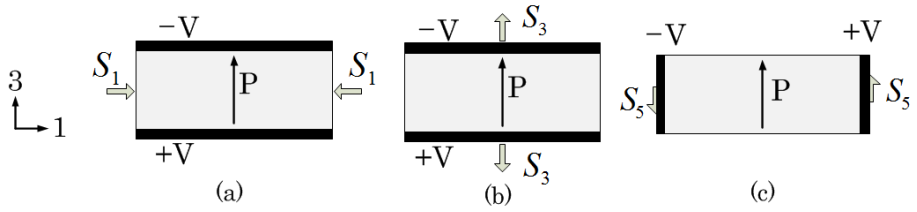

Figure 1.4: Three common coupling coefficients of PZT (a) d31 coupling, (b)d33 coupling and (c) d15 coupling . The axes on the left show the material coordinate. The black layers are electrode, the gray layer are PZT. The black arrow inside PZT material shows the polarization (P) direction.

such as ultrasound transducers to improve the sensitivity and the bandwidth of these devices [56]. However, their major drawback is the significantly high cost because of the manufacturing challenges involved. PZT can provide relatively high coupling coefficients. In addition, manufacturing of the PZT material has much simpler requirements than a single-crystal structure. Therefore, PZT materials are investigated in this study.

Device configuration

In ferroelectric materials, the polarization directions of the ferroelectric domains can be controlled using electric fields. Therefore, in addition to high coupling, devices with ferroelectric materials can also offer flexible configurations.

Most common PZT materials have three independent coupling parameters, i.e., d_{31}, d_{33} and d_{15} as shown in (1.5). Because the 3-axis is the poling axis of the material, the first index denotes the direction of the electric field and the second index denotes the stress/strain component. Figure 1.4 illustrates the directions of the electrical and mechanical fields when the different piezoelectric coupling coefficients are used. The two most commonly used structures in building MEMS devices are beams and plates, and these structures are thus investigated in this study.

d_{31} coupling

The principle of a device with d_{31} coupling is illustrated in Fig.1.4a. The transducer includes a piezoelectric layer that is stacked between top and bottom electrode layers. During or before operation, the piezoelectric layer is poled in the vertical direction. This is also the direction of the applied electric field that is used to induce normal strain/stress along the horizontal direction. Therefore, this case is also referred to as transverse coupling. The advantages of these structures are their simple designs and their ability to induce homogeneous fields inside their active layers. During operation, one disadvantage of the d_{31} coupling actuators is that they produce tensile stress because the ceramic materials are prone to cracking under high tensile stress [57].

Because of the simple structures, many studies have used transverse coupling in their designs. The resulting actuator can be configured using either a simple unimorph configuration or a multimorph configuration. The unimorph structure shown in Fig.1.5a can include multiple elastic layers and a single piezoelectric layer stacked between top and bottom electrode (TBE) layers. The multimorph structure shown in Fig.1.5b can include an arbitrary number of piezoelectric layers. If the

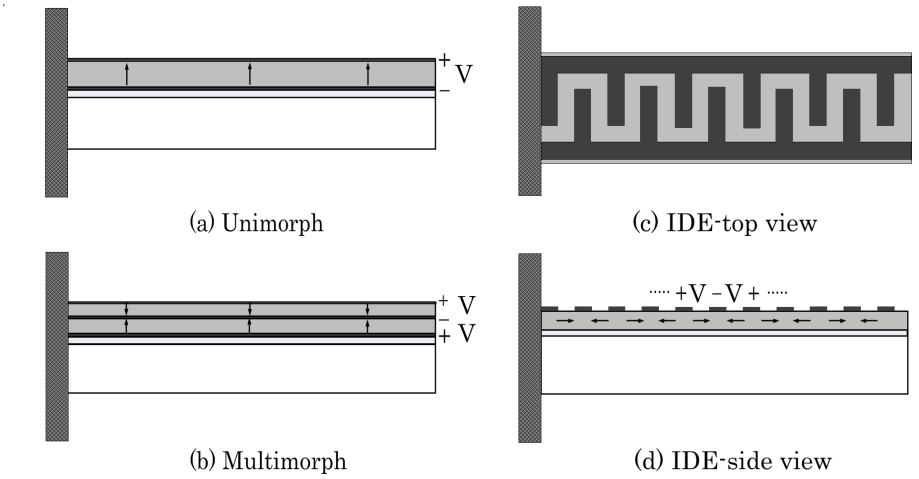

Figure 1.5: Actuator configuration with d_{31} coupling (a) and (b), and with d_{33} coupling (c) and (d).

total thickness of the piezoelectric layers is fixed, the multimorph has the potential advantage of maintaining actuator performance while reducing the applied voltage.

d_{33} coupling

The principle of device operation when using d_{33} coupling is shown in Fig.1.4b. Unlike d_{31} coupling, the polarization, the electric field and the mechanical strain/stress with d_{33} coupling are all oriented in the same direction. Therefore, this type of coupling is also referred to as longitudinal coupling. Based on simple considerations, because the value of the piezoelectric coupling constant d_{33} is approximately double the d_{31} constant for most piezoceramics [50, 58], devices with longitudinal piezoelectric coupling are expected to be twice as strong as the corresponding devices with transverse coupling. During actuation, the compressive stress that is generated by d_{33} coupling can help to prevent cracking of the ceramic materials [57]. However, this coupling requires a much higher actuation voltage than the d_{31} coupling.

The typical device with d_{33} coupling is the type with the interdigital electrode (IDE) configuration shown in Fig.1.5c. Theoretically speaking, the device concept can be configured using both unimorph and multimorph structures. However, multimorph device structures do not appear in the literature because of the fabrication complexity involved. The unimorph structure shown in Fig.1.5d is therefore the most commonly used for these devices.

d_{15} coupling

The principle of device operation with the d_{15} coupling mode is shown in Fig.1.4c. The electric field is applied in the perpendicular direction along with the polarization and the shear strain/stress is generated. While the d_{15} mode has the largest coupling value among the three, thin-film piezoelectric devices with d_{15} coupling are difficult to realize in real structures.

2 Motivation

Many pictures are taken every second worldwide. These pictures may depict the happiest moment in one's life or may show very important information. Many of these moments occur in an instant, and camera users increasingly demand not only to be able to capture the moment but also to be able to take the picture in high definition. This demand can be resolved using electronic cameras with autofocus functions. In optical systems, a tunable lens enables the autofocus function. The typical principles that determine tunability are the relative movement and/or the ability of the optical lens to change shape. The actuator assumes these mechanical roles in the system. Different actuation principles are applied to construct the tunable lens. The voice coil motor (VCM) [59, 60], which was first patented by Alexander Graham Bell in 1874, is considered to be one of the main approaches for tunable lens construction. The magnetic force is used to change the relative position between the optical lens and the objects of interest to adjust the focusing. However, magnetically-based tunable lenses have disadvantages in terms of miniaturization, focusing speed and power consumption. At present, piezoelectric and electrostatic device types are becoming increasingly prominent as solutions to replace the traditional VCM. Many successful prototypes have progressed from laboratory development to the marketplace, with notable names that include Wavelens, Varioptic, Optotune, Apple and Polight. A performance comparison of the piezoelectric, electrostatic and electromagnetic tunable lenses is shown in Table.1.2. As the Table illustrates, the piezoelectric tunable lens can provide the fastest response.

Table 1.2: Comparison between different tunable lens concepts [61] [62]

	Piezoelectric	Electrostatic	VCM
Focusing time	1ms	10ms	5-15ms
Power	5mW	1mW	50-200mW
Size	6 × 6 mm	6.5 × 6.5 mm	8×8 mm
Magnetic Interference	No	No	Yes

In Norway, Polight AS has patented the piezoelectric tunable lens that is shown in Fig.1.6a. This lens consists of a polymer layer that is stacked between a glass support and a glass membrane. A piezoelectric transducer is then deposited on top of the glass membrane. This piezoelectric transducer consists of a thin piezoelectric layer and top and bottom metal electrodes. The transducer must be configured to create radial stress and strain fields when a voltage is applied. Because of the position of the piezoelectric transducer relative to the neutral plane, a strain gradient is created across the thickness of the composite membrane and thus causes the membrane to bend. By controlling the membrane deformation, the tunable focusing function of the lens is then enabled, as shown in Fig.1.6b.

The working principle of the tunable lens shown in Fig.1.6b can be linked with that of the human eye shown in Fig.1.6c. The piezoelectric transducer plays the roles of the ciliary muscles while the polymer acts as the crystalline lens. This 'machine eye' is *relaxed* to focus at infinity if no electric potential is applied; otherwise, the eye is *tensed* to focus at a finite distance. A stronger actuator, which acts as the muscle, leads to a larger bending curvature. The paraxial formula of the plano-convex thin

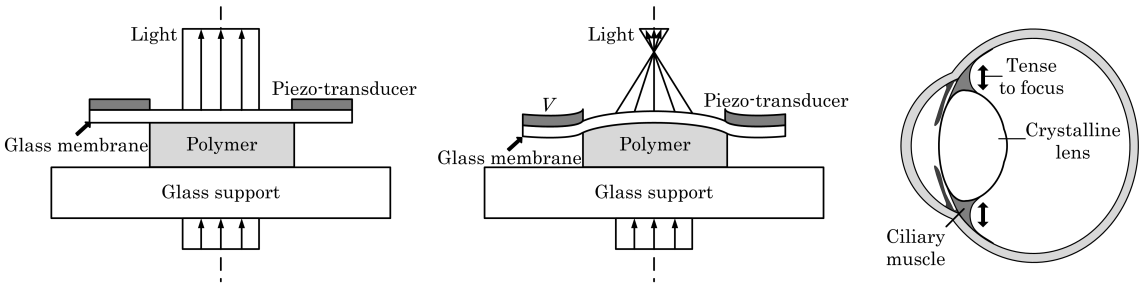

(a) Focus at infinity (b) Focus at a finite distance (c) Human's eye

Figure 1.6: The piezoelectric based tunable lens configuration [63]. (a) The lens focuses at infinity at 0 voltage. (b) The lens focuses at a finite distance under an applied voltage. (c) The focusing principle of the lens similar to human's eye [64], the actuator acts as the muscle while the polymer acts as the crystalline.

lens for its focal length is given by [65]:

$$\frac{1}{f} = (n_g - 1)\rho \tag{1.6}$$

where n_g is the refractive index of the glass and polymer and ρ is the bending curvature, the reciprocal focal length is linearly dependent on the curvature. Therefore, a stronger actuator causes higher lens curvature and thus enables shorter focal lengths.

To construct a stronger actuator, we can either increase the piezoelectric transducer thickness or configure the transducer using a multimorph configuration. The latter solution can potentially help in reducing the applied voltage. However, both solutions require more complex fabrication processes, which are always accompanied by higher costs, and this is not always encouraged in consumer electronics applications. The other solution is to use different piezoelectric coupling coefficients because the value of d_{31} is less than that of d_{33} or d_{15}. For a piezoelectric transducer with d_{15} coupling, the polarization is perpendicular to the electric field shown in Fig.1.4. In a thin film piezoelectric actuator, the polarization can be switched using the applied electric field. Therefore, thin film piezoelectric actuators with d_{15} coupling are difficult to realize. An actuator with d_{33} coupling can be realized with the IDE configuration. Because the piezoelectric coupling constant d_{33} has a value that is approximately two times larger than that of the d_{31} for most PZTs, IDE thin film piezoelectric actuators have been expected to be stronger than conventional TBE actuators. Experimental results [66] have provided motivation for this expectation. In [66], two samples of a single piezoelectric layer were configured with the IDE and TBE layouts. The piezoelectric layer is 190.5μm thick in both samples. Under the same applied electric field, the sample with the IDE configuration produced higher strain than the sample with the TBE configuration. Additionally, the IDE devices required only a single electrode layer on top of the piezoelectric transducer. This configuration thus has the potential to reduce the number of the fabrication processes required. Therefore, the IDE configuration can potentially help to reduce the manufacturing costs. By realizing this potential, attention has been drawn to IDE configurations not only for actuator applications but also for use in other MEMS devices such as accelerometers [67], ultrasound devices [68], and energy harvesters [69]. However, a recent experimental study [57] on cantilever-type actuators concluded that the IDE actuator is no better than the TBE actuator. This is somewhat contrary to previous expectations and shows that further studies are necessary for a greater

understanding of IDE actuators.

The objective of this study is to investigate piezoelectric microactuators based on the interdigitated electrodes concept. The target is to understand and model these IDE-type actuators. We would like to determine whether or not the thin film piezoelectric actuator with the IDE configuration could be a stronger actuator than the corresponding TBE-type actuator and establish if it is possible for this configuration to be implemented as part of the next generation of tunable optical lenses.

3 The IDE configuration

The IDE configuration was introduced by Tesla in 1891 [70]. By immersing a series of rectangular plates in an insulating liquid, he found that the total capacitance of the resulting structure is linearly proportional to the number of plates used. In 1965, by depositing the IDE structure on the surface of a piezoelectric material, White and Voltmer [71] successfully formed the first surface acoustic wave (SAW) devices. This foundation initiated an explosion in the development of SAW technology over the next few decades [72]. SAW technology has had a huge impact in military applications, consumer electronics and telecommunications. The IDE concept was also applied extensively in sensing applications. The most important and attractive reason for use of this structure is its single-sided access feature [73]. This feature can be beneficial in nondestructive sensing when using electric [74--76], magnetic [77--79] or acoustic [80] fields to penetrate into the samples under test. In most of the cases mentioned above, the IDE is deposited on a dielectric without any piezoelectric properties or on a polar, nonferroelectric piezoelectric material such as quartz or, in the case of thin films, polar, nonferroelectric compounds such as aluminum nitride (AlN) and zinc oxide (ZnO). In these piezoelectric materials, because of the alternating signs of the electric potential between the neighboring IDE fingers, the sign of the piezoelectric stress also alternates and statically, the average stress can thus be cancelled. However, ferroelectric materials are different. Because the polarization of a ferroelectric material can be switched using an electric field, the same sign is installed for the stress in the piezoelectric layer. This enables the use of IDE structures in actuators [81]. In 1993, by applying IDE patterns to both sides of a single ferroelectric layer, Hagood and co-authors [66] demonstrated that the structure could provide a larger and more anisotropic strain than a conventional planar actuator with the TBE configuration. Recently, the IDE configuration has been used in several different cantilever [82] and plate-type [67] actuators. Additionally, because higher voltages can be achieved when larger gap distances are used, the IDE is also suitable for vibration energy harvesting applications [69, 83].

This wide range of potential applications has motivated the modeling of the IDE structure. Unlike conventional devices that use the TBE configuration, neither the direction nor the intensity of the electric field is homogeneous within the dielectric material when using the IDE configuration. This nonstandard distribution thus creates many challenges in prediction of the exact performance of these devices. For example, many efforts have previously been made to calculate the IDE capacitance. Because calculations of the most basic parallel plate model overestimate the IDE capacitance, more advanced calculation techniques are required. The first one to be mentioned here is the continuum model [75, 84, 85]. In this approach, the capacitance can be calculated by solving Laplace's equation for the scalar potential and the

electrical charge. Because the IDE structure is periodic, the electric potentials on these fingers can be spatially transformed using an infinite Fourier series. By inserting the transformation into Laplace's equation and applying the conservation of charge as a boundary condition, closed-form analytical solutions can be found for the potential and the charge. The conformal mapping technique (CMT) [86--90] is another analytical approach that can be used to calculate the IDE capacitance. The CMT originated from the fact that both the real and imaginary parts of an analytical function fulfill the Laplace equation in the complex plane. Using an analytic mapping process, an analytical function can be mapped to another analytical function on another complex plane. Laplace's equation can then be solved in the new plane using simpler standard geometries and boundary conditions. One computational approach used to calculate the IDE capacitance is the finite element method (FEM) [91--95]. The FEM model is generally recognized as the most popular computational approach in the literature.

In previous modelling researches, the complexity of the inhomogeneous field distribution has been addressed comprehensively. Laplace's equation is regarded as a starting point from which other physical quantities, e.g., capacitance, electric charge, electric field and potential, can be derived. Therefore, these models are only valid if the electric displacement is an electric field-dependent quantity. In piezoelectric materials, the electric displacement field is linearly related to both the electrical and mechanical fields. This electromechanical coupling effect presents another challenge when modelling the IDE structures. In fact, the electromechanical coupling not only affects the electrical quantities but can also affect the mechanical quantities.

In actuators, the mechanical performance aspects, e.g., free deflection, the blocking force and the electromechanical coupling factor, are important. To characterize the mechanical performance, it is necessary to apply an electric potential difference across the electrodes. The resulting electrical energy will then be coupled to generate an actuated stress that deforms the device against its mechanical stiffness. For balance, that mechanical deformation leads to the response of a mechanical stress. This mechanical stress acts in opposition to the actuated stress. Because piezoelectricity is a bi-directional effect, this mechanical stress also causes some electrical displacement on the electrode. Therefore, both the mechanical quantity, i.e., the stiffness, and the electrical quantity, i.e., the permittivity, can potentially be dependent on the electromechanical coupling factor. While the dependence of the permittivity on the piezoelectric electromechanical coupling factor has been formulated for both the IDE and TBE structures [96], the dependence of the mechanical flexural rigidity on the piezoelectric coupling factor has only previously been reported for TBE devices [97]. In IDE devices, the question of whether the mechanical flexural rigidity is dependent on the electromechanical coupling factor remains open and thus must be solved.

If the IDE structure is deposited on a ferroelectric material, the inhomogeneous electric field can then redistribute the permittivity inhomogeneously. This inhomogeneous permittivity then brings modelling of the IDE structure to the next level of complexity. The problem has thus become too complex to approach using an analytical model because the classical theory is only supported for solutions in homogeneous media. Therefore, the solution to this complex problem requires support from computational techniques.

4 Choice of research area

As mentioned in Section 2 and Section 3, there are many gaps in the knowledge and contradictions in the current understanding of piezoelectric actuators with IDE configurations. One of the areas that must be explored will involve study of the ways in which the materials electromechanical coupling factor affects both the electrical and mechanical properties of IDE transducers. Another relevant topic will involve establishing the governing equation for the electrostatic field inside the piezoelectric material when using the IDE configuration. Perhaps the most challenging and interesting topic will be to determine the inhomogeneous field inside the piezoelectric material with an IDE structure on top. The contradictions in the comparisons between the IDE and TBE actuators also represent an attractive topic. All the topics mentioned will first be investigated for the most basic MEMS building block: beam actuators. In detail, we will fill the knowledge gaps step by step by:

- Establishing a new general governing equation for bending of IDE beam actuators. From the general governing equation, we will show that the mechanical properties of cantilever and clamped-clamped beam actuators, without an applied external force, are not dependent on the materials electromechanical coupling factor.

- Establishing a general linear two-port model of IDE cantilevers. The two-port model will be established on the basis of the new governing equation for bending of IDE beam actuators. From the two-port parameters, we will then be able to see the effects of the materials electromechanical coupling factor on the electrical and mechanical properties of these cantilever transducers.

- Performing a deflection and electromechanical coupling factor comparison between the TBE and IDE beam actuators. We will then determine whether or not the IDE actuator represents a better choice than the TBE actuator.

- Establishing new governing equations to study the electrical properties, including the capacitance, the electric displacement and the electric field, of the piezoelectric material. For a non-piezoelectric material, Laplace's equation represents a starting point from which to derive the electrical properties inside the dielectric material. We will then determine whether this equation is also valid for piezoelectric materials.

- Determining the effects of the inhomogeneous electric field on the two-port parameters of IDE cantilever transducers.

- Characterizing ferroelectric materials when using the IDE configuration. The established theory will be used to characterize the properties of thin film ferroelectric materials, e.g., the CV and PV and stress-field loops.

- Modelling the inhomogeneous permittivity distributions inside piezoelectric materials.

Another interesting topic is modelling of a plate actuator when using the IDE configuration, because the plate is relevant as the most likely structure to be implemented in a tunable lens. In this topic, we will focus on:

- Modelling of the actuation of a circular plate piezoelectric actuator with the IDE electrode configuration.
- Making comparisons between TBE and IDE circular plate actuators. When used together with the comparison of the beam actuators, the two comparison studies will help to determine whether the IDE concept is suitable for use in the next generation of tunable lenses.
- Determining the effects of the different electrode configurations on the bending of circular plate actuators. In addition to the IDE and TBE actuators, other electrode patterns will also be investigated.

By following the studies of the topics mentioned above, we expect to establish suitable fundamental and practical knowledge for the design, modelling and characterization of piezoelectric microactuators with the IDE configuration. However, the scientific conclusions are not simply limited to microactuator-based applications such as micropumps, switches, and tunable lenses. The established theory can also be beneficial in sensor and generator-based applications.

5 Thesis outline

The thesis begins with a general introduction of the field of study, the motivation for the study and the choice of research area. Two most common structures used to construct MEMS devices, i.e., beams and plates, are then studied. Chapter 2 focuses on the beam actuators. The governing equations, the two-port models, the inhomogeneous distribution and the ferroelectric material characterization are all derived in this chapter. In Chapter 3, plate actuators are investigated. Circular plate-type actuators using the IDE configuration are modelled. A comparison of the deflection characteristics of plates with the TBE and IDE electrodes is given. The effects of the different electrode configurations on the actuation of circular plates are investigated. Finally, the conclusions and potential areas of further study are presented in Chapter 4. The Appendix attaches all the manuscripts that set the basis for the content of this thesis.

Chapter 2

Beam actuators

This chapter focuses on static responses of beam actuators. A new governing equation for bending and a two-port model of IDE beam actuator are derived. An inhomogeneous distribution of the electric field is investigated. The IDE actuator is compared with the TBE ones. Finally, these new models are used to characterize thin film ferroelectric material with the IDE configuration on top.

The chapter starts with an introduction on the general two-port representation of the beam actuators section 1. This model helps us understand how the transducers are responded to different kind of stimuli. To derive the two-port parameters, governing equations for each beam actuator e.g., TBE or IDE need to be established. Many studies have published the governing equations and the two-port model of the TBE beams. However, only a few studies recognized the effect of the material electromechanical coupling factor on the elastic property of the beam e.g., flexural rigidity. In addition, no publication studies this effect on the IDE beams. Therefore, starting from the piezoelectric constitutive relations, the new general governing equations section 3.1 and two-port parameters section 4 of the IDE beam actuators are established. The effects of the material electromechanical coupling factor on both electrical and mechanical parameters of the two-port model are derived. In section 5, the tip deflection of the IDE and TBE beams is chosen to compare. In section 6, the non-uniform electric field is investigated. Its effects on the physical parameters such as capacitance, deflection and transducer's electromechanical coupling factor are discussed. In section 7, the transducer electromechanical coupling factor of the IDE and TBE actuators are compared. Finally, all derived models are used to characterize the electrical and electromechanical properties of the thin film ferroelectric material with the IDE configuration. The novel characterization method is presented in section 8.

1 Modelling of the piezoelectric layered beam

1.1 The general form of two-port model

The constitutive equations (1.1-1.4) are used to model the piezoelectricity in the material level. In the structural level, the electromechanical properties of the transducer with piezoelectric material can also be modelled by other constitutive equations. These equations are relating stimulus and response of the transducer. For instance, with the piezoelectric cantilever beams Fig.2.1, the stimuli can for example be efforts such as force F and voltage V. A potential difference V is applied across

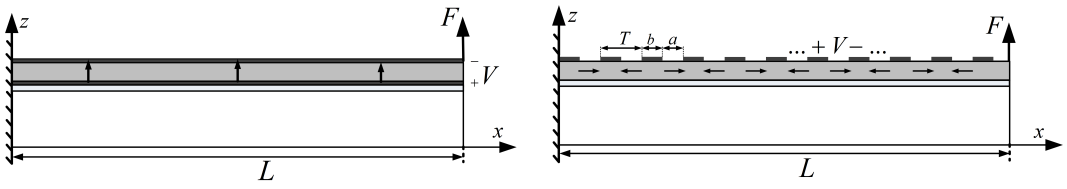

(a) TBE configuration (b) IDE configuration

Figure 2.1: Piezoelectric layered cantilever with d_{31} (a) and d_{33} (b) coupling. The arrows inside the piezoelectric layer (plotted in grey) show the direction of the polarization.

the electrodes and an external force F acts at the tip of the beam. The responses are then a total charge Q on the metal electrode and a tip deflection δ. Here, $x-y-z$ coordinate-system axes are device oriented and are different from the crystallographic axes $1-2-3$ of the piezoelectric material which are determined by the polarization direction (3-axis) and therefore may vary throughout the device. In general, the layered beams can include arbitrary number of layers of different materials as shown in Fig.2.2 i.e., an elastic structural material, a piezoelectric layer, some diffusion barriers and/or seed layers, and the IDE or TBE metal electrodes.

Under ideal conditions, the device has no loss or leakage. The energy-conserving transducer is assumed to work in the linear regime. Regardless of whether the configuration is a TBE Fig.2.1a or an IDE Fig.2.1b in static equilibrium, the tip deflection δ and electrical charge Q can be expressed as [98--100]

$$\begin{pmatrix} \delta \\ Q \end{pmatrix} = \begin{pmatrix} \frac{1}{K_s} & \zeta \\ \zeta & C \end{pmatrix} \begin{pmatrix} F \\ V \end{pmatrix}. \tag{2.1}$$

The relation (2.1) is the two-port model of the transducer. The transformation matrix is specified by three parameters: a beam short-circuit stiffness K_s, a free capacitance C and a transducer's coupling constant ζ. These parameters are analogous to the reciprocal Young's modulus, dielectric constant and the material coupling constant in the constitutive equations of the piezoelectric material. The transducer electromechanical coupling factor κ is

$$\kappa^2 = \frac{\zeta^2 K_s}{C}, \quad 0 \leq \kappa^2 \leq 1. \tag{2.2}$$

The squared electromechanical coupling factor is defined as the ratio of the output energy to the maximum input energy during a conversion cycle [58, 100]. Hence, it is a figure of merit saying how effective the piezoelectric transducer is in converting energy.

1.2 Governing equations

In approaching the governing equations, some assumptions are required [101]

1. Each layer is purely linear elastic or piezoelectric.
2. All parts of the structure are in static equilibrium.
3. There is no slip at interfaces between layers.
4. Beam thickness is always much smaller than the radius of bending curvature.
5. A *narrow beam* is defined as a beam with width much smaller than its length.
6. A *wide beam* is defined as a beam with width is much larger than its length.

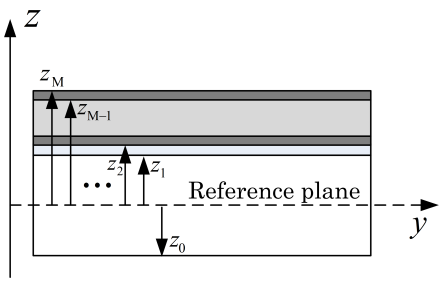

Figure 2.2: Cross section of layered beam structure. An example of the TBE device with M layers.

We distinguish the two special cases of a *narrow beam* and a *wide beam* with respectively *plane stress* and *plane strain* constitutive equations. Distinguishing with respect to the width to length ratio is motivated by the Searle parameter [102] being small and by Swanson's result for homogeneous beams [103] that the wide-to-narrow-beam transition is independent of the thickness. Intermediate cases do of course occur, but would have to be treated by plate theory.

Different constraints of narrow or wide beam lead to different boundary conditions of the beam in the width direction. For the narrow beam, the stress is zero and for the wide beam, the strain is zero. Hence, the effective Young's modulus Y, piezoelectric coupling constants d, and dielectric constant ε for d_{31} (2.3,2.4) [97] and d_{33} (2.5,2.6) coupling are different in these cases and are defined as

$$Y = \begin{cases} \frac{1}{s_{11}^E} & \text{narrow beam} \\ \frac{1}{s_{11,\text{eff}}^E} = \frac{s_{22}^E}{s_{11}^E s_{22}^E - \left(s_{12}^E\right)^2} & \text{wide beam,} \end{cases} \tag{2.3}$$

$$d = \begin{cases} d_{31} & \text{narrow beam} \\ d_{31,\text{eff}} = d_{31} - d_{32}\frac{s_{12}^E}{s_{22}^E} & \text{wide beam.} \end{cases} \tag{2.4}$$

$$Y = \begin{cases} \frac{1}{s_{33}^E} & \text{narrow beam} \\ \frac{1}{s_{33,\text{eff}}^E} = \frac{s_{22}^E}{s_{22}^E s_{33}^E - \left(s_{32}^E\right)^2} & \text{wide beam,} \end{cases} \tag{2.5}$$

$$d = \begin{cases} d_{33} & \text{narrow beam} \\ d_{33,\text{eff}} = d_{33} - d_{32}\frac{s_{32}^E}{s_{22}^E} & \text{wide beam.} \end{cases} \tag{2.6}$$

$$\varepsilon = \begin{cases} \varepsilon_{33}^T & \text{narrow beam} \\ \varepsilon_{33,\text{eff}}^T = \varepsilon_{33}^T - \frac{d_{32}^2}{s_{22}^E} & \text{wide beam.} \end{cases} \tag{2.7}$$

where s_{ij}^E is the compliance at constant electric field, d_{ij} is the piezoelectric coupling constant and ε_{ij}^T is the dielectric constant at constant stress. The Voigt notation [45] is used. In our analysis, we assume that the piezoelectric material has zero shear-tension coupling, i.e., $s_{ij}^E = 0$ for $i = 1, 2, 3$ and $j = 4, 5, 6$. This assumption applies to many materials such as those with orthorohombic, cubic, isotropic or hexagonal symmetry [46].

From the assumptions, the x-axis normal strain in the beam is

$$S(x,z) = u'(x) - zw''(x) \tag{2.8}$$

where $u(x)$ and $w(x)$ are the longitudinal displacement and the transversal deflection of a point at position x along the beam axis.

Let z_m denote the lowest coordinate the m^{th} layer along the z-axis as shown in Fig.2.2. Y_m, d_m, and ε_m are the effective material parameters of this layer. Starting from the d-form of the piezoelectric constitutive equations (1.1) and using the effective constants in (2.3-2.7), constitutive equations within a layer can be written

$$T_m(x,z) = Y_m(S(x,z) - d_m E_m(x,z)) \tag{2.9}$$

$$D_m(x,z) = \varepsilon_m(1-\kappa_m^2)E_m(x,z) + d_m Y_m S(x,z) \tag{2.10}$$

where $\kappa_m^2 = Y_m d_m^2/\varepsilon_m$ is an electromechanical coupling factor for the material.

To establish the governing equations, (2.8-2.10) are used to express the electric displacement $D_m(x,z)$, the stress resultants bending moment per unit width

$$M(x) = \sum_{m=0}^{\mathrm{M}-1} \int_{z_m}^{z_{m+1}} T_m(x,z) z \mathrm{d}z, \tag{2.11}$$

and axial force per unit width

$$P(x) = \sum_{m=0}^{\mathrm{M}-1} \int_{z_m}^{z_{m+1}} T_m(x,z) \mathrm{d}z \tag{2.12}$$

in terms of V, u' and w'' for a section of the beam. Together with beam equilibrium equations, these results can be used to obtain expressions for the parameters of the two-port model stated in (2.1).

2 Two-port model of the TBE transducer

Although two-port models of unimorph and bimorph transducers have been published [98, 99, 104], however, these work were limited for two-layer structures. In addition, effect of the material electromechanical coupling factor on the mechanical property was not mentioned. This effect was later recognized in a few researches e.g., [97]. They showed that the flexural rigidity of the structure is dependent on the electromechanical coupling factor of the piezoelectric material.

In this section, a general governing equation for the bending of the unimorph TBE actuator with arbitrary number of layers is reviewed [97]. Using this equation, the two-port model of the TBE cantilever is derived. Then, the effect of the material electromechanical coupling factor on both electrical and mechanical property of the transducer is observed.

First, we choose the coordinate system that can decouple the bending moment with the axial strain, and the axial force with the bending strain. One can show that this decoupling is achieved when

$$\sum_m \bar{z}_m Y_m t_m = 0 \tag{2.13}$$

where $t_m = z_{m+1} - z_m$ the thickness of the m^{th} layer and $\bar{z}_m = (z_{m+1} + z_m)/2$. By $\sum_m$, we mean $\sum_{m=0}^{\mathrm{M}-1}$ with M the number of layers and this notation is used hereafter. This choice leads to

$$M(x) = -\hat{K}\frac{\partial^2 w}{\partial x^2} + \hat{\Gamma}\frac{V}{t_\mathrm{p}} \tag{2.14}$$

or

$$\frac{\partial^2 w}{\partial x^2} = -\frac{M(x)}{\hat{K}} + \frac{\hat{\Gamma}}{\hat{K}}\frac{V}{t_p} \tag{2.15}$$

where the t_p is the thickness of the piezoelectric layer and

$$\hat{K} = \sum_m Y_m \left[\frac{I_m}{1-\kappa_m^2} + t_m \bar{z}_m^2\right], \tag{2.16}$$

$$\hat{\Gamma} = \sum_m \bar{z}_m Y_m t_m d_m. \tag{2.17}$$

Here, $I_m = t_m^3/12$ is the area moment of inertia per unit width of the m^{th} layer.

As the force F acts at the tip of the beam,

$$M(x) = -F(L-x). \tag{2.18}$$

The derivation of the tip deflection δ is as follows. First, we substitute (2.18) into (2.15). Then, the new equation is integrated across the beam length. Finally, boundary conditions, no deflection and no slope at the clamped end, are applied to find all integral constants.

From Gauss's law, the electric displacement within the piezoelectric layer at any cross-section is constant. This value is found by integrating (2.10) along the z-axis:

$$\overline{D_z}(x) = \frac{1}{t_p}\int_{z_p}^{z_{p+1}} D_z(x,z)\mathrm{d}z. \tag{2.19}$$

In the integral (2.19), the strain $S(x,z)$ is given in (2.8) and the second derivative of the deflection is given in (2.15). The total electric charge per unit width is

$$Q = \int_0^L \overline{D_z}(x)\mathrm{d}x. \tag{2.20}$$

Neglecting the small contribution to charge from the axial strain, we arrive at a TBE two-port-model with narrow-beam parameters

$$K_\mathrm{s} = \frac{3\hat{K}}{L^3}, \tag{2.21}$$

$$\zeta = \frac{\bar{z}_p d_{31}}{s_{11}^E \hat{K}}\frac{L^2}{2}, \tag{2.22}$$

$$C = \varepsilon_{33}^T\left[1 + (\alpha_{31}-1)\,\kappa_{31}^2\right]\frac{L}{t_p}, \tag{2.23}$$

and

$$\kappa^2 = \frac{3}{4}\frac{\alpha_{31}\kappa_{31}^2}{1+(\alpha_{31}-1)\kappa_{31}^2} \tag{2.24}$$

where $\alpha_{31} = t_p \bar{z}_p^2/(s_{11}^E \hat{K})$, $\kappa_{31}^2 = d_{31}^2/(s_{11}^E \varepsilon_{33}^T)$. Note that $t_p \bar{z}_p^2/s_{11}^E$ is a contribution of the piezoelectric layer to the flexural rigidity of the beam (2.16). The quantity α_{31} therefore quantifies the relative contribution of the piezoelectric layer to the flexural rigidity. We will refer to it as a flexural rigidity ratio.

The formula (2.21) show that the stiffness K_s of the structure is not only dependent on the elasticity and dimension of the layers but also the electromechanical coupling factor of the piezoelectric material. The formulas (2.23) and (2.24) show that C and κ^2 are not only determined by the piezoelectric material. Moreover, these parameters are also dependent on the other materials of the stack and their relative positions, i.e., through the flexural rigidity ratio.

For the wide beam, the effective values (2.3), (2.4) and (2.7) should be used instead to obtain its parameters by exactly the same route.

For the specific case of a unimorph beam, the two-port parameters were presented in [98] and [104]. By neglecting the contribution of the electromechanical coupling on the flexural rigidity in (2.16), our general results (2.21), (2.23) and (2.24) agree with these previous results by setting M = 2.

3 Governing equation of d_{33} coupling beams

For the d_{31} coupling transducers, we observed that the material electromechanical coupling factor modifies the flexural rigidity of the piezoelectric material with a term $1/(1-\kappa_m^2)$ (2.16). This contribution can be substantial if the piezoelectric material has high electromechanical coupling factor or if the piezoelectric layers dominate the thickness in some multimorphs structure [97]. The concern turns out if the material electromechanical coupling factor has some contributions on the d_{33} coupling transducers or not. In this section, detail analyses are given for the clarification.

3.1 Governing equation

We assume that the electric displacement in the active region is constant along the length. It is found by integrating (2.10) across the active region i.e., $nT + b \leq x \leq (n+1)T$, n is an integer, so that

$$D_m(x,z) = d_m Y_m \bar{S}(z) - \varepsilon_m(1-\kappa_m^2)\frac{V}{a} \tag{2.25}$$

where

$$\bar{S}(z) = \frac{1}{a}\int_{nT+b}^{(n+1)T} S(x,z)\,dx = \frac{u(\mathrm{T}_n + a) - u(\mathrm{T}_n)}{a} - z\frac{w'(\mathrm{T}_n + a) - w'(\mathrm{T}_n)}{a} \tag{2.26}$$

and $\mathrm{T}_n = nT + b$.
Substituting (2.25) into (2.10) leads to

$$E_m(x,z) = -\frac{V}{a} - \frac{\xi_m}{d_m}(S(x,z) - \bar{S}(z)) \tag{2.27}$$

where $\xi_m = \frac{\kappa_m^2}{1-\kappa_m^2}$.

Now substituting (2.27) into (2.9) the resultant stress is obtained as

$$T_m(x,z) = Y_m\left((1+\xi_m)S(x,z) - \xi_m \bar{S}(z) + d_m\frac{V}{a}\right). \tag{2.28}$$

Then, the bending moment (2.11) and stretching force (2.12) per unit width can be found by integrating the stress (2.28) along the thickness. We choose the origin so that $\sum_m t_m Y_m \bar{z}_m = 0$ where $\bar{z}_m = (z_m + z_{m+1})/2$. Then, the governing equations of the layered beam structure with d_{33} coupling are

$$P(x) = \left(\hat{K}_P + \hat{K}_{P,\xi}\right) u'(x) - \hat{\Gamma}_\xi w''(x) + \hat{P}_E - \hat{K}_{P,\xi} \frac{u\left(\mathrm{T}_n + a\right) - u\left(\mathrm{T}_n\right)}{a} + \hat{\Gamma}_\xi \frac{w'\left(\mathrm{T}_n + a\right) - w'\left(\mathrm{T}_n\right)}{a}, \tag{2.29}$$

$$M\left(x\right) = \hat{\Gamma}_\xi u'(x) - \left(\hat{K}_2 + \hat{K}_{2,\xi}\right) w''(x) + \hat{M}_{E2} - \hat{\Gamma}_\xi \frac{u\left(\mathrm{T}_n + a\right) - u\left(\mathrm{T}_n\right)}{a} + \hat{K}_{2,\xi} \frac{w'\left(\mathrm{T}_n + a\right) - w'\left(\mathrm{T}_n\right)}{a} \tag{2.30}$$

where

$$\hat{P}_E = \sum_m t_m Y_m d_m \frac{V}{a}, \tag{2.31}$$

$$\hat{K}_P = \sum_m t_m Y_m, \tag{2.32}$$

$$\hat{M}_{E2} = \sum_m t_m Y_m \bar{z}_m d_m \frac{V}{a}, \tag{2.33}$$

$$\hat{K}_2 = \sum_m t_m Y_m \left(\bar{z}_m^2 + \frac{t_m^2}{12}\right), \tag{2.34}$$

and the remaining definitions are $\hat{K}_{P,\xi} = \sum_m t_m Y_m \xi_m$, $\hat{\Gamma}_\xi = \sum_m t_m Y_m \bar{z}_m \xi_m$ and $\hat{K}_{2,\xi} = \sum_m t_m Y_m \xi_m \left(\bar{z}_m^2 + \frac{t_m^2}{12}\right)$.

Integrating (2.29) and (2.30) along the active region leads to

$$\frac{u\left(\mathrm{T}_n + a\right) - u\left(\mathrm{T}_n\right)}{a} = -\frac{\hat{P}_E - P_n}{\hat{K}_P}, \tag{2.35}$$

$$\frac{w'\left(\mathrm{T}_n + a\right) - w'\left(\mathrm{T}_n\right)}{a} = \frac{\hat{M}_{E2} - M_n}{\hat{K}_2} \tag{2.36}$$

where $P_n = \frac{1}{a}\int_{nT+b}^{(n+1)T} P(x)dx$ and $M_n = \frac{1}{a}\int_{nT+b}^{(n+1)T} M(x)dx$ are respectively the average force and moment per unit width.

Finally, substituting (2.35) and (2.36) into (2.29) and (2.30), solving the new equations with respect to $u'\left(x\right)$ and $w''\left(x\right)$, we get

$$u'\left(x\right) = -\frac{\hat{P}_E}{\hat{K}_P} - \frac{\hat{\Gamma}_\xi \left(M(x) - M_n\right)}{(\hat{K}_p + \hat{K}_{p,\xi})(\hat{K}_2 + \hat{K}_{2,\xi}) - \hat{\Gamma}_\xi^2} + \frac{P_n}{\hat{K}_p} \frac{\left(\frac{P(x)}{P_n}\hat{K}_P + \hat{K}_{p,\xi}\right)(\hat{K}_2 + \hat{K}_{2,\xi}) - \hat{\Gamma}_\xi^2}{(\hat{K}_p + \hat{K}_{p,\xi})(\hat{K}_2 + \hat{K}_{2,\xi}) - \hat{\Gamma}_\xi^2}, \tag{2.37}$$

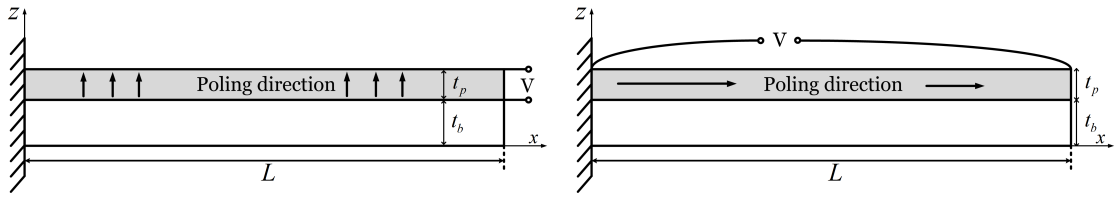

(a) d_{31} coupling actuator (b) d_{33} coupling actuator

Figure 2.3: The potential V is applied to kept electric field strength at $E = 1\text{MV/m}$ in both case of coupling mode and $t_b + t_p = 40\mu\text{m}$.

$$w''(x) = \frac{\hat{M}_{E2}}{\hat{K}_2} + \frac{\hat{\Gamma}_\xi \left(P(x) - P_n\right)}{(\hat{K}_p + \hat{K}_{p,\xi})(\hat{K}_2 + \hat{K}_{2,\xi}) - \hat{\Gamma}_\xi^2} - \frac{M_n}{\hat{K}_2} \frac{\left(\hat{K}_P + \hat{K}_{p,\xi}\right)\left(\frac{M(x)}{M_n}\hat{K}_2 + \hat{K}_{2,\xi}\right) - \hat{\Gamma}_\xi^2}{(\hat{K}_p + \hat{K}_{p,\xi})(\hat{K}_2 + \hat{K}_{2,\xi}) - \hat{\Gamma}_\xi^2}. \tag{2.38}$$

If no external force is applied ($F = 0$), for the cantilever beam, $M(x) = P(x) = 0$ and then

$$u'(x) = -\frac{\hat{P}_E}{\hat{K}_P}, \tag{2.39}$$

$$w''(x) = \frac{\hat{M}_{E2}}{\hat{K}_2}. \tag{2.40}$$

For the clamped-clamped beam actuator, $M(x) = M_n = \text{const}$ and $P(x) = P_n = 0$. Then

$$u'(x) = -\frac{\hat{P}_E}{\hat{K}_P}, \tag{2.41}$$

$$w''(x) = \frac{\hat{M}_{E2} - M_n}{\hat{K}_2}. \tag{2.42}$$

Equations (2.39), (2.40), (2.41) and (2.42) show that no coupling correction term appears in the flexural rigidity of the IDE-beam active regions.

3.2 Case studies

Two cantilever beams are investigated, both have length L of 1mm. In these case studies, we limit the structures with two layers. A structural layer has the Young modulus of 74 GPa and the Poisson's ratio of 0.3. A piezoelectric layer has properties as given in Table.2.1. The electrode layers are much thinner than other layers so that their elastic effects can be neglected.

Beam with d_{31} coupling

Figure 2.3a is the beam actuator with d_{31} coupling. The electric field direction is parallel to the polarization direction, the stress and strain fields are induced in perpendicular to the polarization direction.

By integrating the bending curvature (2.15) along the x-direction, the free tip deflection is

$$\delta_{\text{TBE}}(L) = \rho_{31}\frac{L^2}{2} \tag{2.43}$$

Table 2.1: $PbZr_{0.53}Ti_{0.47}O_3$ parameters calculated from [50--52]

Parameters and unit	Narrow beam		Wide beam	
	Notation	Value	Notation	Value
Compliance ($(TPa)^{-1}$)	$s_{11}^E = s_{22}^E$	13.8	$s_{11,\text{eff}}^E$	12.6
	s_{12}^E	-4.07		
	$s_{32}^E = s_{31}^E$	-5.8		
	s_{33}^E	17.1	$s_{33,\text{eff}}^E$	14.7
Piezoelectric coupling (pm/V)	$d_{31} = d_{32}$	-116.7	$d_{31,\text{eff}}$	-151.1
	d_{33}	224.2	$d_{33,\text{eff}}$	175.2
Permittivity	ϵ_{11}^T	$1290\varepsilon_0$		
	ϵ_{33}^T	$1180\varepsilon_0$	$\epsilon_{33,\text{eff}}^T$	$1067\varepsilon_0$
Material electromechanical coupling factor	κ_{31}^2	0.09	$\kappa_{31,\text{eff}}^2$	0.19
	κ_{33}^2	0.28	$\kappa_{33,\text{eff}}^2$	0.22

where $\rho_{31} = (\hat{\Gamma}V)/(\hat{K}t_p)$ is the free bending curvature ($M(x) = 0$) of the TBE beam.

In Fig.2.4a, two analytical model are validated by the FEM simulation. The standard model is plotted when κ_{31} is excluded in the flexural rigidity $\hat{K}$ (2.16). This standard model of flexural rigidity is often found in literatures [98, 104]. The corrected model is plotted when κ_{31} is included in the flexural rigidity $\hat{K}$ as given in (2.16). Figure 2.4a shows that the corrected model with the modification in the flexural rigidity is the best in reproducing the results calculated by the finite element simulation. However, if the piezoelectric film is thin ($\alpha > 0.6$), both analytical model can reproduce the FEM results. This is because the flexural rigidity of the whole structure is dominant by the structural layer. Therefore, a small correction for a small flexural rigidity of the piezoelectric layer is not so important and can be neglected.

Beam with d_{33} coupling

For actuators with the d_{33} coupling, the electric field, polarization and stress strain fields are all in a horizontal direction. We simplify the actuator with one active region as shown in Fig.2.3b. For thin piezoelectric film, this configuration seems unrealistic since it requires a very high electric potential ($\approx 10^4 V$) for poling. However, the configuration is a good example to understand the actuation with d_{33} coupling.

By integrating the bending curvature (2.40) along the x-direction, the free tip deflection is

$$\delta_{\text{IDE}}(L) = \rho_{33}\frac{L^2}{2} \tag{2.44}$$

where $\rho_{33} = \hat{M}_{E2}/\hat{K}_2$ is the free bending curvature ($M(x) = 0$) of the IDE beam.

The FEM and analytical results in Fig.2.4b are perfectly agreed. No correction term requires for the flexural rigidity as expected.

4 Two-port model of the IDE transducer

The IDE structure is shown in Fig.2.1b. We first assume that the electric field has a homogeneous distribution within the active regions i.e., between the electrode fingers and is zero in the passive regions i.e., beneath each finger as shown in Fig.2.5.

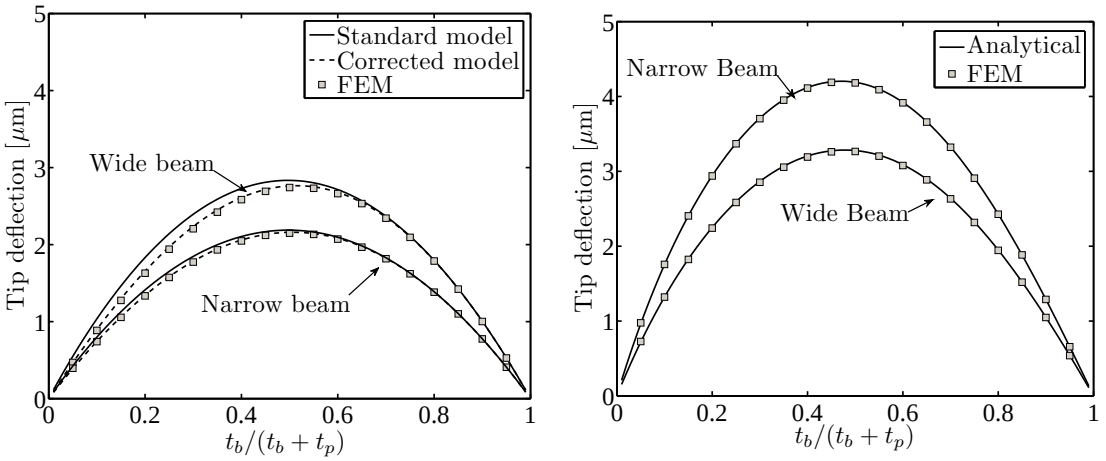

(a) with the d_{31} coupling

(b) with the d_{33} coupling

Figure 2.4: Tip deflection of piezoelectric actuator at different thickness of the substrate and piezoelectric material $t_b/(t_p+t_b)$ and $t_b+t_p=40\mu$m.

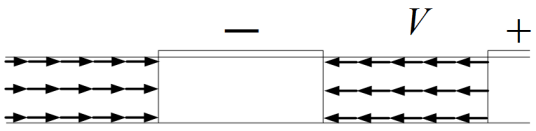

Figure 2.5: Homogeneous field distribution assumption inside active regions.

We choose the origin as mentioned in section 3.1 i.e., $\sum_m t_m Y_m \bar{z}_m = 0$. Due to the different stack layers between the active and passive regions i.e., orientation of the piezoelectric polarization and the presence of a very thin metal-electrode film, the origin are located differently. We choose the one in the active regions. With this choice, there will be a small such coupling in the passive regions due to the different stack layers, we neglect this tiny coupling. Hence, from (2.15) and (2.38) the governing equation of the IDE beam is

$$\frac{\partial^2 w}{\partial x^2} = \begin{cases} -\frac{M(x)}{\hat{K}} & \text{Passive region} \\ \frac{\hat{M}_{E2}}{\hat{K}_2} - \frac{M(x)}{\widetilde{K}_2} - M_n\left(\frac{1}{\hat{K}_2} - \frac{1}{\widetilde{K}_2}\right) & \text{Active region} \end{cases} \tag{2.45}$$

where the passive and active regions which are respectively $x \in [nT, nT+b)$ and $x \in [nT+b, (n+1)T)$ for integer n. The flexural rigidities $\hat{K}$ and $\hat{K}_2$ in the passive and active regions respectively are given in (2.16) and (2.34). The flexural rigidity $\widetilde{K}_2$ is

$$\widetilde{K}_2 = \hat{K}_2 + \hat{K}_{2,\xi} - \frac{\hat{\Gamma}_\xi^2}{\hat{K}_p + \hat{K}_{p,\xi}}, \tag{2.46}$$

where all definitions are given in section 3.1. By inserting (2.18) into (2.45), integrating the resulting relation across the beam length, and applying boundary conditions, the tip deflection δ of the beam is found. From (2.1), the short-circuit compliance $1/K_s$ is the ratio of this deflection to the force at zero voltage, i.e.,

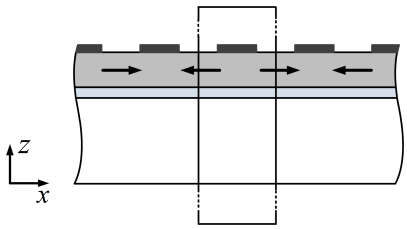

Figure 2.6: The total electric charge on an electrode is found by integrating the normal component of the electric displacement vector around the contour.

$$\frac{1}{K_\mathrm{s}} = \frac{L(N+1)}{\hat{K}_2}\left[\frac{a^2}{2} - \frac{a^3+3a^2b}{6L} + \frac{NTa}{2} - \frac{N(N+2)T^2a}{6L}\right] - \frac{(N+1)a^3}{12}\left(\frac{1}{\hat{K}_2} - \frac{1}{\widetilde{K}_2}\right) + \frac{L(N+1)}{\hat{K}}\left[\frac{b^2+2ab}{2} - \frac{b^3+3ab^2}{6L} + \frac{NTb}{2} - \frac{N(N+2)T^2b}{6L}\right] \tag{2.47}$$

where N is the number of active regions and $L = (N+1)T$.

The coupling constant is the ratio of the deflection to the voltage for zero force, and can be written

$$\zeta = \frac{\bar{z}_p t_p d_{33}}{s_{33}^E \hat{K}_2}\frac{N^2 a}{2}\left(1 + \left(1+\frac{1}{N}\right)\frac{b}{a} + \frac{2}{N}\right). \tag{2.48}$$

The total electric charge per unit width on an electrode of the IDE cantilever can be found by integrating the normal component of the electric displacement vector around a contour as shown in Fig.2.6 and summing over all fingers of the electrode. Neglecting the electric flux outside the piezoelectric material, the contour integral reduces to two integrals across the piezoelectric layers on each side of the finger. Choosing the contour to cross in the middle of the active regions, i.e., at $x = \bar{x}_n = (n+1/2)T + b/2$, ensures that the displacement field is x-directed and aligned with or against the normal on those parts of the contour. Hence with N active regions, the charge is

$$Q = \sum_{n=0}^{N-1}\int_{z_p}^{z_{p+1}} D_x(\bar{x}_n, z)\mathrm{d}z. \tag{2.49}$$

In evaluating this charge, we assume that the electric field is a constant, i.e., $E(x,z) = E_x = V/a$. From the charge expression, we can then extract the free capacitance C as the coefficient of voltage dependence when the force is equal to zero. It is

$$C = \varepsilon_{33,\mathrm{eff}}\frac{Nt_p}{a} \tag{2.50}$$

where we defined an effective permittivity

$$\varepsilon_{33,\mathrm{eff}} = \varepsilon_{33}^T\left[1 + (\alpha_{33}-1)\,\kappa_{33}^2\right]. \tag{2.51}$$

and $\alpha_{33} = \frac{t_p\bar{z}_p^2}{s_{33}^E\hat{K}_2}$, $\kappa_{33}^2 = \frac{d_{33}^2}{s_{33}^E\varepsilon_{33}^T}$.

Since we know C, K_s, and ζ the coupling is conveniently quantified in terms of the two-port electromechanical coupling factor (2.2) which becomes

$$\kappa^2 = \frac{3}{4}\frac{\alpha_{33}\kappa_{33}^2}{1+(\alpha_{33}-1)\kappa_{33}^2}\frac{N^3a^3}{L^3}\left[1 + \left(1+\frac{1}{N}\right)\frac{b}{a} + \frac{2}{N}\right]^2 \tag{2.52}$$

where we made the simplification

$$\hat{K} \approx \widetilde{K}_2 \approx \hat{K}_2. \tag{2.53}$$

Then

$$K_{\mathrm{s}} = \frac{3\hat{K}_2}{L^3}. \tag{2.54}$$

When N is large enough, we can further simplify to

$$\kappa^2 = \frac{3}{4}\frac{\alpha_{33}\kappa_{33}^2}{1+(\alpha_{33}-1)\kappa_{33}^2}\frac{a}{T}. \tag{2.55}$$

Similarly to the TBE device, equations (2.50), (2.55) show that C and κ^2 in the IDE device are also dependent on the detailed layer structure through a flexural rigidity ratio, here called α_{33}. Equation (2.55) state that the electromechanical coupling factor of the IDE device is also dependent on the gap to pitch ratio.

Note that all analysis apply for the narrow structure. For the wide beam, the effective values (2.5, 2.6, 2.7) should be used.

5 Deflection of the piezoelectric layered beam

In this section, the free deflection of the IDE and TBE actuator are compared. In some optical applications such as scanning micro-mirrors [16, 105], optical switches [106], optical image stabilizers [107] and tunable lenses [10, 108] the tip deflection should be as high as possible. Moreover, measured beam deflection is a standard method to characterize thin piezoelectric films. This method has been commercialized with the aixACCT systems [109] for the transversal coupling measurement with the TBE beam [110]. An accurate model of the IDE beam can be applied for an accurate measurement of the longitudinal coupling.

5.1 Comparison between piezoelectric beams with the TBE and IDE configurations

The established models in section 2 and 4 are used to compare the free tip deflection between the TBE and IDE beams. The comparison helps designers to determine the actuation with higher deflection capability. This is important for some optical applications as mentioned above.

The comparison is conducted both at equal voltage and at equal electric field. In the first comparison the same potential difference V is applied across the TBE as between the neighbouring electrodes of the IDE actuator. In the equal-field comparison, the voltages are set such that the average electric field strength is the same in the IDE and the TBE. The applied voltage between the neighbouring fingers in the IDE actuator V_{IDE} and the applied voltage between the top and the bottom electrode in the TBE actuator V_{TBE} are then related by

$$V_{\mathrm{IDE}} = V_{\mathrm{TBE}} \times \frac{a}{t_p}. \tag{2.56}$$

From paper 1 [111], the wide-beam actuator is the upper deflection limit for the TBE beams and is the lower deflection limit for the IDE beam. This means

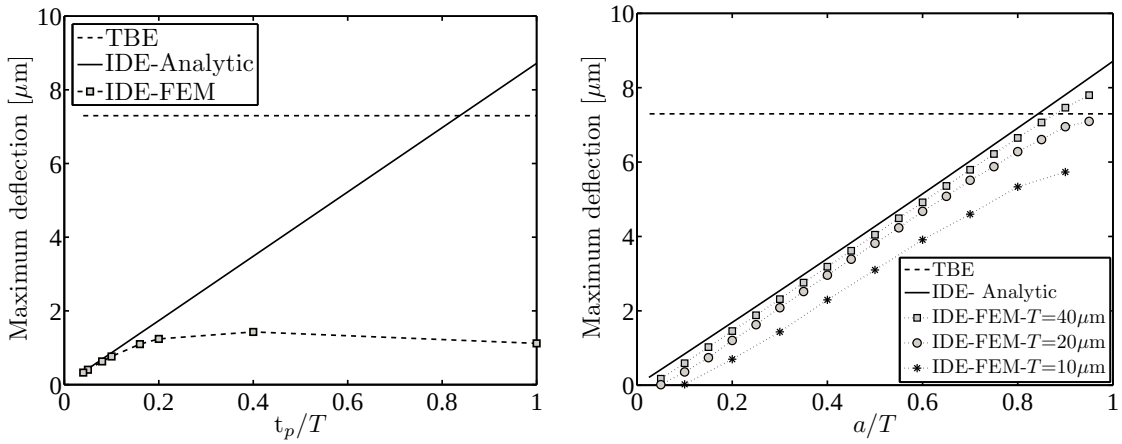

(a) Equal voltage at VTBE=VIDE=10V (b) Equal electric field with VTBE=10V

Figure 2.7: IDE and TBE cantilever actuators comparison. For the IDE, the finger spacings and finger widths are a = b = T/2. The thickness of the piezoelectric layer is t_p = 2um.

that if there exists a wide-beam IDE actuator that has larger deflection than the corresponding TBE actuator, then the deflection is larger for any IDE actuator width. Therefore, we only consider the wide-beam actuators which is the more conservative choice with respect to IDE performance. We are not limit our comparison with only the cantilever beam but the clamped-clamped beam are also compared.

Cantilever beams

If we substitute $L = (N+1)(a+b)$ into (2.22), the free tip deflection of the d_{31} mode actuator is

$$\delta_{\text{TBE}} = \zeta_{\text{TBE}} V_{\text{TBE}} = \frac{\bar{z}_{p,\text{TBE}} d_{31}}{s_{11}^E \hat{K}} \frac{(Na)^2}{2} \left[1 + \left(1 + \frac{1}{N}\right)\frac{b}{a} + \frac{1}{N}\right]^2 V_{\text{TBE}}. \tag{2.57}$$

From (2.48) and (2.57), the tip deflection ratio between the two types of cantilever actuators is

$$\left|\frac{\delta_{\text{IDE}}}{\delta_{\text{TBE}}}\right| = \left|\frac{\bar{z}_{p,\text{IDE}}}{\bar{z}_{p,\text{TBE}}} \frac{V_{\text{IDE}}}{V_{\text{TBE}}} \frac{\hat{K}}{\hat{K}_2} \frac{d_{33} s_{11}^E}{d_{31} s_{33}^E} \frac{t_p}{a}\right| \frac{\left[1 + \left(1 + \frac{1}{N}\right)\frac{b}{a} + \frac{2}{N}\right]}{\left[1 + \left(1 + \frac{1}{N}\right)\frac{b}{a} + \frac{1}{N}\right]^2}. \tag{2.58}$$

The comparison between the IDE and the TBE cantilever actuators is shown in Fig. 2.7a for the same voltage. Analytical result predict that the IDE actuator can have higher deflection than the TBE one if $t_p/T > 0.8$. However, this is not the case with the FEM results, the TBE actuator is always superior to the IDE actuator. The analytical result and FEM results is only agree well when the thickness of the piezoelectric much smaller than the gap. Otherwise, electric field is non-uniform and reduce the performance of the IDE device.

Comparison at the same electric field strength is shown in Fig. 2.7b. The IDE wide-beam actuator is preferred if the ratio between the gap and the pitch a/T is larger than 0.8. This is confirmed by the FEM calculation when the pitch is $T = 40\mu$m and a/T is around 0.8. The FEM results also report that the smaller the pitch the smaller the deflection.

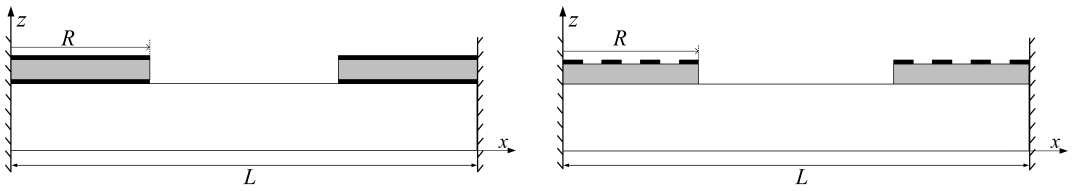

(a) TBE (b) IDE

Figure 2.8: TBE (a) and IDE (b) clamped-clamped beam actuators.

Clamped-clamped beams

The clamped-clamped beams with TBE and IDE configurations are shown in Fig.2.8a and Fig.2.8b respectively. From paper 1 [111], the deflection at the center of the clamped-clamped beams are

$$\delta_{\text{TBE}}\left(\frac{L}{2}\right) = \frac{\bar{z}_{p,\text{TBE}} d_{31}}{s_{11}^E \hat{K}} \frac{L^2}{8} \frac{X\left(1-X\right)}{1+\left(\frac{Y_b I_b}{\hat{K}}-1\right)X} V_{\text{TBE}} \tag{2.59}$$

and

$$\delta_{\text{IDE}}\left(\frac{L}{2}\right) = \frac{\bar{z}_{p,\text{IDE}} d_{33}}{s_{33}^E \hat{K}_2} \frac{t_p}{T} \frac{L^2}{8} \frac{X(1-X)}{1+\left(\frac{Y_b I_b}{\hat{K}_2}\frac{a}{T}+(1+\frac{1}{N})\frac{Y_b I_b}{\hat{K}}\frac{b}{T}-1\right)X} V_{\text{IDE}} \tag{2.60}$$

where $X = 2R/L$. Y_b, $I_b = t_b^3/12$ are respectively the Young's modulus and the moment of inertia per unit width of the structural layer with the thickness t_b. The optimum transducer length can be found from (2.59) and (2.60) are

$$X_{\text{TBE}}^{\text{opt}} = \left(1+\sqrt{\frac{Y_b I_b}{\hat{K}}}\right)^{-1}, \tag{2.61}$$

and

$$X_{\text{IDE}}^{\text{opt}} = \left(1+\sqrt{\frac{Y_b I_b}{\hat{K}_2}\frac{a}{T}+(1+\frac{1}{N})\frac{Y_b I_b}{\hat{K}}\frac{b}{T}}\right)^{-1}. \tag{2.62}$$

With the simplifications $Y_b I_b \approx \hat{K}_2 \approx \hat{K}$ and large N, the optimum values in both cases equal one quarter of a beam length. This means that 50% of the beam surface should be covered by the piezoelectric film.

From (2.59) and (2.60), the maximum deflection ratio for a clamped-clamped beam actuator is

$$\left|\frac{\delta_{\text{IDE}}}{\delta_{\text{TBE}}}\right| = \left|\frac{\bar{z}_{p,\text{IDE}}}{\bar{z}_{p,\text{TBE}}}\frac{V_{\text{IDE}}}{V_{\text{TBE}}}\frac{\hat{K}}{\hat{K}_2}\frac{d_{33}s_{11}^E}{d_{31}s_{33}^E}\frac{t_p}{T}\right| \frac{1+\left(\frac{Y_b I_b}{\hat{K}}-1\right)X}{1+\left(\frac{Y_b I_b}{\hat{K}_2}\frac{a}{T}+(1+\frac{1}{N})\frac{Y_b I_b}{\hat{K}}\frac{b}{T}-1\right)X}. \tag{2.63}$$

For the equal-voltage comparison, the results in Fig.2.9a show a similar tendency to the cantilever case. The deflection of the IDE actuator calculated by FEM model is much smaller than the analytic and less than the TBE one. Meanwhile, for the equal-field comparison, the analytical and FEM results in Fig.2.9b predict that the IDE actuator will have larger deflection than the TBE actuator at a certain ratio of finger width and spacing i.e., $a/T = 0.9$ and $T = 40\mu$m.

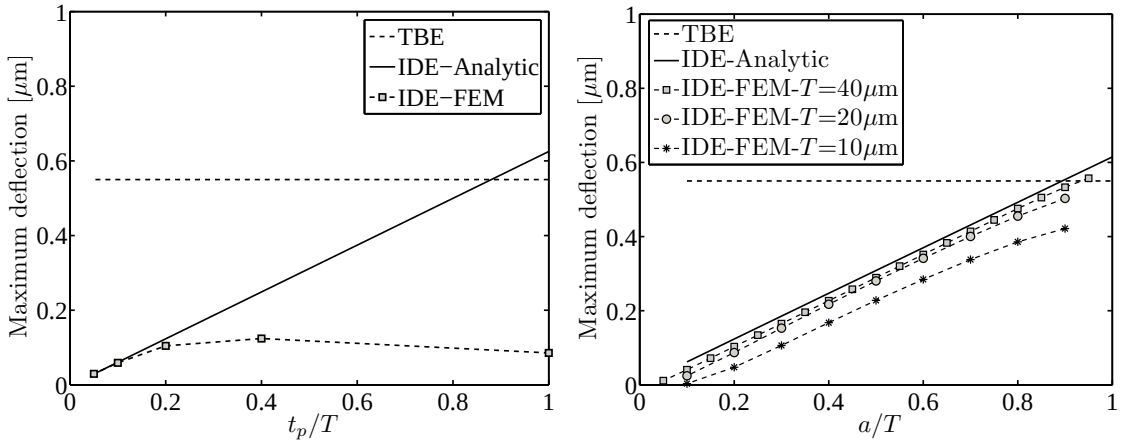

(a) Equal voltage at VTBE=VIDE=10V (b) Equal electric field with VTBE=10V

Figure 2.9: IDE and TBE cantilever actuators comparison. For the IDE, the finger spacings and finger widths are a = b = T/2. The transducer length is Ropt = 270um. The thickness of the piezoelectric layer is t_p = 2um.

5.2 Discussion

The ratios (2.58) and (2.63) can be further simplified if the number of active regions N is large enough and the structure thickness is dominant by the substrate. The second simplification leads to $Y_b I_b \approx \hat{K} \approx \hat{K}_2$ and $\bar{z}_{p,\mathrm{IDE}} \approx \bar{z}_{p,\mathrm{TBE}} \approx (t_p + t_b)/2$. With both simplifications, we can show that the cantilever and the clamped-clamped beam have identical ratios. We define these ratios as figures of merit (FOMs): FOM_V for the equal-voltage comparison and FOM_E for the equal-field comparison

$$\mathrm{FOM}_V \approx \begin{cases} \left| \frac{s_{11}^E}{s_{33}^E} \times \frac{d_{33}}{d_{31}} \right| \times \frac{t_p}{T} & \text{Narrow beam,} \\ \left| \frac{s_{11,\mathrm{eff}}^E}{s_{33,\mathrm{eff}}^E} \times \frac{d_{33,\mathrm{eff}}}{d_{31,\mathrm{eff}}} \right| \times \frac{t_p}{T} & \text{Wide beam,} \end{cases} \tag{2.64}$$

and

$$\mathrm{FOM}_E \approx \begin{cases} \left| \frac{s_{11}^E}{s_{33}^E} \times \frac{d_{33}}{d_{31}} \right| \times \frac{a}{T} & \text{Narrow beam,} \\ \left| \frac{s_{11,\mathrm{eff}}^E}{s_{33,\mathrm{eff}}^E} \times \frac{d_{33,\mathrm{eff}}}{d_{31,\mathrm{eff}}} \right| \times \frac{a}{T} & \text{Wide beam.} \end{cases} \tag{2.65}$$

The FOMs in (2.64) and (2.65) are dependent on material properties and a few mechanical dimensions. Using these one can determine which is the appropriate actuator design, the TBE or the IDE actuator, for a specific application.

In the equal-voltage results in Figs. 2.7a and 2.9a show no parameter range where the IDE is beneficial. This conclusion based on the numerical analysis can be further substantiated by considering the figure of merit in (2.64). For very small t_p/T the FOM goes to zero, but we can estimate the value of t_p/T that makes $\mathrm{FOM}_V > 1$ and hence the IDE beneficial. We find that $t_p/T \geq |s_{33}^E d_{31}|/|s_{11}^E d_{33}| \approx 0.65$, where we used the previously given parameters and, since it gives the lowest value, the narrow-beam equations. However, in this range of value, performance of the IDE beam receive detrimental effects. The reason is the inhomogeneous electric-field distribution. This will be discuss more detail in the next section.

For the equal-field comparison, increasing the ratio between the finger spacing and the pitch in the IDE actuator increases $\mathrm{FOM_E}$. Depending on the properties of the PZT materials, the TBE or the IDE design can be chosen. Using the material

Table 2.2: The FOM's pre-factor of different piezoelectric material

Material	$\left\lvert\frac{s^E_{11}}{s^E_{33}} \times \frac{d_{33}}{d_{31}}\right\rvert$	$\left\lvert\frac{s^E_{11,\text{eff}}}{s^E_{33,\text{eff}}} \times \frac{d_{33,\text{eff}}}{d_{31,\text{eff}}}\right\rvert$	References
PZT-5A	1.9	1.19	[49]
PZT-5H	1.73	1.18	[49]
PZT- 3203HD	1.57	1.07	[112]
PZT-45/55	2.06	1.35	[50, 52]
PZT-53/47	1.55	0.99	[50--52]
PZT 60/40	2.26	1.57	[50, 52]
PZN-PT	1.57	1.01	[53]
PMN-PT	1.22	1.02	[54]

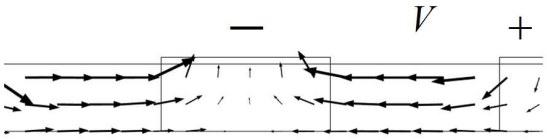

Figure 2.10: Inhomogeneous field distribution inside piezoelectric sheet.

parameters in Table 2.1, $\left\lvert\frac{s^E_{11,\text{eff}}}{s^E_{33,\text{eff}}} \times \frac{d_{33,\text{eff}}}{d_{31,\text{eff}}}\right\rvert \approx 1$ and $\left\lvert\frac{s^E_{11}}{s^E_{33}} \times \frac{d_{33}}{d_{31}}\right\rvert \approx 1.55$ respectively for wide and narrow beams. With thin piezoelectric films and the narrow beam, there is always a value of a/T that make FOM_E (2.65) larger than 1 and hence the IDE beneficial. For the wide beam, these material parameters do not favor the IDE configuration. However, for our case in Fig. 2.7b and Fig. 2.9b, the IDE configuration is preferable with an appropriate choice of a/T, i.e., 0.8 and 0.9 respectively for the cantilever and the clamped-clamped wide-beam. These are both very close to one. This can be understood from the thickness ratio between the piezoelectric layer and the structural layer being 1:10. In this case, the thin-film simplification $Y_b I_b \approx \hat{K} \approx \hat{K}_2$ is not so good.

In the experimental study [57], comparison between TBE and IDE beam has been conducted. An 500nm PZT-film deposited on a structural layer with the whole wafer thickness (approximately 500um) satisfies well the thin-film simplification. The comparable e coefficients, which are the ratios between the d and s coefficients, of $\pm 15\text{C/m}^2$ for the TBE and IDE actuators lead to $\text{FOM}_\text{E}=a/T$ which is always less than one. These figures of merit explain their conclusion that the IDE actuator has no advantage in converse mode.

The piezoelectric material constants vary slightly in the literature as shown in Table 2.2. The $\left\lvert\frac{s^E_{11,\text{eff}}}{s^E_{33,\text{eff}}} \times \frac{d_{33,\text{eff}}}{d_{31,\text{eff}}}\right\rvert$ are varied from 1 to 1.57 which predicting a somewhat higher deflection of the IDE structure relative to the TBE structure for the equal-field comparison.

6 Effect of the non-uniform field on the IDE beam

In previous section, the analysis of IDE transducer assumes that the electric field has an uniform distribution Fig.2.5. This assumption leads to the solution of the coupling constant (2.48) and the capacitance (2.50). The assumption is applicable when the

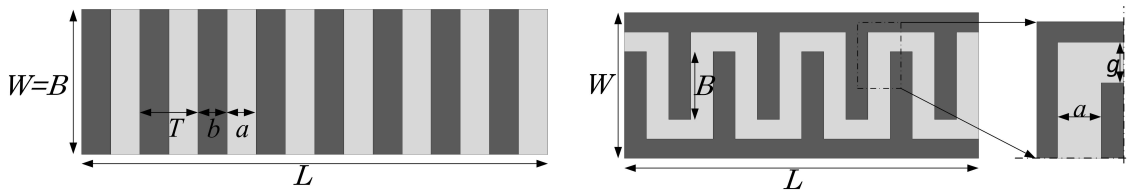

(a) Symmetric configuration (b) Asymmetric configuration

Figure 2.11: Two configurations of the IDE (a) without interconnection lines and (b) with interconnection lines. The dark areas are metal electrodes.

thickness ratio of the piezoelectric layer to the pitch is small. For larger ratios, the FEM results are not well reproduced by these analytic models e.g., Figs 2.7a and 2.9a. The explanation is the non-uniform distribution of the electric field [94] as shown in Fig.2.10.

In this section, effects of the non-uniform field on the IDE beam are investigated. A mathematical approach named conformal mapping technique (CMT) can help to explore the physic. There are several studies using the CMT to solve the non-uniform field problem. However, these works limit for either isotropic [88--90] or anisotropic dielectric [86, 87] material without the piezoelectric effect. Hence, section 6.1 focuses to adapt these available CMTs to anisotropic piezoelectric materials in a parallel-strip structure. Section 6.2 discusses the non-uniform field and its effects on the transducer coupling constant. Section 6.3 presents a new analytic approach to handle the further complexity that arises for the IDE structure when both end-effects and the anisotropy of piezoelectric material are taken into account.

6.1 Capacitance model in an anisotropic piezoelectric material

In this section, the top surface of the IDE device Fig.2.1b has the symmetric configuration without busbars as shown in Fig.2.11a. Starting from Gauss law $\nabla \cdot \vec{D} = 0$, the piezoelectric constitutive equations and thin beam simplification, equation for the electric field in the active regions of the piezoelectric layer with narrow-beam parameters is

$$\varepsilon_{33}^{T} \frac{\partial E_x}{\partial x} + \varepsilon_{11}^{T} \frac{\partial E_z}{\partial z} + d_{33} \frac{\partial T_p(x,z)}{\partial x} = 0. \tag{2.66}$$

If d_{33} equals zero or the stress is constant along the x direction, the last term in (2.66) is zero. This simpler problem can be found in the literature [86], [87]. Without this simplification, (2.66) is rewritten using (2.9) to yield

$$\varepsilon_{33}^{T}(1-\kappa_{33}^{2}) \frac{\partial E_x}{\partial x} + \varepsilon_{11}^{T} \frac{\partial E_z}{\partial z} + \frac{d_{33}}{s_{33}^{E}} \frac{\partial S(x,z)}{\partial x} = 0. \tag{2.67}$$

Neglecting the contribution of the axial strain, the strain term in (2.67) can be replaced by the second derivative using (2.8), i.e.,

$$S(x,z) \approx -z \frac{\partial^2 w}{\partial x^2}. \tag{2.68}$$

Inserting (2.68) into (2.9) for the stress, the resultant moment (2.11) is the integral of the stress. For the mechanically free boundary conditions, the resultant bending

moment (2.11) is zero, we obtain an equation for the second derivative of the defection

$$\frac{\partial^2 w}{\partial x^2} = -\frac{1}{\hat{K}_2}\int_{z_p}^{z_{p+1}} \frac{d_{33}}{s_{33}^E} z E_x \mathrm{d}z. \tag{2.69}$$

If we assume the electric field is uniform, the second derivative (2.69) is back to what we have in (2.40). Otherwise, from (2.68) and (2.69), (2.67) is

$$\varepsilon_{33}^T(1-\kappa_{33}^2)\frac{\partial E_x}{\partial x} + \varepsilon_{11}^T \frac{\partial E_z}{\partial z} + \frac{z d_{33}^2}{\hat{K}_2 (s_{33}^E)^2}\frac{\partial}{\partial x}\int_{z_p}^{z_{p+1}} z E_x \mathrm{d}z = 0. \tag{2.70}$$

We now treat the electric field component E_x as z-independent in the integral. This approximation is valid when the thickness of the piezoelectric film is much smaller than the active gap. Equation (2.70) then becomes

$$\varepsilon_{33}^T\left[1 + \left(z\frac{\bar{z}_p t_p}{\hat{K}_2 s_{33}^E} - 1\right)\kappa_{33}^2\right]\frac{\partial E_x}{\partial x} + \varepsilon_{11}^T\frac{\partial E_z}{\partial z} = 0. \tag{2.71}$$

This equation has the appearance of a two-dimensional Gauss law with spatially varying permittivity. However, since the thickness of the piezoelectric layer is much smaller than the supporting layer, this variation is negligible. We therefore make the further approximation $z = \bar{z}_p$ in the bracket and (2.71) becomes

$$\varepsilon_{33,\mathrm{eff}}\frac{\partial E_x}{\partial x} + \varepsilon_{11}^T\frac{\partial E_z}{\partial z} = 0. \tag{2.72}$$

Note that the effective permittivity $\varepsilon_{33,\mathrm{eff}}$ here is the same quantity (2.51) that we encountered when analyzing the free capacitance (2.50) using a simpler field assumption. With (2.72), the capacitance can now be calculated more accurately.

From the field-potential relation $E_i = -\partial\varphi/\partial x_i$, (2.72) becomes

$$\frac{\partial^2\varphi}{\partial x^2} + \frac{\varepsilon_{11}^T}{\varepsilon_{33,\mathrm{eff}}}\frac{\partial^2\varphi}{\partial z^2} = 0. \tag{2.73}$$

We make a change of coordinates from (x, z) to $(x, \hat{z})$ such that $\hat{z} = \hat{z}_m + \sqrt{\varepsilon_{33,\mathrm{eff}}/\varepsilon_{11}^T}(z - z_m)$ within layer no. m and $\hat{z}_m$ are constants that make the transformation continuous. With $\varphi(x, z) = \hat{\varphi}(x, \hat{z})$, (2.73) becomes

$$\frac{\partial^2\hat{\varphi}}{\partial x^2} + \frac{\partial^2\hat{\varphi}}{\partial\hat{z}^2} = 0 \tag{2.74}$$

within each layer.

The continuity condition on the normal electric displacement at the interfaces between the piezoelectric and other layers should be valid before and after transformation. Hence,

$$\varepsilon_{11}^T\frac{\partial\varphi}{\partial z} = \sqrt{\varepsilon_{33,\mathrm{eff}}\varepsilon_{11}^T}\frac{\partial\hat{\varphi}}{\partial\hat{z}} \tag{2.75}$$

must be continuous at z_p ($\hat{z}_p$) and z_{p+1} ($\hat{z}_{p+1}$). The quantity $\varepsilon_{\mathrm{eq}} = \sqrt{\varepsilon_{33,\mathrm{eff}}\varepsilon_{11}^T}$ is treated as an equivalent relative permittivity inside the piezoelectric layer. This means that the anisotropic dielectric material in the (x, z) coordinate systems can be treated as an isotropic dielectric in the $(x, \hat{z})$ coordinate system. The equivalent parameters are the relative permittivity $\varepsilon_{\mathrm{eq}}$, and the dielectric thickness

$\hat{t}_p = t_p\sqrt{\varepsilon_{33,\text{eff}}/\varepsilon_{11}^T}$. Once this transformation is made, the capacitance can be calculated by a CMT approach, e.g., Gevorgian's models [89] or Igreja's [90].

We now apply the CMT [90] to calculate the capacitance of the symmetric IDE structure Fig.2.11a. The gap and pitch are $a = 3T/4 = 30\mu$m, the glass substrate thickness is fixed at $t_p = 20\mu$m. The Youngs modulus and Poissons ratio and the relative permittivity of the glass are 74GPa, 0.3 and 4.2 respectively. The piezoelectric material properties are given in Table 2.1. As mentioned in [90], the capacitances of other layers i.e., glass and air, can be taken into account using the partial capacitance method. With our numerical values, including the high relative permittivity of the piezoelectric material, the total parasitic capacitance from the air and glass layer is less than 10% of the piezoelectric contribution to capacitance if the piezoelectric layer thickness is more than 2.5% (500nm) of the glass thickness. In typical thin-film applications with piezoelectric layer thickness ranging from 1 to 4 μm, the total parasitic capacitance accounts for only 1.25% to 5% of the capacitance. Hence, these parasitic capacitances can be neglected.

The capacitance of the piezoelectric film with the IDE configuration is

$$C = \frac{N}{2}\varepsilon_{\text{eq}}\frac{K(k_{\text{I}})}{K(k_{\text{I}}')} \tag{2.76}$$

where N is the number of active regions, $K(k_{\text{I}})$ is the complete elliptic integral of the first kind and $K(k_{\text{I}})/K(k_{\text{I}}')$ is the elliptic integral ratio as a function of the elliptic modulus

$$k_{\text{I}} = \sqrt{1-k_{\text{I}}'^2} = \frac{\text{sn}\left(K(k)\frac{b}{a+b},k\right)\sqrt{1-k^2}}{\sqrt{1-k^2\text{sn}^2\left(K(k)\frac{b}{a+b},k\right)}} \tag{2.77}$$

where $\text{sn}(u,k)$ is the sine amplitude Jacobi elliptic function [113].

The elliptic moduli k and $k' = \sqrt{1-k^2}$ are obtained from the relation

$$\frac{K(k')}{K(k)} = \frac{2\hat{t}_p}{a+b}. \tag{2.78}$$

Hence,

$$k = \left(\frac{\vartheta_2(0,q_1)}{\vartheta_3(0,q_1)}\right)^2, \tag{2.79}$$

where $\vartheta_2(u,q)$ and $\vartheta_3(u,q)$ is the Jacobi theta functions [113] with

$$q_1 = \exp(-\pi K(k')/K(k)) = \exp(-2\pi\hat{t}_p/(a+b)). \tag{2.80}$$

The elliptic moduli can also be found from (2.78) by using the Hilberg approximation [114]

$$\frac{K(k)}{K(k')} \approx \frac{2}{\pi}\ln\left(2\sqrt{\frac{1+k}{1-k}}\right) \quad \text{for} \quad 1 \le \frac{K(k)}{K'(k)} \le \infty \quad \text{or} \quad \frac{1}{\sqrt{2}} \le k \le 1, \tag{2.81}$$

$$\frac{K(k)}{K(k')} \approx \frac{\pi}{2}/\ln\left(2\sqrt{\frac{1+k'}{1-k'}}\right) \quad \text{for} \quad 0 \le \frac{K(k)}{K'(k)} \le 1 \quad \text{or} \quad 0 \le k \le \frac{1}{\sqrt{2}}. \tag{2.82}$$

Hence,

$$k \approx \frac{q_2-4}{q_2+4} \quad \text{for} \quad 1 \le \frac{K(k)}{K'(k)} \le \infty \quad \text{or} \quad \frac{1}{\sqrt{2}} \le k \le 1, \tag{2.83}$$

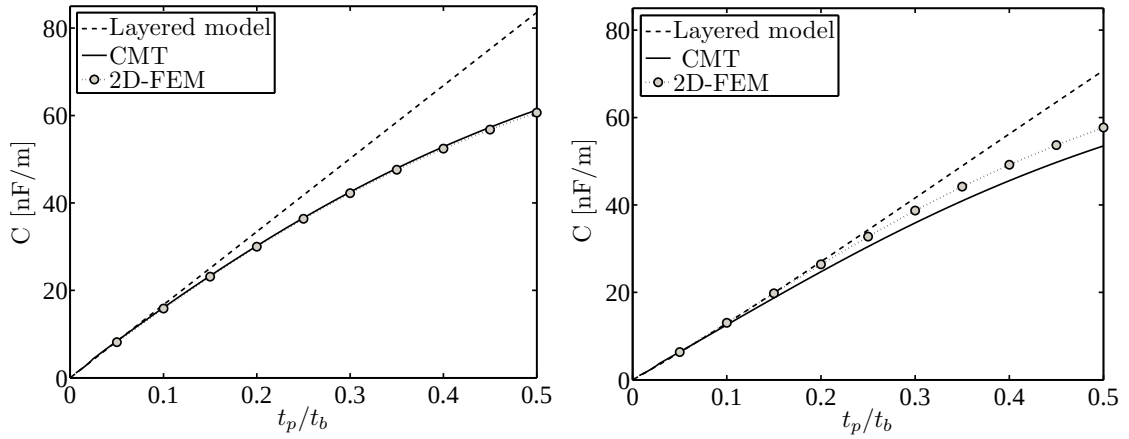

(a) All d_{ij} are set to 0 (b) All d_{ij} are set to the material values

Figure 2.12: Capacitance per unit width of the symmetric IDE piezoelectric beam. The finger spacings and finger widths are a = 3b = 3T/4=30um. The thickness of the substrate layer is fixed t_p = 20um.

$$k' \approx \frac{1-4q_1}{1+4q_1} \quad \text{for} \quad 0 \le \frac{K(k)}{K'(k)} \le 1 \quad \text{or} \quad 0 \le k \le \frac{1}{\sqrt{2}}. \tag{2.84}$$

The two conditions for the value of the ratio $K(k)/K'(k)$ and the value of k are similar. Here, we write $K'(k) = K(k')$, q_1 is given in (2.80) and

$$q_2 = \exp(\pi K(k)/K'(k)) = \exp(\pi(a+b)/(2t_p)). \tag{2.85}$$

Figure 2.12a presents the capacitance of the symmetric IDE structure calculated with different methods: the layered model (2.50), the CMT model, and a 2D FEM model for the narrow- beam parameters. Here, all piezoelectric coupling constants d_{ij} are artificially set to zero in order to first understand the electrostatics. In the CMT model, the piezoelectric layer is treated as isotropic material with $\varepsilon_{\text{eq}} = \sqrt{\varepsilon_{33,\text{eff}}\varepsilon_{11}^T}$ (2.76) and $\hat{t}_p = t_p\sqrt{\varepsilon_{33,\text{eff}}/\varepsilon_{11}^T}$ (2.80, 2.85).

In Fig.2.12a, the layered model predicts a linear relationship between the capacitance and the dielectric thickness because of the assumption of a uniform field distribution (Fig.2.5). The CMT and FEM results are almost identical. The two models predict smaller capacitances than the layered model. The differences increase with piezoelectric thickness and deviate from the simple linear relationship due to non-uniform electrostatic field.

In Fig.2.12b, we reinstated the correct values of the piezoelectric coupling constants d_{ij}. In Fig.2.12b, we observe smaller capacitances than in Fig.2.12a. The effect is contained in $\varepsilon_{33,\text{eff}}$ (2.51) which also appears in (2.72). For nonzero coupling it differs from ε_{33}^T and is dependent on the flexural-rigidity ratio.

6.2 Electric field and coupling constant for the symmetric IDE configuration

Using the conformal mapping transformations as in [90] for our problem (2.74), the electric field in a representative segment of the IDE structure Fig.2.13 is derived.

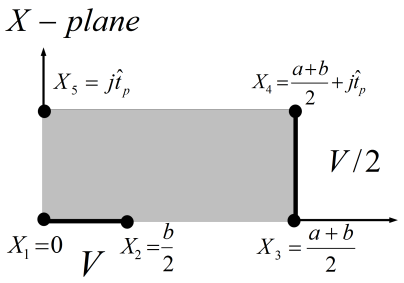

Figure 2.13: A representative segment of IDE. The imaginary axis is at the centre of the electrode fingers while the real axis is on the interface between piezoelectric material and the electrodes.

Representing the two-dimensional electric field by a complex number, it becomes

$$\mathbf{E} = -\frac{\partial \hat{\varphi}}{\partial X}. \tag{2.86}$$

The conformal transformations and the mapping functions are shown in Fig.2.14. Using the chain rules for the derivative, we can write

$$\mathbf{E} = -\frac{\partial \hat{\varphi}_w}{\partial W}\frac{\partial W}{\partial Y}\frac{\partial Y}{\partial T}\frac{\partial T}{\partial Z}\frac{\partial Z}{\partial X} \tag{2.87}$$

with X, Z, T, Y and W are complex variables respectively in the X, Z, T, Y and W-*plane* in Fig 2.14. The derivative $\partial\hat{\varphi}_w/\partial W = -jV/(2K(k_I'))$ is the electric field between the two parallel strip lines in the $W-$*plane*. Other derivatives are

$$\frac{\partial W}{\partial Y} = \frac{1}{\sqrt{(1-Y^2)(1-k_I^2Y^2)}}, \tag{2.88}$$

$$\frac{\partial Y}{\partial T} = \frac{T_4^2\sqrt{T_4^2-T_2^2}}{T_2\sqrt{(T_4^2-T^2)^3}}, \tag{2.89}$$

$$\frac{\partial T}{\partial Z} = \mathrm{cn}(Z,k)\mathrm{dn}(Z,k), \tag{2.90}$$

and

$$\frac{\partial Z}{\partial X} = \frac{2K(k)}{a+b} \tag{2.91}$$

where T_4 and T_2 are given in Fig.2.14, $\mathrm{cn}(u,k)$ and $\mathrm{dn}(u,k)$ are cosine and delta amplitude of the Jacobi elliptic function [113]. The elliptic moduli k and k_I' are given respectively in (2.79) and (2.77).

Substituting $\partial\hat{\varphi}_w/\partial W = -jV/(2K(k_I'))$ and (2.88, 2.89, 2.90, 2.91) into (2.87), denoting $q(X) = \mathrm{sn}\left(\frac{2K(k)X}{a+b}, k\right)$ and noting that $\mathrm{cn}^2(Z,k) + \mathrm{sn}^2(Z,k) = 1$ and $\mathrm{dn}^2(Z,k) + k^2\mathrm{sn}^2(Z,k) = 1$, the electric field is

$$\mathbf{E} = j\frac{V}{a+b}\frac{K(k)}{K(k_1')}\frac{\sqrt{1-k^2q(X_2)^2}}{\sqrt{q(X_2)^2-q(X)^2}}. \tag{2.92}$$

As the electric field inside the representative segment is known, the electric field at other position of the piezoelectric layer can be found by symmetry.

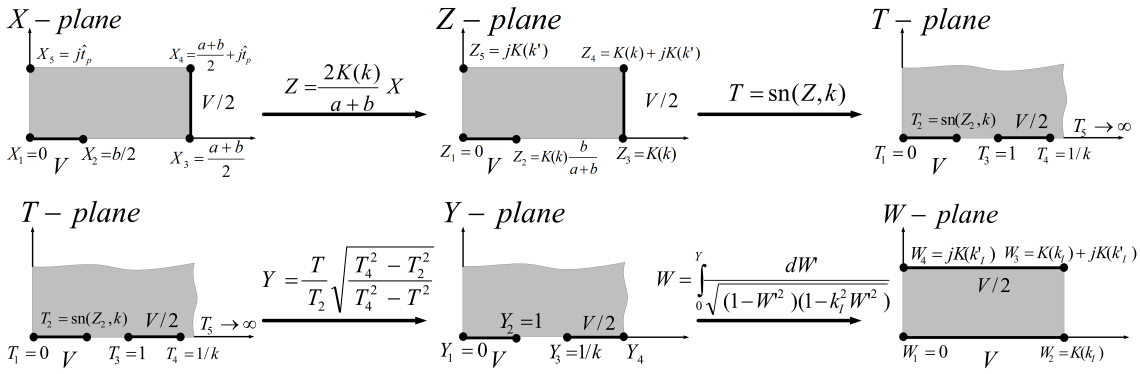

Figure 2.14: The conformal mapping series [90] to transform the representative segment of the IDE to a parallel strip lines.

For the coupling constant ζ, (2.69) shows that only the x-component of the electric field is of concern. In section 6.1, the effective permittivity was approximated by the value at $z = \bar{z}_p$. Hence, the electric field at $z = \bar{z}_p$ is of interest. In the representative segment, this field is expressed as

$$E_x = \mathrm{Re}\{\mathbf{E}\left[\mathrm{real}(X) + j\hat{t}_p/2\right]\}. \tag{2.93}$$

A phenomenological quadratic model (PQ model) is fitted to E_x, i.e.,

$$\begin{aligned} E_x &= \gamma\left[1 - \frac{4\beta}{a^2}\left(x - (nT+b) - \frac{a}{2}\right)^2\right] \times \frac{V}{a} \\ &\qquad \text{for} \quad nT + b \le x < (n+1)T \\ E_x &= 0 \quad \text{elsewhere} \end{aligned} \tag{2.94}$$

where n is a positive integer. The dimensionless quantity β parametrizes the flatness while γ parametrizes the mid-gap electric field value. These quantities can be found by fitting (2.94) at $x = nT + b + a/2$ and $x = nT + b$ with the CMT model (2.93) at $X = (a+b)/2 + j\hat{t}_p/2$ and $X = b/2 + j\hat{t}_p/2$. The result is

$$\gamma = \mathrm{Re}\left[\mathbf{E}\left(\frac{a+b}{2} + j\frac{\hat{t}_p}{2}\right)\right] \times \frac{a}{V}, \tag{2.95}$$

$$\beta = 1 - \mathrm{Re}\left[\mathbf{E}\left(\frac{b}{2} + j\frac{\hat{t}_p}{2}\right)\right] / \mathrm{Re}\left[\mathbf{E}\left(\frac{a+b}{2} + j\frac{\hat{t}_p}{2}\right)\right]. \tag{2.96}$$

Since the PQ model (2.94) is z-independent, taking this term out of the z-integration (2.69), integrating twice along the x-direction and dividing the result by the applied voltage V, the transducer's coupling constant ζ is expressed as [111]

$$\zeta = \gamma\left(1 - \frac{\beta}{3}\right)\frac{\bar{z}_p t_p d_{33}}{s_{33}^E \hat{K}_2}\frac{N^2 a}{2}\left(1 + \left(1 + \frac{1}{N}\right)\frac{b}{a} + \frac{2}{N}\right). \tag{2.97}$$

The electromechanical coupling factor (2.2) can be calculated since the short-circuit stiffness (2.54), the free capacitance (2.76) and ζ (2.97) are known.

For numerical study, the same parameters of the symmetry IDE structure Fig.2.11a in section 6.1 is investigated. The x-component of the electric field is shown in Fig.2.15. The FEM and CMT results show that the electric field decreases

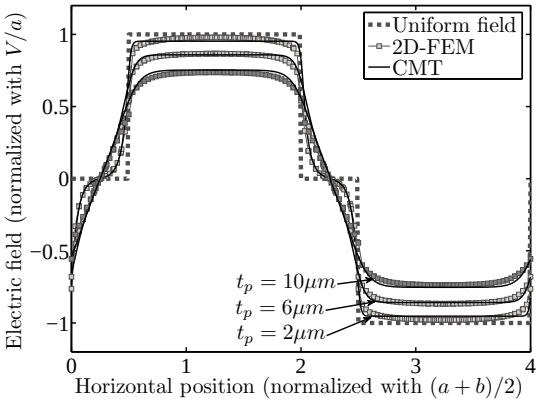

Figure 2.15: Different models of the electric field along the insets dotted line at the middle of the piezoelectric layer

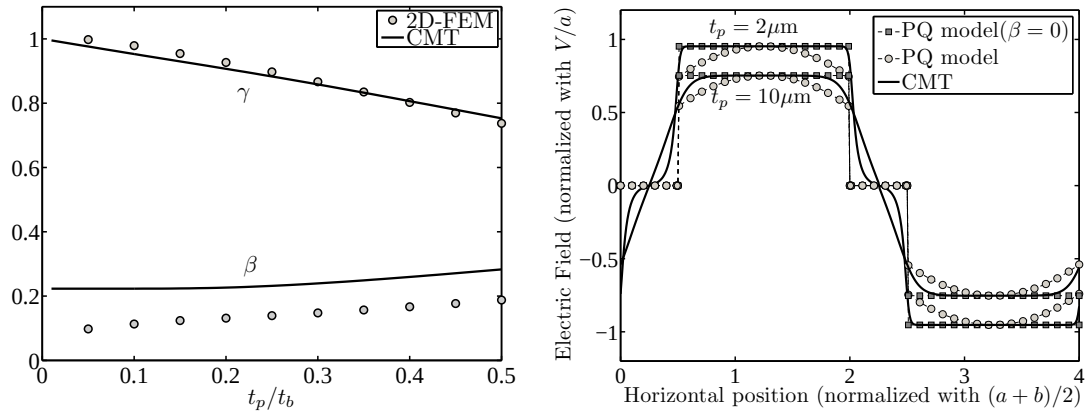

(a) Fitting parameters of the PQ model.

(b) The PQ model results.

Figure 2.16: Fitting parameters of the phenomenological quadratic model electric field model (PQ model) with 2D-FEM and CMT model (a) and the comparison between PQ models and CMT (b).

if the piezoelectric layer thickness increase. The electric field calculated by the uniform field model is higher than the CMT and the FEM results.

The parameters γ and β for the phenomenological quadratic model (PQ model) (2.94) can be extracted from the CMT or FEM curves in Fig.2.15 using field values at the center and boundary of the active region as previously described for the CMT in (2.95) and (2.96). The results are shown in Fig.2.16a for different piezoelectric thicknesses. The coefficient γ parametrizing the field at the center of the active regions is always less than one and decreases with the piezoelectric layer thickness. Hence, the uniform field model always overestimates the electric field. The overestimation increases with the thickness of the piezoelectric layer. The coefficient β parametrizing the flatness increases with the piezoelectric layer thickness. Hence, the quadratic term becomes more important for the thick piezoelectric layer.

The comparison between the PQ model (2.94) and the CMT is shown in Fig.2.16b. For both cases, especially with the thinner piezoelectric layer, the electric field curve is flat in most of the active region and there is a sharp drop around the edges of the electrode. Hence, the quadratic form does not fit well. We observed that the PQ model (2.94) without the quadratic term, or $\beta = 0$, fits better with the CMT results.

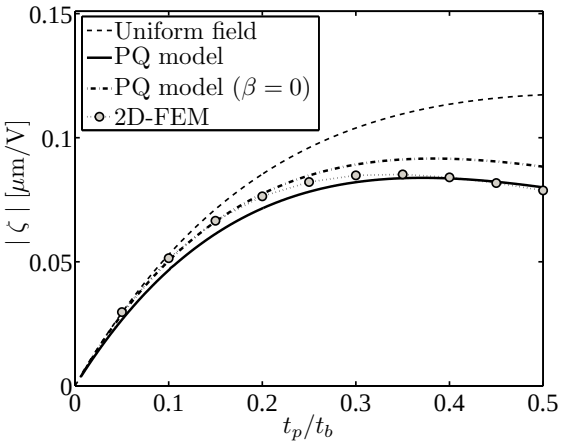

Figure 2.17: The coupling constant of the symmetric IDE piezoelectric narrow beam with different electric field model.

Figure 2.17 shows how the electric field affects the coupling constant ζ. The phenomenological model (2.97) (both with β equal to or different from zero) is closest to the FEM results. In the most interesting thickness range, i.e., $t_p \leq 0.2t_b = 4\mu$m, (2.97) with $\beta = 0$ is closest to the FEM results. Because the uniform field model always overestimates the electric field, it also overestimates the coupling constant ζ. However, in the thickness range $t_p \leq 0.1t_b = 2\mu$m, since γ is approximately one in Fig.2.16a, the results of the uniform field and the fitted model (2.97) with $\beta = 0$ are both good approximations.

6.3 Capacitance model for the the asymmetric IDE configuration

Typically, the IDE devices are asymmetric due to interconnection lines as shown in Fig.2.11b. The electrostatic field is complicated around the tip regions of the electrode fingers. The parasitic capacitances contributed from these regions are very different from the values calculated by the parallel plate model. An accurate capacitance calculation should include both field distributions on the IDE surface and inside into the dielectric material. This three dimensional (3D) problem is out of reach of the CMT because the mapping theory only applies to the two dimensional (2D) problems. Therefore, for simplicity, a uniform electrostatic field distribution across the dielectric thickness is assumed. The assumption is suitable for a structure with dielectric thickness much smaller than the IDE pitch. Then the 3D problem is simplified to a 2D problem, which can be solved by the CMT.

From Fig.2.11b, if we know the capacitance C_n of the small part shown in the inset, the positive integer n indicates the n^{th} active region, the total capacitance C of the IDE device with N active regions is

$$C = 2NC_nt_p. \tag{2.98}$$

To transform the complicated polygonal shape around a corner to a simple rectangle, we apply the conformal transformation in Fig.2.18 transforming the small part to a parallel plate capacitor. Then, C_n can be calculated by applying the parallel-plate formula to the rectangle.

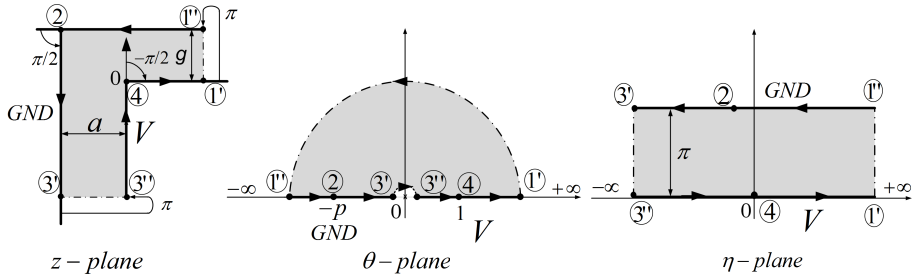

Figure 2.18: Conformal mapping flow to transform a polygon into parallel strip lines.

The transformation flow in Fig.2.18 requires two transform steps. First, the polygon in z-plane is mapped to the upper half-plane in θ-plane via the Schwartz-Christoffel (SC) [115] derivative

$$\frac{\mathrm{d}z}{\mathrm{d}\theta} = c_0 \frac{\sqrt{\theta - 1}}{\theta\sqrt{\theta + p}} \tag{2.99}$$

where the origin $z = 0$ is chosen at the corner of the IDE finger and is mapped to $\theta = 1$. The constants $c_0 = g/\pi$ and $p = g^2/a^2$ are found by mapping relations given in equations (27.17) and (27.22) of [115]. The integral of (2.99) is

$$z = c_0 \left[2\sinh^{-1}\sqrt{\frac{\theta - 1}{p + 1}} - \frac{2\tan^{-1}\sqrt{\frac{p(\theta-1)}{\theta+p}}}{\sqrt{p}} \right]. \tag{2.100}$$

In the second step, the upper-half θ-plane is mapped to a strip between two parallel lines in the η-plane via a mapping function $\eta = \ln(\theta)$. Hence, the capacitance is

$$C_n = \frac{\varepsilon_r \varepsilon_0 (\eta_{1'} - \eta_{3''})}{\pi} = \frac{\varepsilon_r \varepsilon_0}{\pi} \ln \frac{\theta_{1'}}{\theta_{3''}} \tag{2.101}$$

where $\theta_{1'}, \theta_{3''}$ respectively are images of $z_{1'}, z_{3''}$ in the θ-plane. These values can be found in (2.100). ε_r is the relative permittivity of the dielectric layer while ε_0 is the vacuum permittivity.

Equation (2.101) only applies directly to an isotropic material. For an anisotropic material that is homogeneous and has the principal directions of the permittivity orthogonal or parallel to the polygonal faces, we can first use the transformation in section 6.1, introducing an effective permittivity and effective dimensions, to make the problem isotropic.

For the IDE, the polarization direction (3-axis) changes around the corner of a finger as indicated in Fig.2.19a. The orientation of the permittivity tensor follows the direction of polarization. In order to apply the transformation we therefore split the problem of calculating the capacitance C_n into two simpler capacitance problems as indicated in the figure. That is, we approximate $C_n \approx C_{n1} + C_{n2}$ where C_{n1} and C_{n2} are the contributions to C_n related to charges on the thick black lines in Fig.2.19b and Fig.2.19c respectively.

When calculating each of the partial capacitances C_{n1} and C_{n2}, we treat the polarization as uniform as shown in the figure. The largest deviations in assumed permittivity from the stated problem are then found in the regions of the corner with the smallest electric flux density. By this, we expect to have included the dominant contributions to the capacitance and some of the fringing-field effects.

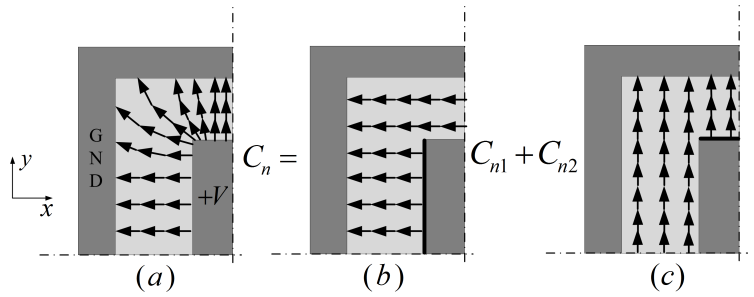

Figure 2.19: Capacitance C_n is split into two different partial capacitances C_{n1} and C_{n2}. Each of these has uniform polarization direction as it is shown.

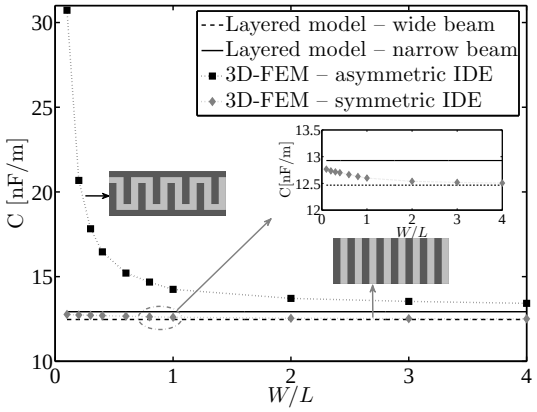

Figure 2.20: Capacitance per overlap width B of the symmetric - asymmetric IDE device at $g = 5\mu$m.

To summarize: each of the partial capacitances is calculated by a transformation to an isotropic problem as in section 6.1 followed by the mapping flow in Fig.2.18. The capacitances C_{n1} and C_{n2} correspond to the two parallel capacitances on the left and the right half-plane of the η-plane separated by the imaginary axis. These capacitances can be calculated using (2.101)

$$C_{n1} = \frac{\varepsilon_{n1}}{\pi} \ln \frac{1}{\theta_{n1,3''}}; \quad C_{n2} = \frac{\varepsilon_{n2}}{\pi} \ln \theta_{n2,1'} \tag{2.102}$$

where $\theta_{n1,3''}$ is the image of $z_{3''}$ in the θ-plane of C_{n1}, $\theta_{n2,1'}$ is the image of $z_{1'}$ in the θ-plane of C_{n2}. The permittivity $\varepsilon_{n1}, \varepsilon_{n2}$ correspond to the different polarization orientations for C_{n1} and C_{n2} respectively.

For numerical study, IDE beam studied in this section has an asymmetric electrode structure due to the interconnect lines shown in Fig.2.11b. As discussed, the CMT is applicable if the electrostatic field is uniformly distributed across the piezoelectric layer thickness. We observed in section 6.2 that the field distribution can be assumed uniform if the piezoelectric layer thickness is in the range $t_p \leq 0.1 t_b$. We choose the beam with dimensions $t_p = t_b/10 = 2\mu$m and keep the gap and the pitch values, i.e., $a = 3T/4 = 30\mu$m.

For the CMT model, the partial capacitances C_{n1} and C_{n2} in Fig.2.19 are calculated with the equivalent permittivity ε_{n1} and ε_{n2} and effective dimensions $\hat{a}$ and $\hat{g}$ as given in Table 2.3. These formulas are derived in the same way as in section 6.1.

Figure 2.20 compares the capacitance per overlap width B of the layered model to the FEM result for the IDE beams with and without interconnect lines. For the

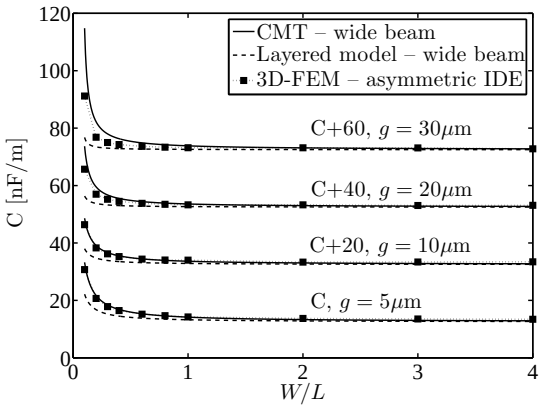

Figure 2.21: Capacitance per overlap width B of the asymmetric IDE device with different end gaps g.

symmetric IDE beam, the two layered-model capacitances with narrow and wide beam parameters set respectively the upper and lower limits of the FEM results. The capacitance of the FEM model decreases asymptotically towards the wide-beam limit as the beam width is increased. This is because the effective dielectric constant decreases from ε_{33}^T to $\varepsilon_{33,\text{eff}}^T$ as shown in Table 2.1.

For the asymmetric IDE beam, additional capacitance around the end gap of the IDE fingers contributes. This explains why the capacitance per overlap width is higher with the asymmetric than with the symmetric IDE.

In order to improve the layered model, we add the capacitance between the end of each electrode finger and the interconnect line. The model of this capacitance is analogous to the inter-electrode capacitance. These models are given in the Table 2.3. The result is compared to CMT and FEM in Fig.2.21. The layered model with narrow-beam parameters is not shown because it is visually indistinguishable from the wide-beam result. The total capacitance per overlap width is still smaller than the FEM results especially if $W/L < 1$. This means there are additional contributions caused by the fringing effects at the corners of the IDE fingers. By applying the CMT technique, these fringing capacitances are taken into account. The CMT model is in a better agreement with the FEM results. Therefore, the CMT model is more accurate than the layered model.

7 Electromechanical coupling factor of the TBE and the IDE transducers

In section 5, the comparison of the beam deflection has been conducted. In this section, we focus on the transducer electromechanical coupling factor. First, numerical calculation of the electromechanical coupling factors of the piezoelectric cantilever with TBE and IDE configurations Fig.2.1 is presented. Then, these values are compared. The electromechanical coupling factor gives information on the conversion efficiency between the electrical and mechanical energy. Normally, the higher conversion efficiency is beneficial in applications such as microsensors, microgenerators.

For the TBE beam, the model of the electromechanical coupling factor is presented in section 2. For the IDE beam, three different analytical models of the

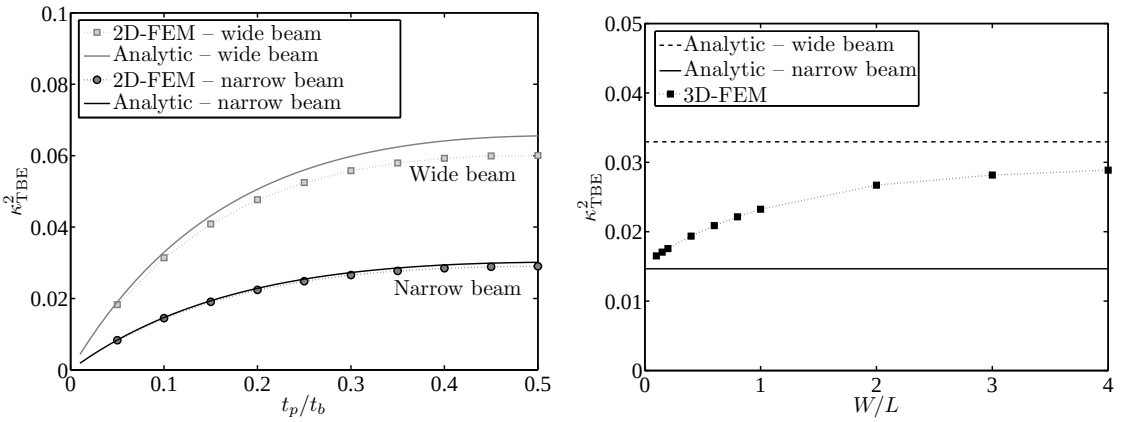

(a) With different piezoelectric layer thickness.

(b) Thin film piezoelectric $t_p/t_b = 0.1$ with different beam width.

Figure 2.22: Electromechanical coupling factor of the TBE device

electromechanical coupling factor are presented. In the first model, the electromechanical coupling factor is calculated using the layered model for the capacitance and the uniform electric field model for the transducer coupling constant as presented in section 4. Secondly, the electromechanical coupling factor is calculated using the CMT model for the capacitance and the PQ model for the transducer coupling constant as presented in section 6.1 and 6.2. Both of these electromechanical coupling factor models are for the symmetric configuration Fig.2.11a. The last electromechanical coupling factor model relates to the thin film piezoelectric beam with the asymmetric configuration Fig.2.11b. The capacitance is calculated using the CMT model in section 6.3 and the coupling constant is calculated using the uniform model in section 4. The necessary formulas to calculate the two-port parameters for different configurations are summarized in Table. 2.3.

We choose a length $L = 1$mm for all the numerical calculations. The cross section of the beam include a structural elastic layer, a piezoelectric sheet and electrode layers. For the structural layer, similar to section 6, we choose $t_b = 20\mu$m thick glass with Young's modulus and Poisson's ratio 74GPa and 0.3 respectively. Glass can be interesting for optical applications. The electrode is 200nm thick platinum with Young's modulus and Poisson's ratio 169GPa and 0.38 respectively. The properties of the piezoelectric material is listed in Table. 2.1.

7.1 TBE beam

Figure 2.22a compares the electromechanical coupling factor of the TBE transducer calculated by 2D FEM simulation and (2.24). Analytical and FEM results are nearly equal. The wide beam transducer has larger electromechanical coupling factor than the narrow one. This is because the y-deformation restriction from narrow to wide beam increases the effective electromechanical coupling factor of the material κ^2_{31} as shown in Table 2.1.

In Fig.2.22b, we consider a finite beam width using a 3D FEM simulation. The numerical electromechanical coupling factor increases monotonically with W from a value near the analytical narrow-beam result and approaches the analytical wide-beam result.

Table 2.3: Analytic model summary

	TBE	**Symmetric IDE**	**Asymmetric IDE**
		Short-circuit stiffness K_s	
Layered model	$\frac{3W\hat{K}}{L^3}$	$\frac{3W\hat{K}_2}{L^3}$	$\frac{3W\hat{K}_2}{L^3}$
Definition	$\hat{K} = \sum_m Y_m \left[\frac{I_m}{1-\kappa_m^2} + t_m \bar{z}_m^2\right]$, $Y_p = \frac{1}{s_{11}^E}$, $\kappa_p^2 = \kappa_{31}^2 = \frac{d_{31}^2}{s_{11}^E \varepsilon_{33}^T}$, $\bar{z}_m = \frac{z_{m+1}+z_m}{2}$, $\sum_m \bar{z}_m Y_m t_m = 0$, $I_m = t_m^3/12$ and $t_m = z_{m+1} - z_m$.	$\hat{K}_2 = \sum_m Y_m \left[I_m + t_m \bar{z}_m^2\right]$, $Y_p = \frac{1}{s_{33}^E}$, $\bar{z}_m = \frac{z_{m+1}+z_m}{2}$, $\sum_m \bar{z}_m Y_m t_m = 0$, $I_m = t_m^3/12$ and $t_m = z_{m+1} - z_m$.	$\hat{K}_2 = \sum_m Y_m \left(I_m + t_m \bar{z}_m^2\right)$, $Y_p = \frac{1}{s_{33}^E}$, $\bar{z}_m = \frac{z_{m+1}+z_m}{2}$, $\sum_m \bar{z}_m Y_m t_m = 0$, $I_m = t_m^3/12$ and $t_m = z_{m+1} - z_m$.
		Free capacitance C	
Layered model	$\varepsilon_{33}^T \left[1 + (\alpha_{31} - 1)\, \kappa_{31}^2\right] \frac{WL}{t_p}$	$N \varepsilon_{33,\text{eff}} \frac{Wt_p}{a}$	$N \left(\varepsilon_{33,\text{eff}} \frac{Bt_p}{a} + \varepsilon_{31,\text{eff}} \frac{bt_p}{g}\right)$
CMT		$\frac{NW}{2} \varepsilon_{eq} \frac{K(k_I)}{K(k_I')}$	$\frac{2Nt_p}{\pi} (\varepsilon_{n1} \ln \frac{1}{\theta_{n1,3''}} + \varepsilon_{n2} \ln \theta_{\text{n2},1'})$
Definition	$\alpha_{31} = \frac{t_p \bar{z}_p^2}{s_{11}^E \hat{K}}$.	$\varepsilon_{33,\text{eff}} = \varepsilon_{33}^T \left[1 + (\alpha_{33} - 1)\, \kappa_{33}^2\right]$, $\alpha_{33} = \frac{t_p \bar{z}_p^2}{s_{33}^E \hat{K}_2}$, $\kappa_{33}^2 = \frac{d_{33}^2}{s_{33}^E \varepsilon_{33}^T}$, $\varepsilon_{eq} = \sqrt{\varepsilon_{33,\text{eff}} \varepsilon_{11}^T}$, $k_\text{I} = \sqrt{1 - k_\text{I}'^2} = \frac{q(b/2)\sqrt{1-k^2}}{\sqrt{1-k^2 q(X_2)^2}}$, $q(X) = \text{sn}\left(\frac{2K(k)X}{a+b}, k\right)$, $k = \sqrt{1-k'^2}$, $\frac{K(k')}{K(k)} = \frac{2\hat{t}_p}{a+b}$, and $\hat{t}_p = t_p \sqrt{\varepsilon_{33,\text{eff}}/\varepsilon_{11}^T}$.	$\varepsilon_{33,\text{eff}} = \varepsilon_{33}^T \left[1 + (\alpha_{33} - 1)\, \kappa_{33}^2\right]$, $\alpha_{33} = \frac{t_p \bar{z}_p^2}{s_{33}^E \hat{K}_2}$, $\kappa_{33}^2 = \frac{d_{33}^2}{s_{33}^E \varepsilon_{33}^T}$, $\varepsilon_{31,\text{eff}} = \varepsilon_{33}^T \left[1 + (\alpha_{31,n2} - 1)\, \kappa_{31}^2\right]$, $\alpha_{31,n2} = \frac{t_p \bar{z}_p^2}{s_{11}^E \hat{K}_2}$, $\kappa_{31}^2 = \frac{d_{31}^2}{s_{11}^E \varepsilon_{33}^T}$, $\varepsilon_{n1} = \sqrt{\varepsilon_{33,\text{eff}} \varepsilon_{11}^T}$, $\varepsilon_{n2} = \sqrt{\varepsilon_{31,\text{eff}} \varepsilon_{11}^T}$, $\theta_{n1,3''}$ is the solution of the following equation $\frac{B}{2} = \frac{g}{\pi} \left[2 \sinh^{-1} \sqrt{\frac{\theta-1}{p_{n1}+1}} - \frac{2 \tan^{-1} \sqrt{\frac{p_{n1}(\theta-1)}{\theta+p_{n1}}}}{\sqrt{p_{n1}}}\right]$ with $p_{n1} = \frac{g^2}{\hat{a}^2}$ and $\hat{a} = a\sqrt{\varepsilon_{11}^T/\varepsilon_{33,\text{eff}}}$. $\theta_{n2,1'}$ is the solution of the following equation $\frac{b}{2} = \frac{\hat{g}}{\pi} \left[2 \sinh^{-1} \sqrt{\frac{\theta-1}{p_{n2}+1}} - \frac{2 \tan^{-1} \sqrt{\frac{p_{n2}(\theta-1)}{\theta+p_{n2}}}}{\sqrt{p_{n2}}}\right]$ with $p_{n2} = \frac{\hat{g}^2}{a^2}$ and $\hat{g} = g\sqrt{\varepsilon_{11}^T/\varepsilon_{31,\text{eff}}}$.
		Coupling constant ζ	
Uniform field	$\frac{\overline{z}_p d_{31}}{s_{11}^E \hat{K}} \frac{L^2}{2}$	$\frac{\overline{z}_p d_{33} t_p}{s_{33}^E \hat{K}_2} \frac{N^2 a}{2} \left(1 + \left(1 + \frac{1}{N}\right) \frac{b}{a} + \frac{2}{N}\right)$	$\frac{\overline{z}_p d_{33} t_p}{s_{33}^E \hat{K}_2} \frac{N^2 a}{2} \left(1 + \left(1 + \frac{1}{N}\right) \frac{b}{a} + \frac{2}{N}\right)$
PQ model ($\beta = 0$)		$\gamma \frac{\overline{z}_p d_{33} t_p}{s_{33}^E \hat{K}_2} \frac{N^2 a}{2} \left(1 + \left(1 + \frac{1}{N}\right) \frac{b}{a} + \frac{2}{N}\right)$	
Definition		$\gamma = \text{Re}\left[\mathbf{E}\left(\frac{a+b}{2} + j\frac{\hat{t}_p}{2}\right)\right] \times \frac{a}{V}$, $\mathbf{E}(X) = j \frac{V}{a+b} \frac{K(k)}{K(k_1')} \frac{\sqrt{1-k^2 q(b/2)^2}}{\sqrt{q(b/2)^2 - q(X)^2}}$	

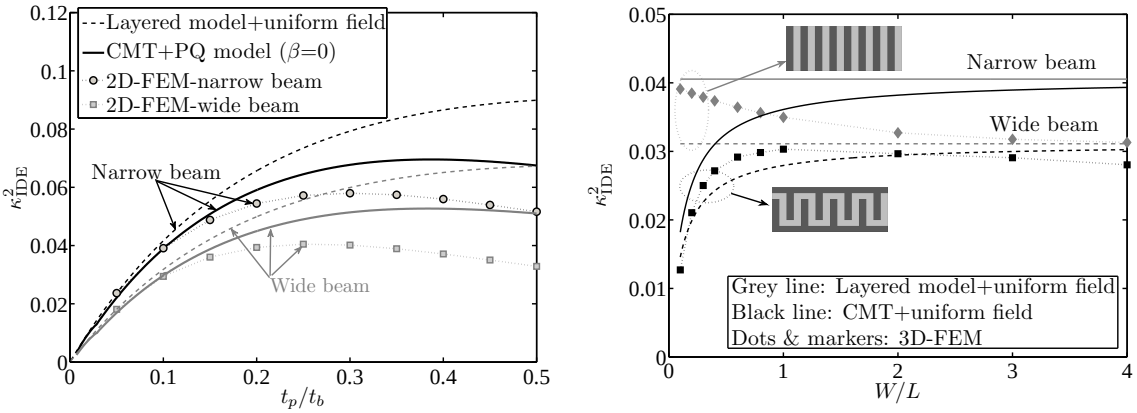

(a) With different piezoelectric layer thickness.

(b) Thin film piezoelectric $t_p/t_b = 0.1$ with different beam width and $g = 5\mu$m.

Figure 2.23: Electromechanical coupling factor of the IDE device

7.2 IDE beam

In Fig.2.23, the electromechanical coupling factor calculated by the layered model with the uniform field assumption is always larger than the FEM and CMT results. The reason is the overestimation of the uniform field model in Fig.2.15. For the thin piezoelectric layer i.e., $t_p \leq 0.1t_b = 2\mu$m, the overestimate is very small so the results of the two analytic (layered model and CMT with $\beta = 0$) and the FEM models are almost equal. For the thicker piezoelectric layer, even with an undesired compensation made by the capacitance overestimation Fig.2.12b, the electromechanical coupling factor calculated by the layered model is still higher than the FEM and the CMT results.

The electromechanical coupling factor of the symmetric and asymmetric IDE beams are shown in Fig.2.23b. The asymmetric IDE beam has smaller electromechanical coupling factor than the symmetric one. The reason is the parasitic capacitance around the end gaps of the asymmetric IDE configuration. For the symmetric IDE beam, the FEM results is bracketed between the narrow- and wide-beam results. The situation is more complex for the asymmetric IDE beam. For this configuration, if W is small, i.e., $W < L$, the FEM results increase significantly with the width W. The dramatic change comes from the change in the capacitance. The CMT model (darker solid and dashed line) is capable of capturing this feature. We note that the CMT result with wide-beam parameters is significantly closer to the FEM result than the CMT with narrow-beam parameters, also for rather small W/L.

7.3 Comparison between TBE and IDE

The ratio between the electromechanical coupling factor of the IDE beam Fig.2.23 and the TBE beam in Fig.2.22 is shown in Fig.2.24. Figure 2.24a shows the coupling ratio at different piezoelectric layer thickness. The area between the two curves with the narrow and wide beam parameters is the possible ratio values for the devices with a finite width. When the thickness ratio is less than 0.1, the electromechanical coupling factor ratio can be varied from 1 up to 2.5.

Figure 2.24b shows the coupling ratio when $t_p/t_b = 0.1$. We first consider the symmetric configuration. In this case, the layered model without end-gap effects, brackets the ratio from the FEM calculation. The wide-beam parameters give a

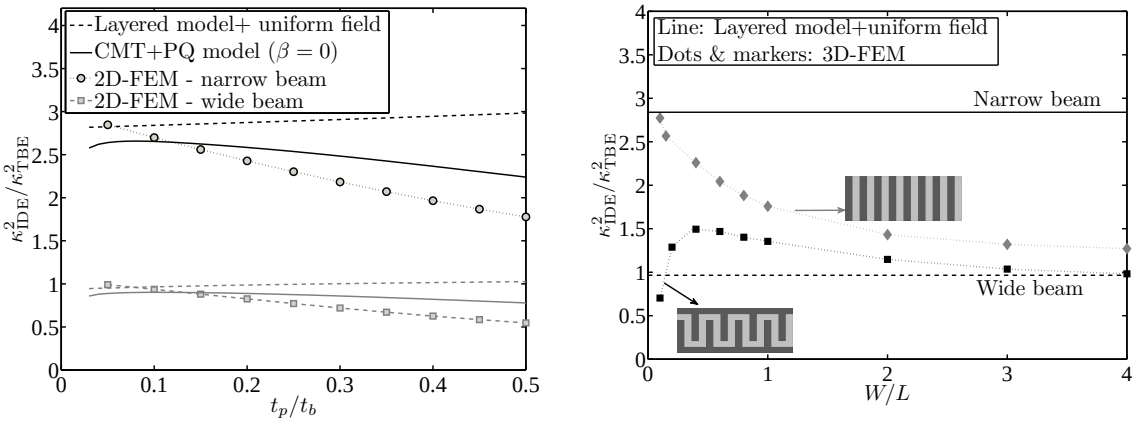

(a) With different piezoelectric layer thickness.

(b) Thin film piezoelectric $t_p/t_b = 0.1$ with different beam width and $g = 5\mu$m.

Figure 2.24: Electromechanical coupling factor ratio between the IDE and the TBE transducers

lower bound and the narrow-beam parameters give an upper bound. This is similar to the observation for the electromechanical coupling factor of the IDE beam in Fig.2.23b and the TBE beam in Fig.2.22b.

In Fig.2.24b, the lower limit of the coupling ratio is approximately one. Hence, the IDE beam always has higher electromechanical coupling factor than the TBE counterpart. The conclusion is confirmed by FEM results. The symmetric IDE beam always has larger electromechanical coupling factor than the TBE beam.

The same conclusion is arrived at for the asymmetric IDE beam with $W/L > 0.15$. The maximum ratio of electromechanical coupling factors is found for $W/L \approx 0.4$, i.e., $L = 1000\mu$m and $W = 400\mu$m, which gives a ratio of 1.5.

8 Characterization of the thin PZT film with IDE

In previous sections, we showed that the anisotropic piezoelectric material can be treated as an isotropic ones. In these analyses, we assumed that the permittivity is distributed homogeneously inside piezoelectric layer.

In this section, by using the assumption of a homogeneous distribution of the permittivity, a number of corrections are derived for the electric field and the capacitance. These new simplified models are helped to obtain the properties of the piezoelectric material with the IDE configuration e.g., PV, CV and the stress-field loops from experiment results. Details of device description and measurement set up are presented in the paper 3 [116].

In reality, the permittivity of the piezoelectric material is dependent on the applied electric field. In the TBE configuration, since the electric field is homogeneous, the permittivity will distribute homogeneously inside the piezoelectric layer. However, in the IDE configuration, the electric field inside the piezoelectric layer is spatial dependent. Therefore, the permittivity will distribute inhomogeneously. By using the finite element method, this inhomogeneous distribution is investigated. We observed that the inhomogeneous distribution could be treated as an effective homogeneous one.

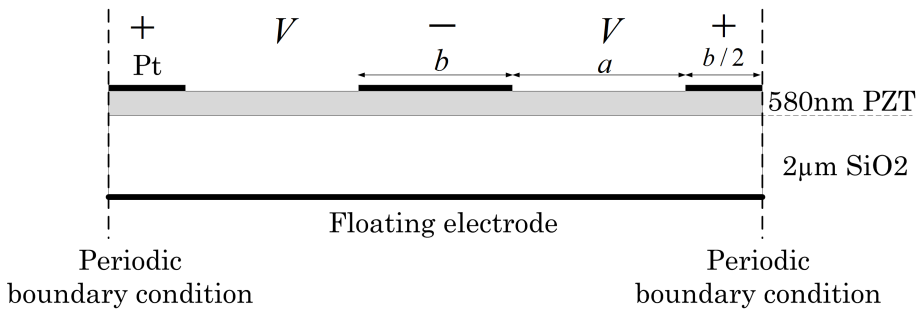

Figure 2.25: The geometry of the IDE transducer.

8.1 Analysis of the IDE devices with homogeneous dielectric distribution

Finite element simulation

A finite element model of the IDE structure presented in Fig.2.25 has been implemented. For the purpose of model comparisons, the piezoelectric material is treated as a homogeneous and isotropic dielectric material with a relative permittivity of 1000. The thickness of the piezoelectric layer is 580nm and the thickness of SiO_2 layer is 2μm. The relative permittivity of the SiO_2 layer is 4.2. On each sides, corresponding to the middle of the electrode finger, periodic boundary condition is applied. The condition means that the representative segment is repeated indefinitely, which is appropriate for the IDE configuration with many electrode pairs. Because the SiO_2 layer is on a conducting Si substrate, its bottom interface is treated as a floating electrode [81]. There is a potential difference V between two neighbouring electrode fingers. The Pt electrodes on the top have a thickness of 100nm and fixed width of $b = 6\mu$m.

The capacitance is the ratio between the total charge collected on the electrodes and the applied voltage. However, because of the singularities at the edges of the electrode fingers, numerical error occurs in the total charge integral. To avoid the error, the capacitance is calculated by integrating the energy density $\boldsymbol{D} \cdot \boldsymbol{E}/2$ (omitting the spontaneous polarization) over the whole volume $\mathcal{V}$ of the dielectric material as follows

$$C = \frac{\int \boldsymbol{D} \cdot \boldsymbol{E} \, \mathrm{d}\mathcal{V}}{V^2}. \tag{2.103}$$

Total capacitance model

In section 6.1, we have discussed that the anisotropic dielectric material can be treated as an isotropic dielectric one. To obtain the permittivity of the material, we will first measure capacitance as a function of the applied voltage. Then, the permittivity is calculated from a capacitance model which needs to be accurate. For instance, the capacitance per unit width between the two neighbouring electrode fingers with the homogeneous permittivity is

$$C_{\mathrm{IDE}} = \frac{\varepsilon_r \varepsilon_0}{2} \frac{K(k_{\mathrm{I}})}{K(k'_{\mathrm{I}})} \tag{2.104}$$

where ε_r is an equivalent relative permittivity of the ferroelectric material, ε_0 is the permittivity of vacuum, (2.104) follow the Igreja model [90], $k_{\mathrm{I}}, k'_{\mathrm{I}}, K(k_{\mathrm{I}})$ and $K(k'_{\mathrm{I}})$

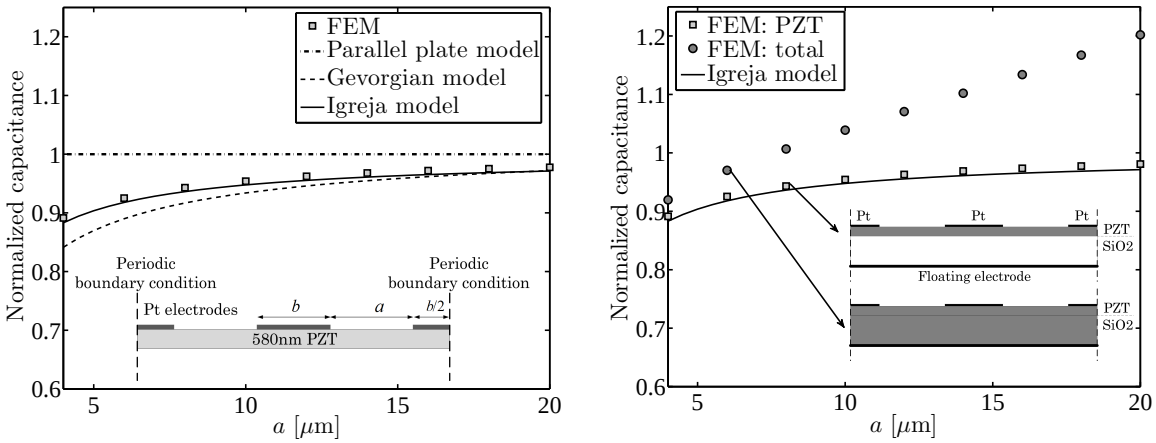

(a) With only a piezoelectric layer (b) The total capacitance.

Figure 2.26: Comparison between different capacitance models in case of only a piezoelectric layer (a) and the effect of the SiO_2 layer and the floating electrode on the total capacitance (b).

are given in section 6.1. Other models can be used for calculation such as Gevorian model [89] or the simple parallel plate model

$$C_{\mathrm{IDE}} = \varepsilon_r \varepsilon_0 \frac{t_p}{a} \tag{2.105}$$

Three analytical models: parallel plate model, Igreja model and Gevorian model, are used to calculate C_{IDE}. First, we analyze the simplest structure with the piezoelectric layer and IDE on top. The comparison helps to choose the most accurate analytical model for further investigation. The analytical results are validated by the FEM results. The comparison is shown in Fig.2.26a. For a consistency comparison, the FEM model is not taken the SiO_2 layer and the floating electrode into account as shown in the inset of the figure. The parallel plate model overestimates the capacitance. The Igreja model is more accurate than the Gevorgian model. This is the same observation as mentioned in [90]. In [90], the authors stated that transformation sequence could be the reason for the difference.

Next, we add the contribution of the SiO_2 layer and the floating electrode in the FEM model. In the FEM model, the ferroelectric layer capacitance and the total capacitance are calculated by different volume integrals (2.103). The results in Fig.2.26b show that the Igreja model can reproduce the capacitance of the piezoelectric layer. This capacitance is smaller than the total one. The differences are increasing for larger gaps a.

During a measurement, only the total capacitance is obtained. Therefore, to extract the properties of the ferroelectric material, we need to separate the C_{IDE} from the total value. We refers all contributions but C_{IDE} to the total capacitance as parasitic capacitances.

Figure 2.27 shows the electrostatic electric field inside the dielectric stack. In the ferroelectric layer, the electric field is very strong in the regions between the fingers. In the SiO_2 layer, the electric field is distributed in both regions between and beneath the electrode fingers.

Figure 2.28a illustrates equivalent circuit for the dielectric stack. The capacitance C_{IDE} is that of the ferroelectric material. The capacitance corresponds to the electric

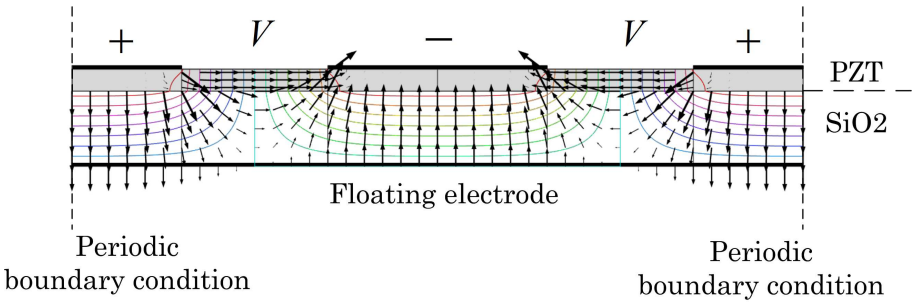

Figure 2.27: The electrostatic field inside the dielectric stack is presented. The contour show the equipotential lines. The length and direction of the arrows indicate the strength and direction of the electric field. The simulation is of the FEM model in Fig.2.25 with $a = 4\mu$m and $b = 6\mu$m.

field in the regions between the two neighbouring fingers. There are two kinds of capacitances in the SiO_2 layer. The first one, C_p', connects the IDE fingers together. It corresponds to the electric field lines that start and end on the IDE fingers as shown in Fig.2.27. The capacitances C_p' can be calculated using the partial capacitance method [90]. However, we observe that this capacitance is very small in comparison with $C_{\rm IDE}$ and can be neglected. The other one, C_p, connects the IDE fingers to the floating electrode. Because of the Pt top electrodes and the floating bottom electrode, the regions below the fingers can be regarded as two serial capacitors i.e., $C_{\rm PPE}$ and C_p. Since $C_{\rm PPE}$ and C_p have similar area but the piezoelectric material has much larger dielectric constant and smaller thickness than SiO_2, $C_{\rm PPE}$ can be neglected compared with C_p. However, the C_p capacitor has an area larger than the $C_{\rm IDE}$ by a factor b/t_p, and their small thickness compensates for the low dielectric constant of SiO_2, so this parasitic contribution can become comparable to $C_{\rm IDE}$ for large gaps. Therefore, C_p is the largest contribution to the parasitic capacitance within the interdigitating zone.

To estimate C_p, an artificial thin electrode at the interface of the ferroelectric and SiO_2 layers is introduced. The phenomenological model to obtain the electrode width is given in (2.106). We draw a line from the two end points of the Pt electrodes to the two points on the bottom of the SiO_2 layer at the center of the gaps. The two lines cut the PZT-SiO_2 interface at two points and define the effective electrode width as shown in Fig.2.28b. The idea emerges from the observation that the parasitic capacitance is gap and thickness dependent. Hence, the effective width of the equivalent electrode (2.106) is dependent on the Pt electrode width b, the active gap a and the thickness of the dielectric layers.

$$b_{\rm eff} = b + a\frac{t_p}{t_p + t_{\rm SiO_2}} \tag{2.106}$$

where $t_{\rm SiO_2}$ is the SiO_2 layer's thickness. Then, the capacitance of a trapezoid inside the SiO_2 layer Fig.2.28b is calculated. The capacitance formula [117] is

$$C_p = 2\varepsilon_{\rm SiO_2}\varepsilon_0\frac{K(k_{\rm C})}{K(k_{\rm C}')} \tag{2.107}$$

where the elliptic modulus is

$$k_{\rm C} = \sqrt{1 - k_{\rm C}'^2} = k_1 {\rm sn}\left(K(k_1)\frac{b_{\rm eff}}{a+b}, k_1\right). \tag{2.108}$$

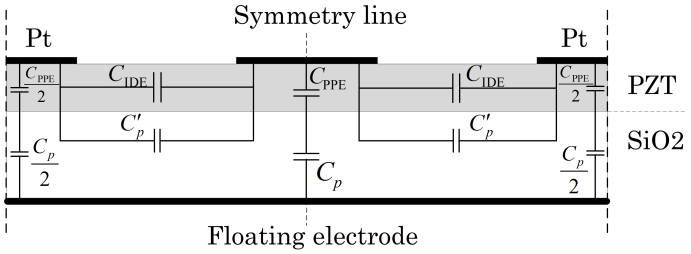

(a) The equivalent circuit.

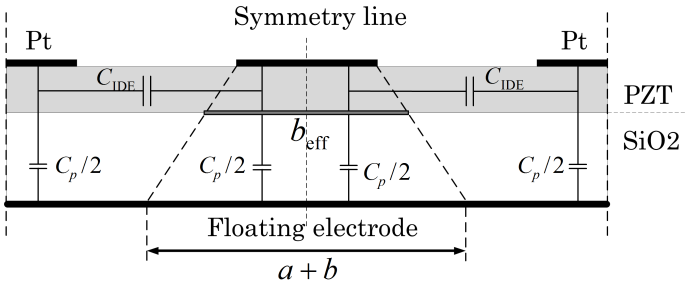

(b) The simplified version.

Figure 2.28: The equivalent circuit (a) and its simplified version (b) of the IDE representative segments. For clarity, in (b), we only show the equivalent electrode for one finger.

The modulus k_1 is found from

$$\frac{K(k_1')}{K(k_1)} = \frac{2t_{\mathrm{SiO_2}}}{a+b}. \tag{2.109}$$

Finally, if N is the number of the gaps, the total capacitance per unit width is

$$C = N\left(C_{\mathrm{IDE}} + \frac{C_p}{4}\right). \tag{2.110}$$

In (2.110), we assumed that the number of the gaps is large enough so that the contribution of the exterior electrode capacitances as mentioned in [90] can be assumed to be equal to that of the inner electrodes.

The results of the total capacitance is shown in Fig.2.29a and we see that the FEM and the analytical results are in a good agreement. Hence, capacitances of the piezoelectric and the SiO_2 layer can be distinguished. In Fig.2.29a, a few variations of the effective electrode b_{eff} are also presented. The smallest width $b_{\mathrm{eff}} = b$, which is independent of the gap and thickness, underestimates the FEM results. And the largest $b_{\mathrm{eff}} = a + b$, which is independent of the thickness, overestimates the capacitance.

The accuracy of the total capacitance model (2.110) is validated for the piezoelectric layer thickness up to 4μm. This thickness limit is common for thin piezoelectric film deposited with the sol-gel process. The thickness of the SiO_2 is fixed at 2μm. The ratio of the analytical (2.110) to the FEM results is presented in Fig.2.29b. The maximum difference between the two models in the whole range of the gap and the film thickness is found to be less than 4%.

We note that in measurement, there are additional parasitic capacitances of the SiO_2 layer beneath the contact pads and the IDE bus-bars. For our samples, these capacitance have been characterized in [118] and should be distinguished from (2.107).

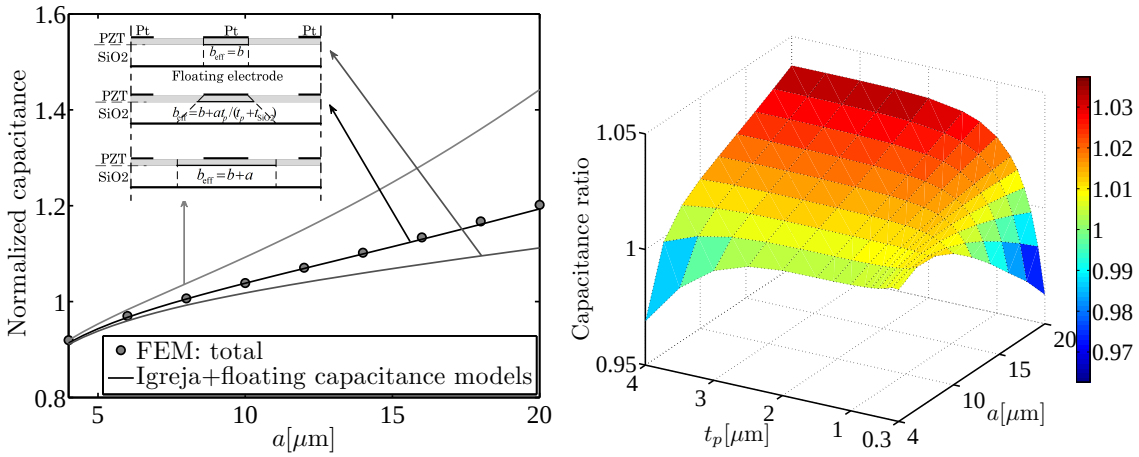

(a) The normalized value. (b) The ratio value.

Figure 2.29: The comparison between the analytic (2.110) and FEM model of the total capacitance. (a) Both are normalized with (2.105), (b) Capacitance ratio of (2.110) with the effective electrode width (2.106) to the FEM results

Effective electric field model

Since the ferroelectric material coefficients are dependent on the electric field strength, it is nessesary to know how much potential difference should be applied across the electrodes. For IDE devices, although not so accurate, to estimate the electric field by the voltage over gap ratio is often used in literature due to its conveniency. Recently, some efforts have been made to improve the accuracy of the IDE's electric field model while keeping the formula in a simple form. For instance, the Gevorgian capacitance model is simplified [81, 118] to

$$C_{\text{IDE}} = \varepsilon_r \varepsilon_0 \frac{t_p}{a + \Delta a_1} \tag{2.111}$$

where Δa_1 is only thickness dependent

$$\Delta a_1 = \frac{4\ln(2\sqrt{2})}{\pi} t_p. \tag{2.112}$$

Then, by comparing equations (2.111) and (2.105), we see that the gap a is extended to an effective value $(a + \Delta a_1)$. Therefore, the electric field is analogous to

$$E = \frac{V}{a + \Delta a_1}. \tag{2.113}$$

The correction value Δa_1 enable a simple but more accurate estimation of the electric field than the traditional uniform field model [81]. However, as observed in Fig.2.26a, the Igreja model is more accurate than the Gevorgian model. Therefore, it is worth figuring out if the Igreja model can be simplified with a similar approximation.
In thin film approximation, $(a + b)/2t_p$ is much larger than one, using (2.83), the elliptic modulus is expressed as

$$k = 1 - \frac{8}{q_2} \tag{2.114}$$

where $q_2 = e^{\frac{\pi(a+b)}{2t_p}}$ is given in (2.85). This value approaches infinity if the pitch to thickness ratio is very large. In our study, q_2 is at least $\exp(10\pi/(2 \times 0.58)) \approx$

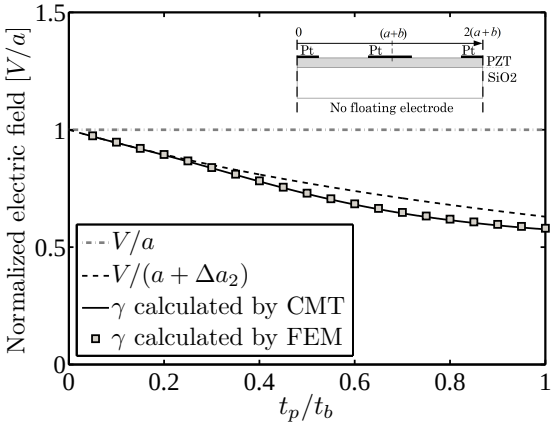

Figure 2.30: Different normalized models of the electric field at the center of the gap. The structure is shown in the inset, the floating electrode is not taken into account.

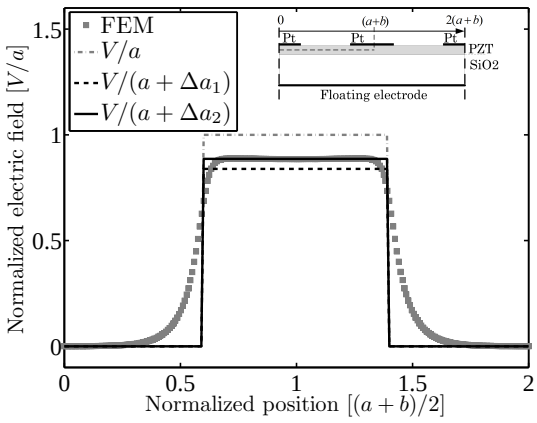

Figure 2.31: Electric field in longitudinal direction. The inset with the cut line of the electric field with $a = 4\mu$m, $b = 6\mu$m

5.77×10^{11} for the smallest gap so k is asymptomatically close to 1 for all gaps. When $k \approx 1$, using two simplifications $\mathrm{sn}(z,k) \approx \tanh z$ and $K(k) = \ln(\frac{4}{\sqrt{1-k^2}})$ [119], then

$$\mathrm{sn}(K(k)\frac{b}{a+b}, k) \approx \tanh(\frac{b}{a+b}K(k)) = 1 - 2\left(\frac{\sqrt{1-k^2}}{4}\right)^{\frac{2b}{a+b}} \tag{2.115}$$

Substituting (2.115) and (2.114) into (2.77), we get

$$k_\mathrm{I} \approx \frac{1}{\sqrt{1 + q_2^{\frac{a}{a+b}}/4}}. \tag{2.116}$$

As q_2 is going to infinity, the elliptic modulus k_I approximates zero so k'_I approximates one. Then, $1 + k'_\mathrm{I} \approx 2$ and $1 - k'_\mathrm{I} = 1 - \sqrt{1 - k_\mathrm{I}^2} \approx k_\mathrm{I}^2/2$, the elliptic integral ratio using (2.82) is simplified to

$$\frac{K(k'_\mathrm{I})}{K(k_\mathrm{I})} \approx \frac{2}{\pi}\ln\frac{4}{k_\mathrm{I}} \approx \frac{a}{2t_p} + \frac{2\ln 2}{\pi} \tag{2.117}$$

where the second approximation is found by replacing (2.116) into the first approximation. Finally, replacing (2.117) into (2.104), ones obtains the capacitance in the form

$$C_\mathrm{IDE} = \varepsilon_r\varepsilon_0\frac{Wt_p}{a + \Delta a_2} \tag{2.118}$$

where Δa_2 is

$$\Delta a_2 = \frac{4\ln(2)}{\pi}t_p = \frac{2}{3}\Delta a_1. \tag{2.119}$$

We observe that the new correction value is around 67% of the previous correction value. The simplification gives a numerical explanation why the Igreja model gives higher capacitance than the Gevorgian model. Moreover, when a becomes large, the correction values Δa_1 and Δa_2 are negligible, the two models are asymptotical as shown in Fig.2.26a.

The new electric field formula based on the new correction term is

$$E = \frac{V}{a + \Delta a_2} = \frac{V}{a}\frac{a}{a + \Delta a_2} \tag{2.120}$$

The fraction $a/(a + \Delta a_2)$ is analogous to the γ value in the PQ model of the electric field (2.95) with thin film approximation. Figure 2.30 compare the accuracy of different electric field model at the center of the gap. In this figure, the structural dimensions and permittivity are $a = 30\mu$m, $T = a + b = 40\mu$m $t_p = 20\mu$m, $\varepsilon_r = 1000$ and $\varepsilon_{SiO_2} = 4.2$. The floating electrode is not taken into account. The figure shows that the ratio $(a/a + \Delta a_2)$ is a good approximation of γ especially if $t_p < 0.3t_b$ or $t_p < 0.15T$.

In our samples, the smallest pitch is $T = 10\mu$m, the piezoelectric thickness is $t_p = 580$nm. Hence t_p is always less than $0.15T$. When the floating electrode condition is taken into account as shown in Fig.2.25, the electric field in the longitudinal direction is presented in Fig.2.31. Three different electric field models are verified by the finite element results. The figure showed that the simplification model with the correction quantity Δa_2 is best match with the FEM results.

8.2 Results

CV and PV curves

First, the simplest model of uniform field V/a and parallel plate capacitance (2.105) is used to characterize the CV and PV curves for different IDE samples. The results are shown in the figures Fig.2.32a and Fig.2.32b. We subtracted the parasitic capacitance and the parasitic charges of the contact pads and bus-bar regions from the measured results for CV and PV loops respectively. These parasitic capacitances were characterized in [118].

As previously observed in Fig.2.26b, FE simulation shows that the total normalized capacitance increases with increasing gap due to the parasitic capacitance of the SiO_2 layer beneath the IDE fingers. This parasitic contribution was not subtracted from the measured result, therefore (2.105) overestimates the relative permittivity, especially at large gap. This overestimation leads to the spread of the data in Fig.2.32a and, because of the inaccurate estimation of the electric field value, to the gap dependent coercive field seen in Fig.2.32b.

A state-of-art characterization method for the CV and PV loops is presented in [81]. The simplified Gevorgian models (2.111) and (2.113) are used to calculate the capacitance and the electric field. The parasitic capacitance beneath the IDE fingers is subtracted by a fitted model. Using these models, the raw data in Fig.2.32a and Fig.2.32b are re-analyzed. The results are shown in Fig.2.32c and Fig.2.32d respectively for the CV and PV loops. These figures are corresponding to the Fig.15c and Fig.15d in [81]. The coercive fields for different gaps are almost equal as shown in the PV loops Fig.2.32d. The coincidence of the CV curves Fig.2.32c are improved in comparison with the Fig.2.32a.

Then, we re-analysed the raw data in Fig.2.32a and Fig.2.32b using our new models. First, C_{IDE} is extracted from the total capacitance (2.110) by using the parasitic capacitance model C_p (2.107). Then, the permittivity is recalculated using simplified Igreja capacitance model (2.118). The electric field is rescaled with the factor $a/(a + \Delta a_2)$. The results from the analysis are shown in Fig.2.32e. The coincidence of the CV curves for different gaps is much improved. For instance, if

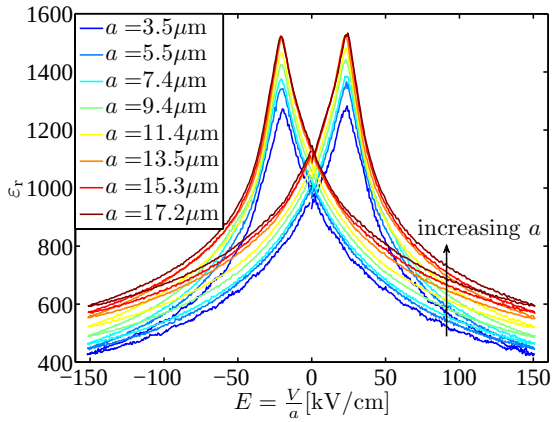

(a) The CV loops

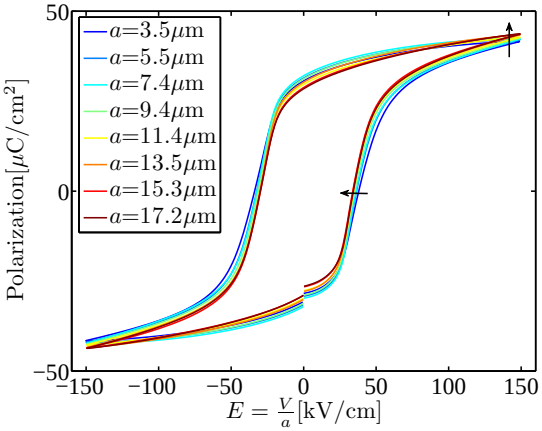

(b) The PV loops

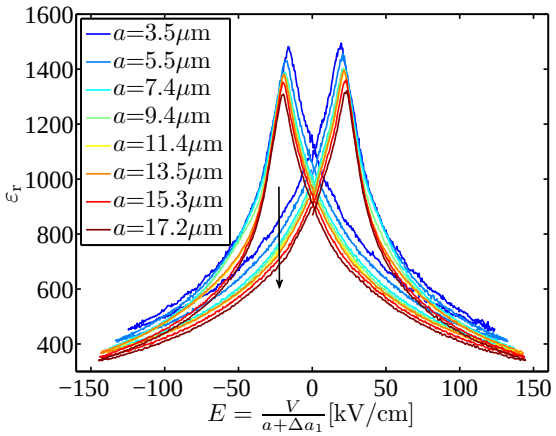

(c) The CV loops

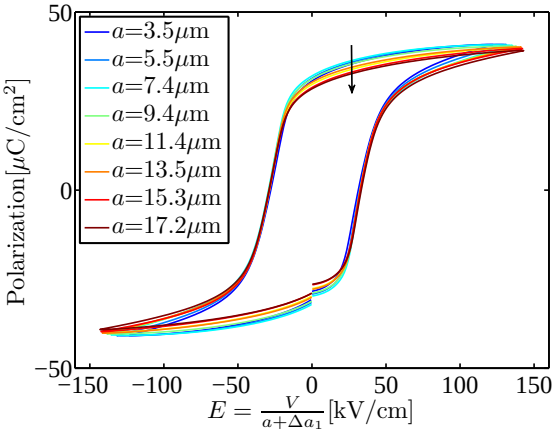

(d) The PV loops

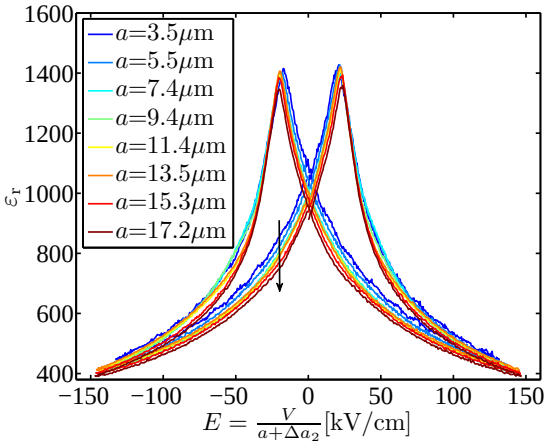

(e) The CV loops

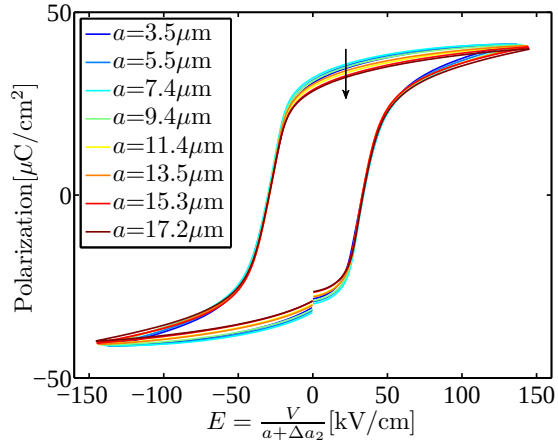

(f) The PV loops

Figure 2.32: Characteristic curves of the PZT film with the IDE on tops. The raw data is measured and reported in [118]. The arrow direction indicates the increasing gap. In (a) and (b), the curves are with the parallel plate capacitance model (2.105) and $E = V/a$. The parasitic capacitance C_p is not subtracted yet. In (c) and (d), the permittivity are with the simplified Gevorgian model (2.111), the electric field is rescaled to $E = V/(a + \Delta a_1)$, the parasitic capacitance is subtracted by using the fitting method. The Figure (c) and (d) correspond to Fig.15c and Fig.15d in [81]. In (e) and (f), the permittivity are with the simplified Igreja model (2.118), the electric field is rescaled to $E = V/(a + \Delta a_2)$, the parasitic capacitance model C_p (2.107) is used to subtract parasitic contributions.

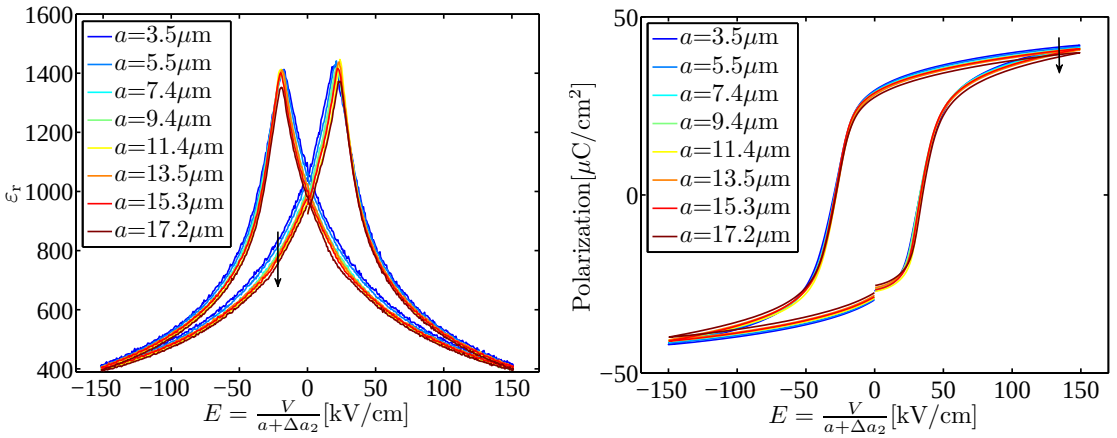

(a) CV loops.

(b) The PV loops

Figure 2.33: Characteristic curves of the PZT film with the IDE on tops. The curves are with the simplified Igreja model (2.118) and $E = V/(a + \Delta a_2)$. The parasitic capacitance C_p is subtracted. The arrow direction indicates the increasing gap.

we calculate the relative spread of the permittivity at the peak of the curve $\varepsilon_r^{\text{peak}}$ around the average value

$$\%\,\text{spread} = 100\frac{\max(\varepsilon_r^{\text{peak}}) - \min(\varepsilon_r^{\text{peak}})}{\max(\varepsilon_r^{\text{peak}}) + \min(\varepsilon_r^{\text{peak}})}. \tag{2.121}$$

The relative spread from around 9% or 6% between the largest and smallest permittivity respectively in Fig.2.32a and Fig.2.32c is reduced to about 2% in Fig.2.32e. For the PV loops, the gap dependent coercive field as seen in Fig.2.32b seems to disappear in Fig.2.32f.

The improvement has motivated for a new measurement, where the new maximum voltage is calculated using the simplified Igreja electric field model (2.113) such as the maximum field is 150kV/cm for all gaps. The results in Fig.2.33 shows the very good coincident for both CV and PV curves. In the CV curves, the relative spread of $\varepsilon_r^{\text{peak}}$ is around 2%. Especially, the spread is less than 0.4% for all the gaps smaller than 15.3μm.

Piezoelectric response in converse mode

In the converse mode, we configure the IDE samples as cantilever actuators. The beam is actuated when an electric potential is applied. First, we assume that these actuators have the same curvature in the transduction regions both under and between the IDE. The deflection formula of the beam is then

$$\delta(x_2) = \rho_{33}\frac{x_1(2x_2 - x_1)}{2} \tag{2.122}$$

where ρ_{33} is the bending curvature as given in (2.44), $\delta(x)$ is the deflection of the cantilever at position x, x_2 is the laser's reflection position and $x_1 = N(a + b)$, these positions are shown in the Fig.3 in paper 3 [116]. Since the substrate is much thicker than the ferroelectric film, the curvature can be simplified to

$$\rho_{33} = \frac{6t_p}{Y_{\text{Si}}t_{\text{Si}}^2}e_{33,\text{if}}Ec_f \tag{2.123}$$

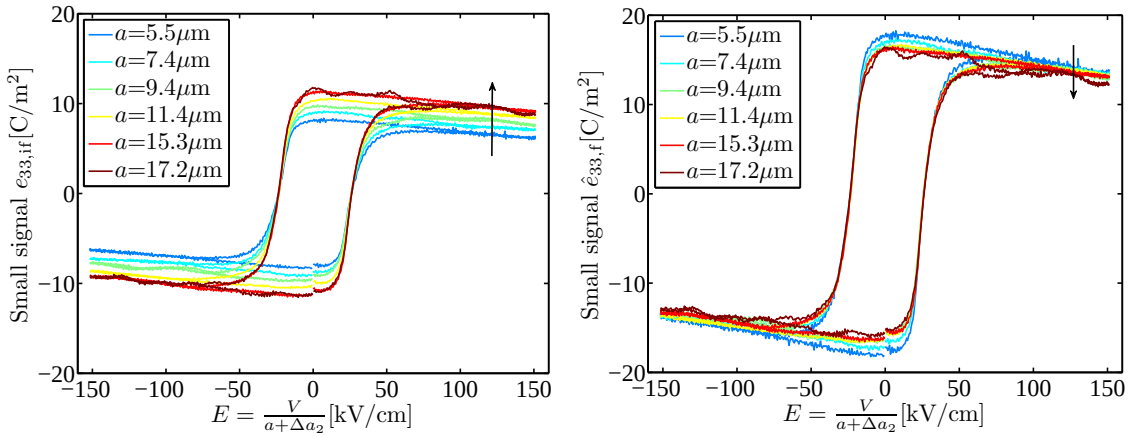

(a) The engineering value (2.124). (b) The effective value (2.129).

Figure 2.34: The small signal coupling constant.

where Y_{Si} is the Young modulus of the Si substrate, $e_{33,\mathrm{if}}$ is the engineering piezoelectric coupling constant [57] and c_f is the transducer coverage factor which is the ratio of the IDE width to the total cantilever width. The simplified curvature is similar to the Stoney formula [120]. Replacing the effective electric field formula (2.120) into (2.123), the engineering coupling constant is analogous to equation (16) in [57] but with the new model of the effective electric field

$$e_{33,\mathrm{if}} = \frac{1}{c_f}\frac{\delta(x_2)}{x_1(2x_2-x_1)}\frac{Y_{\mathrm{Si}}t_{\mathrm{Si}}^2}{3t_p}\frac{a+\Delta a_2}{V}. \tag{2.124}$$

The results of the engineering $e_{33,\mathrm{if}}$ is shown in Fig.2.34a, showing a gap-dependent value for different samples. The reason for this spread is the average of the bending curvature which originates from the same curvature ρ_{33} distribution assumption in the ferroelectric film both at active and passive regions (2.122). By this assumption, the curvature in the passive regions is overestimated while the curvature in the active regions is underestimated. Actually, the electric field is very small in the passive regions, the curvature distribution can be

$$\frac{d^2\delta}{dx^2} = \begin{cases} \hat{\rho}_{33} & \text{active regions,} \\ 0 & \text{passive regions,} \end{cases} \tag{2.125}$$

where the active region curvature is

$$\hat{\rho}_{33} = \frac{6t_p}{Y_{\mathrm{Si}}t_{\mathrm{Si}}^2}\hat{e}_{33,\mathrm{f}}Ec_f, \tag{2.126}$$

with $\hat{e}_{33,\mathrm{f}}$ is the effective coupling constant in the active regions.

Then, the deflection is [57, 111]

$$\delta(x_2) = \hat{\rho}_{33}\frac{(Na)^2}{2}\left(1+\left(1-\frac{1}{N}\right)\frac{b}{a}\right) + N\hat{\rho}_{33}a(x_2-x_1). \tag{2.127}$$

If the number of active regions N is large enough, (2.127) is simplified to

$$\delta(x_2) = \hat{\rho}_{33}\frac{x_1^2}{2}\frac{a}{a+b} + N\hat{\rho}_{33}a(x_2-x_1). \tag{2.128}$$

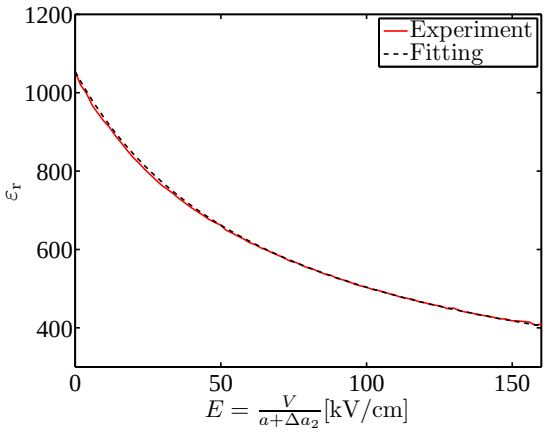

Figure 2.35: The relation between the permittivity and the electric field.

From (2.128), (2.126), (2.120) and $x_1 = N(a+b)$ the effective coupling constant is

$$\hat{e}_{33,\mathrm{f}} = \frac{1}{c_f}\frac{\delta(x_2)}{x_1(2x_2-x_1)}\frac{Y_{\mathrm{Si}}t_{\mathrm{Si}}^2}{3t_p}\frac{a+\Delta a_2}{V}\frac{a+b}{a}. \tag{2.129}$$

From (2.129) and (2.124), we get

$$\hat{e}_{33,\mathrm{f}} = e_{33,\mathrm{if}}\frac{a+b}{a}. \tag{2.130}$$

Equation (2.130) can provide an analytical expression for a phenomenological correction factor introduced in equation (18) in [57]. This correction factor, the ratio of the approximate electric field (V/a) and nominal field, is a constant in [57]. However, by comparing that result to (2.130), we see that the factor is $(a+\Delta a_2)/a$ which is a gap and thickness-dependent.

The results of the $\hat{e}_{33,\mathrm{f}}$ coefficient (2.129) are shown in Fig.2.34b. At the saturation, the relative spread, calculated by using (2.121) for the $\hat{e}_{33,\mathrm{f}}$ coefficient at the maximum electric field, of more than 20% in Fig.2.34a is reduced to less than 7% in Fig.2.34b.

8.3 Inhomogeneous distribution of dielectric

In section 8.1, we assumed that the permittivity was homogeneously distributed inside the ferroelectric material. This assumption allows the formulation of some material properties such as the relative permittivity, polarization and the coupling constant. These models are verified by both FEM and measurement results at different gaps and electric field strength (2.120). However, in the IDE device, the electric field is inhomogeneous in the piezoelectric film. Hence, the dielectric constant distribution is also inhomogeneous because the relative permittivity is a field dependent parameter. To observe the inhomogeneity, the FEM model of section.8.1 is modified. The field dependent permittivity is taken into account. An iterative process in the finite element simulation program (Comsol) updates the inhomogeneous dielectric distribution with respect to the inhomogeneous electric field distribution until convergence.

The relationship between the relative permittivity and the electric field strength is shown in Fig.2.35. The experiment data is taken from the lower branch of the CV curve of the sample with $a = 3.5\mu$m. The gap $a = 3.5\mu$m is chosen because the

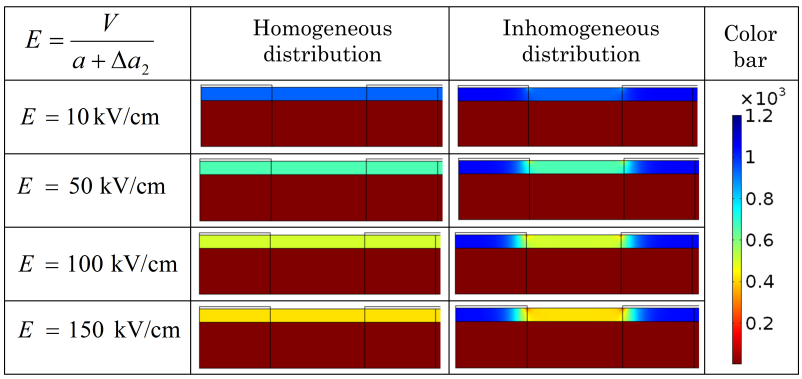

Figure 2.36: The distribution of the dielectric inside the ferroelectric material for $a = 4\mu$m. The color bar indicates the relative permittivity value.

smaller gap can provide the most uniform electric field (as will be clear from Fig.2.37). The field uniformity leads to a homogeneous permittivity distribution. We will see later that for large gaps the electric field is no longer uniform. A phenomenological model is fitted with the experimental data as follows:

$$\varepsilon_r = \frac{A}{E + E_0} + B \tag{2.131}$$

where $A = 6.28 \times 10^9 (V/\text{m})$, $B = 129.6$ and $E_0 = 6.8 \times 10^6 (V/\text{m})$. The permittivity-field relation (2.131) is then used as an input for further FEM simulation.

Figure 2.36 presents the dielectric constant distribution inside the piezoelectric material. The permittivity is a field- and spatial-dependent parameter. The bottom layer is the SiO_2 layer with a homogeneous relative permittivity of 4.2.

The relative permittivity along the cut line as in the inset of Fig.2.31 is shown in Fig.2.37a and in Fig.2.37c respectively for $a = 4\,\mu$m and $a = 20\,\mu$m. The corresponding electric field distributions are shown in Fig.2.37b and in Fig.2.37d. Beneath the electrode, the relative permittivity is larger than in the case of the homogeneous distribution. This is due to the small electric field as shown in Fig.2.37b and Fig.2.37d. Around the boundary between the active and passive regions, there is a transition region where the permittivity is decreasing because of the increasing electric field. In the active regions, for the smaller gaps, the relative permittivity and the electric field are almost the same as for the homogeneous distribution. However, for larger gaps, the relative permittivity and the electric field are very different from the homogeneous distribution. The difference disappears if the floating electrode condition is removed in the FEM model as shown in Fig.2.38. This difference between the two is caused by the fact that the electric field distribution is more inhomogeneous for large gaps than for small gaps, even in the homogeneous dielectric constant case, as can be seen in Figures 2.37b and 2.37d. By construction, the FE model introduces a positive feedback between the local dielectric constant and electric field strength because of equation (2.131) : In regions with a large electric field, the dielectric constant is diminished in the next iteration, which occasions a larger local voltage drop (similarly to two capacitors in series, where the smaller one experiences the larger voltage drop) and, hence, an enlarged electric field, and so forth. Because of this, a greater proportion of the bias between the electrodes is dropping near the electrodes edge. Thus, less is dropping in the middle of the gap, which experiences a lower electric field strength, yielding an increased dielectric constant in this region because of equation (2.131). If the floating electrode is absent,

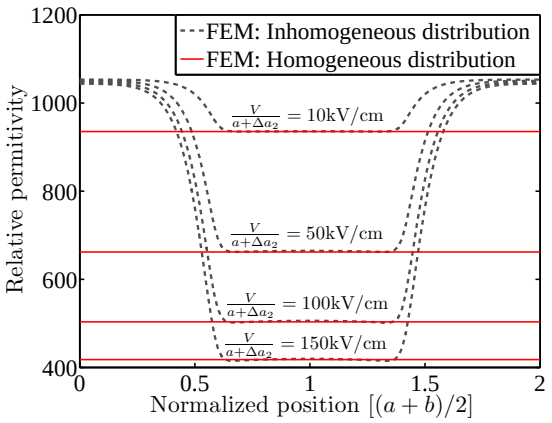

(a) The relative permittivity.

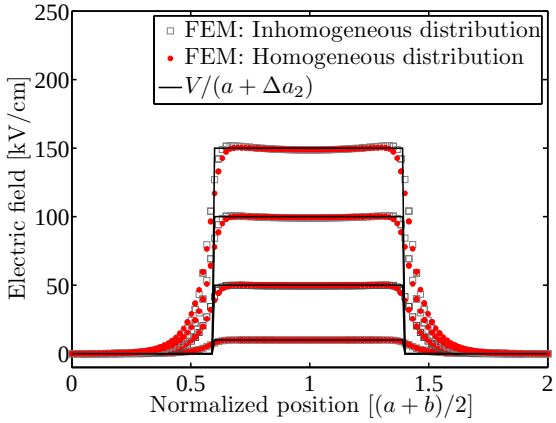

(b) The electric field.

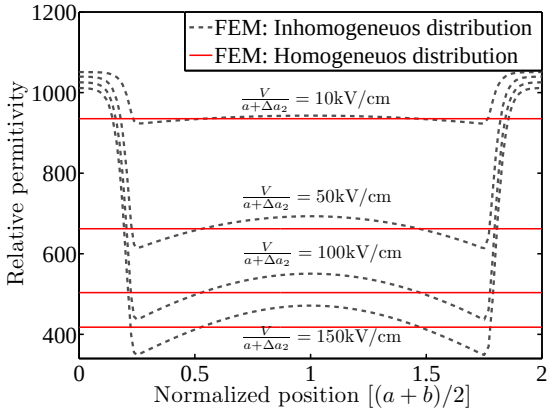

(c) The relative permittivity.

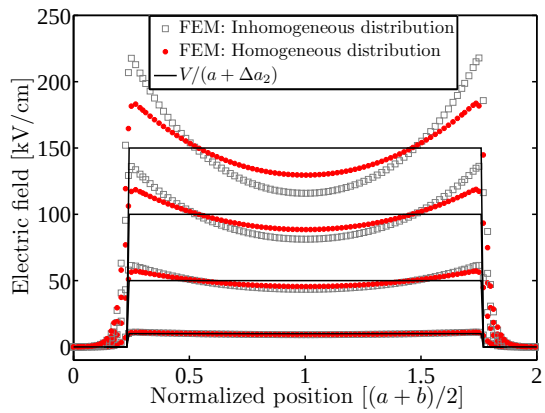

(d) The electric field.

Figure 2.37: The relative permittivity and electric field in Fig.2.36 at the material's cut-line as in Fig.2.31 for two different gaps: $a = 4\,\mu$m (a),(b) and $a = 20\,\mu$m (c),(d).

the electric field is very uniform within the PZT layer for all gaps (see Figure 2.38 and [81]) and therefore this effect is not observed.

The capacitance value in both cases of the permittivity distributions for the 580 nm-thick ferroelectric layer thickness is shown in Fig.2.39a. Despite the different in the permittivity distribution, the capacitances are almost equal. If we further vary the ferroelectric film's thickness as shown in Fig.2.39b, the capacitances are also mostly equal. The reason can be the reciprocal relationship between the electric field and the permittivity. These quantities compensate each other since they appear as a product in the formula for the capacitance. The same capacitance means that the inhomogeneous distribution can be treated as the homogeneous distribution by an equivalent permittivity given in (2.131) where electric field E is defined in (2.120).

The results of the electric field Fig.2.37d reveal that the electric field at the mid-gap and center position of the piezoelectric layers due to the effect of the floating electrode does not equal the value calculated by (2.120). It is smaller especially when the gap is large for both cases of the permittivity distributions. This suggests another correction for the electric field. Because an inhomogeneous distribution of the permittivity can be treated as a homogeneous distribution, the electric field correction in the case of homogeneous permittivity distribution is investigated.

Different finite element simulations with the homogeneous permittivity distribution are required. We vary the gaps and the applied voltage on the electrodes. For

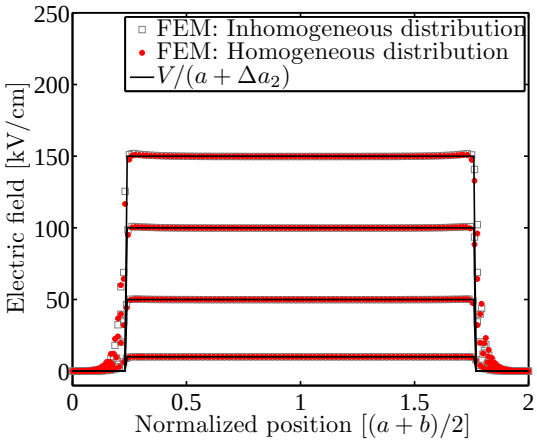

Figure 2.38: The electric field with $a = 20\mu$m in both cases of homogeneous and inhomogeneous dielectric distribution when the floating electrode is not taken into account.

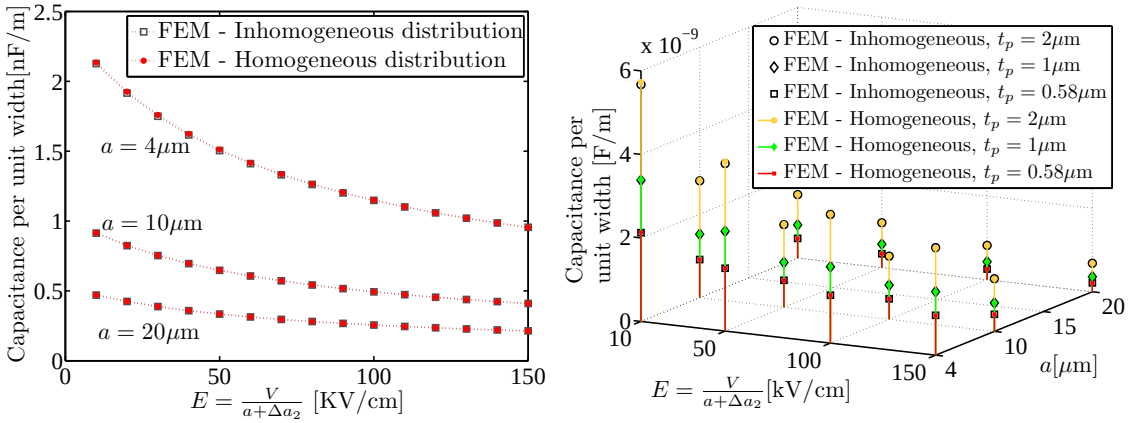

(a) The piezoelectric thickness is $t_p = 580$nm. (b) The piezoelectric thickness is varied.

Figure 2.39: The capacitance in both cases of homogeneous and inhomogeneous distribution.

each simulation, one electric field correction factor ϑ is found by dividing the electric field value at the center and mid-gap of the piezoelectric material by (2.120). A map of all the correction factors with respect to different applied voltages and gaps is found. These data are shown as the black dots in Fig.2.40. By fitting all the data point with a second order polynomial, we can interpolate the correction factor for all variations of gaps and voltages within the investigated range. The second order polynomial expressing the correction factor is

$$\vartheta = \vartheta_{00} + \vartheta_{10}\frac{V}{a+\Delta a_2} + \vartheta_{20}\left(\frac{V}{a+\Delta a_2}\right)^2 + \vartheta_{01}a + \vartheta_{02}a^2 + \vartheta_{11}\frac{Va}{a+\Delta a_2} \qquad (2.132)$$

where $\vartheta_{00} = 0.9956$, $\vartheta_{10} = 4.904\times10^{-10}$ m/V, $\vartheta_{20} = 4.481\times10^{-17}$ m^2/V^2, $\vartheta_{01} = 1261$ 1/m, $\vartheta_{02} = -2.114\times10^{8}$ 1/m^2, $\vartheta_{11} = -2.988\times10^{-4}$ 1/V.

The fitted surface is also presented in the Fig.2.40. For the small values of the gaps and the applied potential, the correction factor is very close to 1. The electric field is well approximated by (2.120). For larger gap or higher applied electric potential, the correction factor is decrease and becomes important.

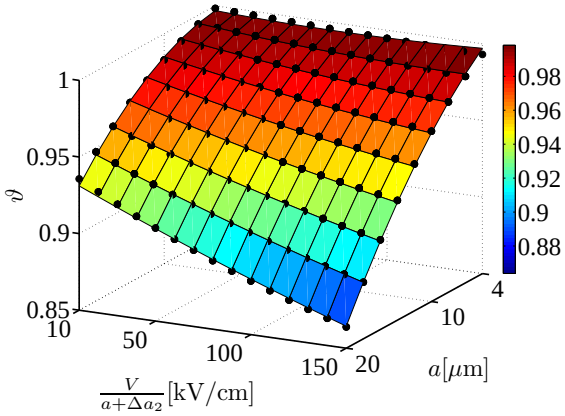

Figure 2.40: The correction factor ϑ for the electric field. The second order polynomial (2.132) (faces) is fitted with the FEM results (black dots).

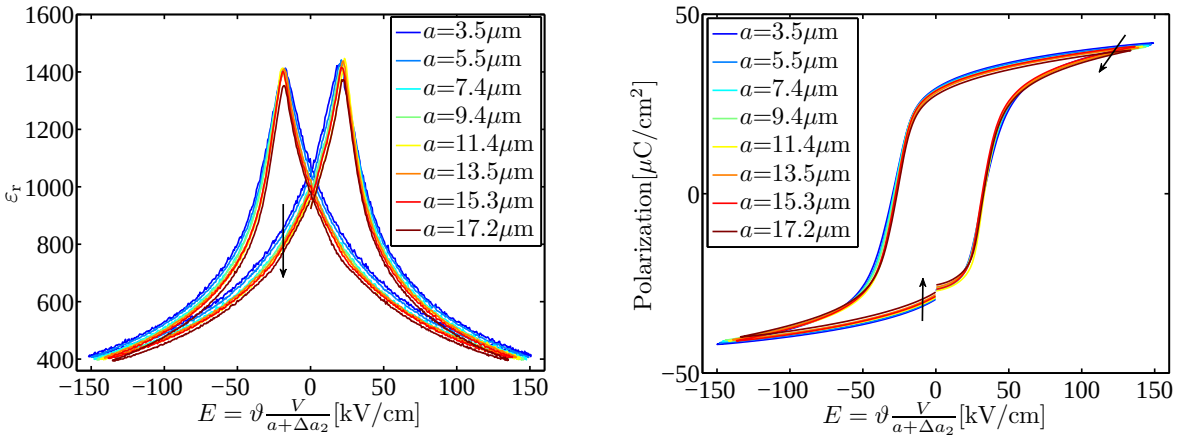

(a) The CV loops.

(b) The PV loops.

Figure 2.41: The CV and PV loops of the PZT film with IDE on tops.

The CV and PV curves in Fig.2.33 are re-plotted respectively in Fig.2.41a and Fig.2.41b with a rescaled electric field axes. In the CV curves, around the coercive field (peak points), the permittivity are almost equal for different samples. However, at the lower or higher fields, the permittivity appear gap dependent.

A possible explanation for the lower dielectric constant for large gaps is as follows. The electric field lines can be split into two parts: the longest part with the length a and two curved lines with the length of $\Delta a_2/2$ near the electrode fingers [81]. In the longest part, the electric field is directed along the x (horizontal) direction (*i .e.* $E_z = 0$). Hence, we would expect it responds more with $\varepsilon_{\parallel}$ than with $\varepsilon_{\perp}$, where $\varepsilon_{\parallel}$ is the dielectric constant along the polarization direction and $\varepsilon_{\perp}$ is the dielectric constant orthogonal to the polarization direction. In the curved electric field regions, we expect that the misalignment between the polarization vector and the field is larger on average, because the domain pattern must accommodate a large field gradient. Hence, in this region, we expect more contribution from $\varepsilon_{\perp}$. In PZT, $\varepsilon_{\perp} > \varepsilon_{\parallel}$, and if the typical spatial extent of the curved electric field region is Δa_2 (the same for all gaps), then the size of the contribution of $\varepsilon_{\perp}$ to the total capacitance will be proportional to $\Delta a_2/a$, and so it will be bigger for small gaps. Therefore, the larger dielectric constant is apparent for small gaps.

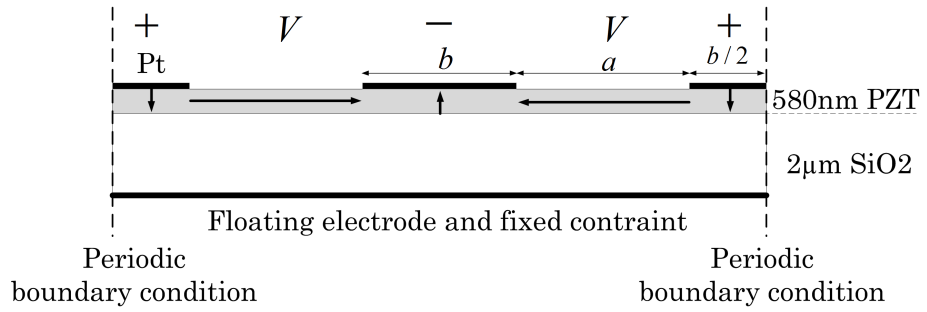

Figure 2.42: The FEM model of the IDE device with piezoelectric coupling coefficient taken into account. The arrow show the direction of the polar axis.

Another observation is seen by introducing the piezoelectric coupling into the FEM model of section 8.1. The model is shown in Fig.2.42. The direction of the polar axis is chosen to follow the electric field direction in a simplified way as shown in Fig.2.42. Since the films is deposited on a wafer of full thickness, the substrate's stiffness prevent the film from expansion. Hence, we set the fixed constraint boundary condition at the interface of the SiO_2-Si. The model requires a full tensor description of the piezoelectric material which is not all available for our samples. We use another piezoelectric tensor for a similar thin film [51] as given in Table 2.1. However, both dielectric constant ε_{33}^T and ε_{11}^T are kept equal 1000. To understand the effect of the coupling, two simulation were performed: one simulation with all piezoelectric coupling coefficients artificially set to zero and the other one with the piezoelectric coupling coefficients set to the values in [51]. By using a literature data, we only expect to obtain a qualitative agreement.

The capacitance of the piezoelectric layer in both simulation cases are shown in Fig.2.43. To eliminate the effect of the gap distance in the capacitance formula, the capacitance of each curve is multiplied with the effective gap $(a + \Delta a_2)$. The capacitance $C_{\text{IDE}}^{\text{PPL}}$ is calculated by the parallel plate model (2.105), while $C_{\text{IDE}}^{\text{CMT}}$ is calculated by the conformal mapping technique with the simplified Igreja model (2.118). We have a factor 2 to account for the two-gap region of the FEM geometry. The two capacitances $C_{\text{IDE}}^{\text{FEM}}$ are the output of the finite element simulation in the two cases of zero and non-zero coupling. Similar to the results observed in Fig.2.26a, the parallel plate model $C_{\text{IDE}}^{\text{PPL}}$ overestimates the capacitance. The results calculated by simplified Igreja model $C_{\text{IDE}}^{\text{CMT}}$ and the finite element simulation with zero coupling coefficients are similar. However, in the FEM model with the non-zero piezoelectric coupling coefficients, we observe that the capacitances are 20-30% less than the $C_{\text{IDE}}^{\text{CMT}}$ or the FEM results with zero-coupling. For the larger gaps, these relative differences are asymptotical to a constant value. For the smaller gap, the relative differences are lower.

There are good reasons to think that there is a lowering of the dielectric constant when the piezoelectric effect is added to the model, because mechanical constraints imposed by the elastic system lead to a partial clamping similar to a thin film clamped on a rigid substrate as discussed in both cases of TBE (2.23) and IDE (2.51, 2.71). The resulting dielectric constant is then between a minimal value corresponding to complete clamping ε^S and a maximal value of ε^T corresponding to a dielectric constant of the free body.

For the CV curves in Fig.2.41a, around the coercive field, the piezoelectric has zero polarization, the unpoled piezoelectric is equivalent to a normal dielectric

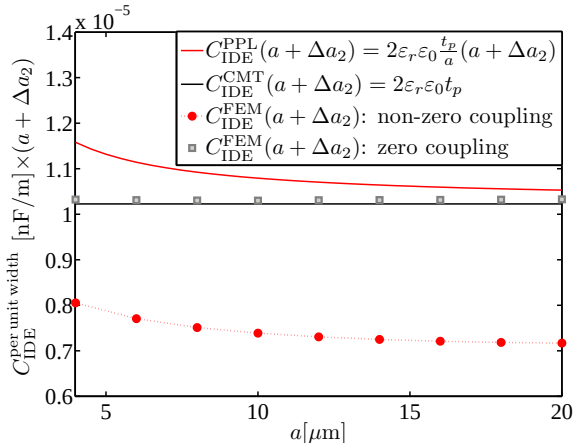

Figure 2.43: The capacitance per unit width multiplied by the effective gap distance $(a+\Delta a_2)$ of the piezoelectric layer in both cases of zero and non-zero piezoelectric coupling coefficients. The piezoelectric material is treated as homogeneous distribution with the permittivity of $\varepsilon_r\varepsilon_0 = \varepsilon_{33}^T = \varepsilon_{11}^T = 1000\varepsilon_0$.

material. Therefore, the dielectric constant for different gaps are equal. Away from the coercive field, the ferroelectric layer is poled, the piezoelectric effect is non-zero. The smaller capacitance is expected for the larger gap as observed in Fig.2.43 lead to the smaller dielectric constant.

Since the relative permittivity of the piezoelectric material appear gap dependent, the PV curves Fig.2.41b are not all coincident. For larger gaps, the relative permittivity is smaller; hence the charges are also smaller as shown in the figure.

Chapter 3

Plate actuators

In this chapter, circular plate actuators with different electrode configurations are investigated. Section 1 provides the structural description of the actuators. Section 2 presents the analyzes of the circular plate actuators with the TBE and the IDE configurations. Prior to the IDE configuration analysis, a circular plate actuator with an uniform d_{33} coupling is studied. Although poling of this structure seems impractical, analysis of this actuator is an important step in modelling the IDE actuator. Then, the deflection comparison between the TBE and IDE is presented in Section 3. Finally, the actuators with different configurations e.g interdigital, spiral, radial electrodes are investigated and compared in Section 4.

1 Structural description

A geometry of axisymmetric plate actuator is shown in Fig.3.1. Similar to the beam actuators, the cross section of the plate can include arbitrary number of layers of different materials i.e., an elastic structural material, a piezoelectric layer, some diffusion barriers and/or seed layers and the metal electrodes. The actuators are clamped at the perimeter. Motivated by the tunable lens application, the elastic substrate is made of a transparent material and there is a center opening letting the light through. Analogous to the clamped-clamped beam actuators, if the plates are fully covered, for both of the d_{33} and the d_{31} coupling, we can show that the deflection is zero.

For numerical study, a 1-mm and a 3-mm diameter circular plate-actuators are investigated. The thickness of the platinum electrodes (Young's modulus = 168GPa, Poison's ratio= 0.38) is fixed at t_e = 200nm, the thickness of the glass substrate (Young's modulus = 74GPa, Poison's ratio = 0.3) is t_b =20μm. These dimensions are chosen similar to a prototype of the tunable lens from Polight AS. The piezoelectric material are the same as the beam actuators chapter. The properties of the piezoelectric material are given in Table 2.1.

2 Actuation of the piezoelectric layered plate

2.1 Governing equations

A general model of a multilayer (M-layer) axisymmetric circular plate actuator Fig.3.2a is investigated. The analysis is based on the classical laminated plate

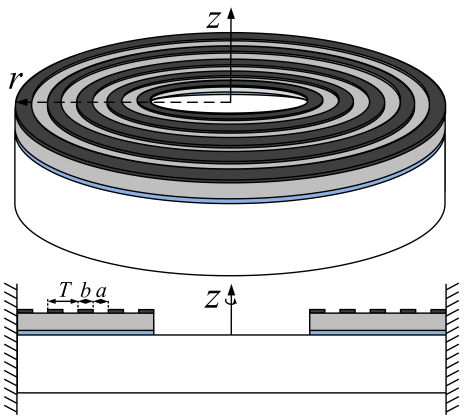

Figure 3.1: A circular plate piezoelectric actuator with an IDE electrode configuration. Different color correspond to different material i.e., black: electrodes, grey: piezoelectric layer, blue: diffusion layer and white: elastic substrate.

theory [121,122]. The theory is governed by the static equilibrium equations [123,124] of the axisymmetric plates

$$\frac{dN_r}{dr} + \frac{N_r - N_\theta}{r} = 0, \tag{3.1}$$

$$Q_r = \frac{dM_r}{dr} + \frac{M_r - M_\theta}{r}, \tag{3.2}$$

$$\frac{dQ_r}{dr} + P + \frac{Q_r}{r} = 0 \tag{3.3}$$

where P is a uniform pressure load on the structure. Q_r is the vertical shear force per unit length, $\mathbf{N} = \{N_r, N_\theta\}$ and $\mathbf{M} = \{M_r, M_\theta\}$ are the force and moment resultants per unit length in the radial and circumferential directions as indicated in Fig.3.2b. If the actuator has only electrical load, $P = 0$, equations (3.2) and (3.3) can be combined to

$$\frac{dM_r}{dr} + \frac{M_r - M_\theta}{r} = 0. \tag{3.4}$$

With the m^{th} layer located between z_{m+1} and z_m as shown in Fig.3.2c and assuming an electric field E_3^m in the poling direction within the layer, the linear elastic strain in this layer is

$$\left\{ \begin{array}{c} \varepsilon_r^m \\ \varepsilon_\theta^m \end{array} \right\} = \left\{ \begin{array}{c} \varepsilon_r \\ \varepsilon_\theta \end{array} \right\} + z \left\{ \begin{array}{c} \rho_r \\ \rho_\theta \end{array} \right\} - E_3^m \left\{ \begin{array}{c} d_{3i}^m \\ d_{3j}^m \end{array} \right\} \tag{3.5}$$

where i, j are determined based on piezoelectric coupling. The quantities $\{\varepsilon_r, \varepsilon_\theta\}$ and $\{\rho_r, \rho_\theta\}$ are the strains and curvatures in the reference plane and can be expressed in terms of the radial u and vertical w deflection in that plane as

$$\left\{ \begin{array}{c} \varepsilon_r \\ \varepsilon_\theta \end{array} \right\} = \left\{ \begin{array}{c} \frac{\partial u(r)}{\partial r} \\ \frac{u(r)}{r} \end{array} \right\}, \tag{3.6}$$

$$\left\{ \begin{array}{c} \rho_r \\ \rho_\theta \end{array} \right\} = \left\{ \begin{array}{c} -\frac{\partial^2 w(r)}{\partial r^2} \\ -\frac{\partial w(r)}{r \partial r} \end{array} \right\}. \tag{3.7}$$

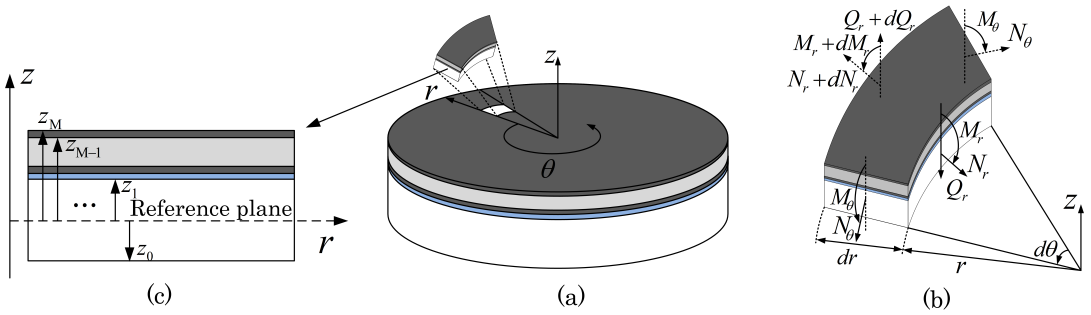

Figure 3.2: The circular multi-layered plate with conventional direction in the polar coordinate system

The linear constitutive relations between the stress and strain in the m^{th} layer via a stiffness matrix $[Q_m]$ is

$$\left\{ \begin{array}{c} \sigma_r^m \\ \sigma_\theta^m \end{array} \right\} = [Q_m] \left\{ \begin{array}{c} \varepsilon_r^m \\ \varepsilon_\theta^m \end{array} \right\}. \tag{3.8}$$

These built in stresses cause the force **N** and moment **M** resultants pr. unit length of the plate

$$\mathbf{N} = \left\{ \begin{array}{c} N_r \\ N_\theta \end{array} \right\} = \sum_{m=0}^{\mathrm{M}-1} \int_{z_m}^{z_{m+1}} \left\{ \begin{array}{c} \sigma_r^m \\ \sigma_\theta^m \end{array} \right\} dz = \mathbf{A} \left\{ \begin{array}{c} \varepsilon_r \\ \varepsilon_\theta \end{array} \right\} + \mathbf{B} \left\{ \begin{array}{c} \rho_r \\ \rho_\theta \end{array} \right\} - \left\{ \begin{array}{c} N_r^p \\ N_\theta^p \end{array} \right\}, \tag{3.9}$$

$$\mathbf{M} = \left\{ \begin{array}{c} M_r \\ M_\theta \end{array} \right\} = \sum_{m=0}^{\mathrm{M}-1} \int_{z_m}^{z_{m+1}} \left\{ \begin{array}{c} \sigma_r^m \\ \sigma_\theta^m \end{array} \right\} z dz = \mathbf{B} \left\{ \begin{array}{c} \varepsilon_r \\ \varepsilon_\theta \end{array} \right\} + \mathbf{D} \left\{ \begin{array}{c} \rho_r \\ \rho_\theta \end{array} \right\} - \left\{ \begin{array}{c} M_r^p \\ M_\theta^p \end{array} \right\} \tag{3.10}$$

where $\mathbf{A} = \sum_{m=0}^{\mathrm{M}-1} \int_{z_m}^{z_{m+1}} [Q_m]\, dz$, $\mathbf{B} = \sum_{m=0}^{\mathrm{M}-1} \int_{z_m}^{z_{m+1}} [Q_k]\, z dz$ and $\mathbf{D} = \sum_{m=0}^{\mathrm{M}-1} \int_{z_m}^{z_{m+1}} [Q_k]\, z^2 dz$ are 2×2 matrices representing respectively the extensional stiffness, bending-extensional coupling and bending stiffness of the layered plates. $\{N_r^p, N_\theta^p\}$ and $\{M_r^p, M_\theta^p\}$ expressed in (3.11), (3.12) are the force and moment resultants generated by the coupling from the piezoelectric layer.

$$\left\{ \begin{array}{c} N_r^p \\ N_\theta^p \end{array} \right\} = \sum_{m=0}^{\mathrm{M}-1} \int_{z_m}^{z_{m+1}} [Q_m]\, E_3^m \left\{ \begin{array}{c} d_{3i}^m \\ d_{3j}^m \end{array} \right\} dz, \tag{3.11}$$

$$\left\{ \begin{array}{c} M_r^p \\ M_\theta^p \end{array} \right\} = \sum_{m=0}^{\mathrm{M}-1} \int_{z_m}^{z_{m+1}} [Q_m]\, E_3^m \left\{ \begin{array}{c} d_{3i}^m \\ d_{3j}^m \end{array} \right\} z dz. \tag{3.12}$$

The governing equations of the layered plate are obtained by inserting (3.9) and (3.10) into (3.1) and (3.4).

2.2 Plate with TBE configuration

The circular plate actuators with the TBE configuration have been studied in literature. For instance, Prasad et al. [125, 126] have applied the classical laminated

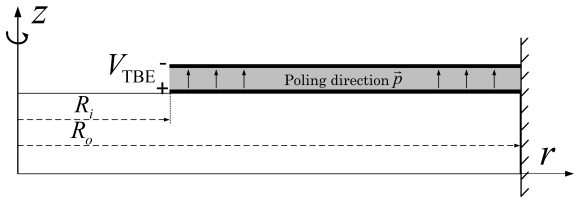

Figure 3.3: Circular plate actuator with the TBE configuration, the voltage difference between the electrodes is V_{TBE}.

plate theory to derive the linear static deflection of a circular piezoelectric unimorph actuator. Mo et al. [127] have adopted the technique to analyze the deflection of the unimorph-laminated plate under different boundary conditions and piezoelectric covered radius. However, these analyses limit for a two-layer structure with an elastic and a piezoelectric layer. Later, a closed-form analytical expression for static deflections of a circular axisymmetric plate with an arbitrary number of layers has been developed by Deshpande and Saggere [122]. Actuators with a center cover of piezoelectric material are considered in the above-mentioned works. In this Section, we investigate the actuation of the plate with a transparent region in the center of the disk.

For the TBE configuration Fig.3.3, the coupling matrix of the piezoelectric layer $\{d_{3i}^m, d_{3j}^m\}$ becomes $\{d_{31}^m, d_{31}^m\}$. Assuming plane stress conditions, the stress-strain stiffness matrix is expressed as

$$[Q_m] = \frac{Y_m}{1-\nu_m^2}\begin{bmatrix} 1 & \nu_m \\ \nu_m & 1 \end{bmatrix} \tag{3.13}$$

where Y_m, ν_m respectively are the Young modulus and Poison ratio of the m^{th} elastic layer. The Young modulus and the Poison ratio of the piezoelectric layer are $Y_p = \frac{1}{s_{11}}$, $\nu_p = -\frac{s_{12}}{s_{11}}$.

By introducing dimensionless radius $\hat{r} = \frac{r}{R_o}$, radial extension $\hat{u} = \frac{u}{R_o}$ and vertical deflection $\hat{w} = \frac{w}{R_o}$, and combining equations (3.1), (3.4), (3.9), (3.10), the governing equations of the layered plate are expressed as

$$\frac{A_{11}}{R_o}\left(\frac{\partial^2\hat{u}}{\partial\hat{r}^2} + \frac{1}{\hat{r}}\frac{\partial\hat{u}}{\partial\hat{r}} - \frac{\hat{u}}{\hat{r}^2}\right) - \frac{B_{11}}{R_o^2}\left(\frac{\partial^3\hat{w}}{\partial\hat{r}^3} + \frac{1}{\hat{r}}\frac{\partial^2\hat{w}}{\partial\hat{r}^2} - \frac{1}{\hat{r}^2}\frac{\partial\hat{w}}{\partial\hat{r}}\right) = 0, \tag{3.14}$$

$$\frac{B_{11}}{R_o}\left(\frac{\partial^2\hat{u}}{\partial\hat{r}^2} + \frac{1}{\hat{r}}\frac{\partial\hat{u}}{\partial\hat{r}} - \frac{\hat{u}}{\hat{r}^2}\right) - \frac{D_{11}}{R_o^2}\left(\frac{\partial^3\hat{w}}{\partial\hat{r}^3} + \frac{1}{\hat{r}}\frac{\partial^2\hat{w}}{\partial\hat{r}^2} - \frac{1}{\hat{r}^2}\frac{\partial\hat{w}}{\partial\hat{r}}\right) = 0. \tag{3.15}$$

The terms A_{11}, B_{11}, D_{11} are elements of the **A, B, D** matrices in (3.9), (3.10). The solutions satisfying (3.14) and (3.15) are

$$\hat{w} = c_1\hat{r}^2 + c_2\ln\hat{r} + c_3, \tag{3.16}$$

$$\hat{u} = c_4\hat{r} + \frac{c_5}{\hat{r}} \tag{3.17}$$

for some integration constants $c_1, \cdots, c_5$. In case of the partially covered plate actuator as shown in the Fig.3.3, the expression of the vertical deflection and radial

extension of the exterior annulus (denoted 'ext', $R_i \leq r \leq R_o$) and interior opening (denoted 'int', $0 \leq r \leq R_i$) regions are

$$\hat{w}^{\text{ext}}(\hat{r}) = C_1^{31}\hat{r}^2 + C_2^{31}\ln\hat{r} + C_3^{31}; \quad \hat{u}^{\text{ext}} = C_4^{31}\hat{r} + \frac{C_5^{31}}{\hat{r}} \tag{3.18}$$

$$\hat{w}^{\text{int}} = C_6^{31}\hat{r}^2 + C_7^{31}; \quad \hat{u}^{\text{int}} = C_8^{31}\hat{r} \tag{3.19}$$

where we introduced new constants for each domain and set two constants to zero in order to ensure that the logarithmic and $1/\hat{r}$ terms do not appear in $\hat{w}^{\text{int}}$ and $\hat{u}^{\text{int}}$. The deformations are then regular at $\hat{r} = 0$. The solutions for the remaining constants C_i^{31} are obtained by applying clamped boundary conditions around the perimeter as well as continuity conditions at the interface between the exterior and the interior regions. The resulting linear system of equations is

$$\begin{bmatrix}
1 & 0 & 1 & 0 & 0 & 0 & 0 & 0 \\
2 & 1 & 0 & 0 & 0 & 0 & 0 & 0 \\
0 & 0 & 0 & 1 & 1 & 0 & 0 & 0 \\
\frac{R_i^2}{R_o^2} & \ln(\frac{R_i}{R_o}) & 1 & 0 & 0 & -\frac{R_i^2}{R_o^2} & -1 & 0 \\
\frac{2R_i}{R_o} & \frac{R_o}{R_i} & 0 & 0 & 0 & -\frac{2R_i}{R_o} & 0 & 0 \\
0 & 0 & 0 & \frac{R_i}{R_o} & \frac{R_o}{R_i} & 0 & 0 & -\frac{R_i}{R_o} \\
\frac{2(D_{11}^{\text{ext}}+D_{12}^{\text{ext}})_{31}}{R_o} & \frac{-R_o(D_{11}^{\text{ext}}-D_{12}^{\text{ext}})_{31}}{R_i^2} & 0 & -(B_{11}^{\text{ext}}+B_{12}^{\text{ext}})_{31} & \frac{R_o^2(B_{11}^{\text{ext}}-B_{12}^{\text{ext}})_{31}}{R_i^2} & -\frac{2(D_{11}^{\text{int}}+D_{12}^{\text{int}})}{R_o} & 0 & (B_{11}^{\text{int}}+B_{12}^{\text{int}}) \\
\frac{2(B_{11}^{\text{ext}}+B_{12}^{\text{ext}})_{31}}{R_o} & \frac{-R_o(B_{11}^{\text{ext}}-B_{12}^{\text{ext}})_{31}}{R_i^2} & 0 & -(A_{11}^{\text{ext}}+A_{12}^{\text{ext}})_{31} & \frac{R_o^2(A_{11}^{\text{ext}}-A_{12}^{\text{ext}})_{31}}{R_i^2} & -\frac{2(B_{11}^{\text{int}}+B_{12}^{\text{int}})}{R_o} & 0 & (A_{11}^{\text{int}}+A_{12}^{\text{int}})
\end{bmatrix}
\begin{Bmatrix} C_1^{31} \\ C_2^{31} \\ C_3^{31} \\ C_4^{31} \\ C_5^{31} \\ C_6^{31} \\ C_7^{31} \\ C_8^{31} \end{Bmatrix} = \begin{Bmatrix} 0 \\ 0 \\ 0 \\ 0 \\ 0 \\ 0 \\ -M_r^p \\ -N_r^p \end{Bmatrix}. \tag{3.20}$$

N_r^p, M_r^p are given by the equations (3.11), (3.12) and are independent of r because the electric field inside the piezoelectric layer of the d_{31} actuator is. The field is

$$E_3^p = \frac{V_{\text{TBE}}}{t_p}. \tag{3.21}$$

From the first five equations in (3.20) the following relations can be extracted

$$C_2^{31} = -2C_1^{31}; \quad C_3^{31} = -C_1^{31}; \quad C_6^{31} = \frac{R_i^2 - R_o^2}{R_i^2}C_1^{31}; \quad C_7^{31} = 2\ln\frac{R_o}{R_i}C_1^{31} \tag{3.22}$$

$$C_5^{31} = -C_4^{31}; \quad C_8^{31} = \frac{R_i^2 - R_o^2}{R_i^2}C_4^{31}. \tag{3.23}$$

Inserting these relations into the two last equations of (3.20) and defining

$$A = (A_{11}^{\text{ext}} + A_{12}^{\text{ext}})_{31} - (A_{11}^{\text{int}} + A_{12}^{\text{int}}) + \frac{R_o^2}{R_i^2}\left[(A_{11}^{\text{ext}} - A_{12}^{\text{ext}})_{31} + (A_{11}^{\text{int}} + A_{12}^{\text{int}})\right], \tag{3.24}$$

$$B = (B_{11}^{\text{ext}} + B_{12}^{\text{ext}})_{31} - (B_{11}^{\text{int}} + B_{12}^{\text{int}}) + \frac{R_o^2}{R_i^2}\left[(B_{11}^{\text{ext}} - B_{12}^{\text{ext}})_{31} + (B_{11}^{\text{int}} + B_{12}^{\text{int}})\right], \tag{3.25}$$

and

$$D = (D_{11}^{\text{ext}} + D_{12}^{\text{ext}})_{31} - (D_{11}^{\text{int}} + D_{12}^{\text{int}}) + \frac{R_o^2}{R_i^2}\left[(D_{11}^{\text{ext}} - D_{12}^{\text{ext}})_{31} + (D_{11}^{\text{int}} + D_{12}^{\text{int}})\right] \quad (3.26)$$

leads to the solutions

$$C_1^{31} = \frac{R_o}{2}\frac{BN_r^p - AM_r^p}{AD - B^2}, \quad (3.27)$$

$$C_4^{31} = \frac{DN_r^p - BM_r^p}{AD - B^2}. \quad (3.28)$$

Finally, the maximum deflection of the plate is

$$(\hat{w}_0^{31})_{\max} = \hat{w}_0^{\text{int}}(\hat{r} = 0) = C_7^{31} = R_o \ln\left(\frac{R_o}{R_i}\right)\frac{BN_r^p - AM_r^p}{AD - B^2}. \quad (3.29)$$

For a thin film, the extensional stiffness, bending-extensional coupling and bending stiffness can be approximated as equal in the exterior annulus and interior opening regions, i.e. we set $A_{xy,31}^{\text{ext}} \approx A_{xy}^{\text{int}}$, $B_{xy,31}^{\text{ext}} \approx B_{xy}^{\text{int}}$, $D_{xy,31}^{\text{ext}} \approx D_{xy}^{\text{int}}$. This approximation gives

$$D \approx \frac{R_o^2}{R_i^2}(D_{11,31}^{\text{ext}} + D_{11}^{\text{int}}); \quad B \approx \frac{R_o^2}{R_i^2}(B_{11,31}^{\text{ext}} + B_{11}^{\text{int}}); \quad A \approx \frac{R_o^2}{R_i^2}(A_{11,31}^{\text{ext}} + A_{11}^{\text{int}}) \quad (3.30)$$

and by choosing the reference plane such that $B_{11}^{\text{int}} = 0$, we also have $B_{11,31}^{\text{ext}} \approx 0$ and

$$(\hat{w}^{31})_{\max} \approx \frac{R_i^2}{R_o}\ln\left(\frac{R_o}{R_i}\right)\frac{M_r^p}{D_{11,31}^{\text{ext}} + D_{11}^{\text{int}}} = \frac{R_o}{t_p}\frac{\bar{\alpha}}{D_{11,31}^{\text{ext}} + D_{11}^{\text{int}}}X^2 \ln X \quad (3.31)$$

where $X = R_i/R_o$ and

$$\bar{\alpha} = \frac{(1+\nu_p)Y_p d_{31}}{2(1-{\nu_p}^2)}(z_{p+1}^2 - z_p^2)V_{\text{TBE}}. \quad (3.32)$$

From (3.31), if the actuator is fully covered ($X = 0$), the center deflection is zero.

For a fixed value of the plate radius R_o, the optimum radius of the interior opening is found by forcing the first derivative of equation (3.31) with respect to X to zero and results in

$$X = \frac{R_i}{R_o} = \frac{1}{\sqrt{e}}. \quad (3.33)$$

The result shows that the optimal structural design of the thin film piezoelectric actuator operated in d_{31} mode is independent of the material choice.

Fig.3.4a compares results obtained by the finite element calculation and the predictions of the analytical models (3.20) and (3.31) at different values of piezoelectric thickness and opening radius. The potential difference applied across the electrodes is chosen to set the electric field strength of the piezoelectric layer to a fixed value of 1MV/m. Analytical results agree with the FEM simulation. The simplified thin-film model predicts the plate deflection well. Thicker piezoelectric layer results in larger deflection. The optimum radius around 300 μm agrees with the calculated ratio (3.33). The cross section of the deflection shape of the plate is shown in Fig.3.4b.

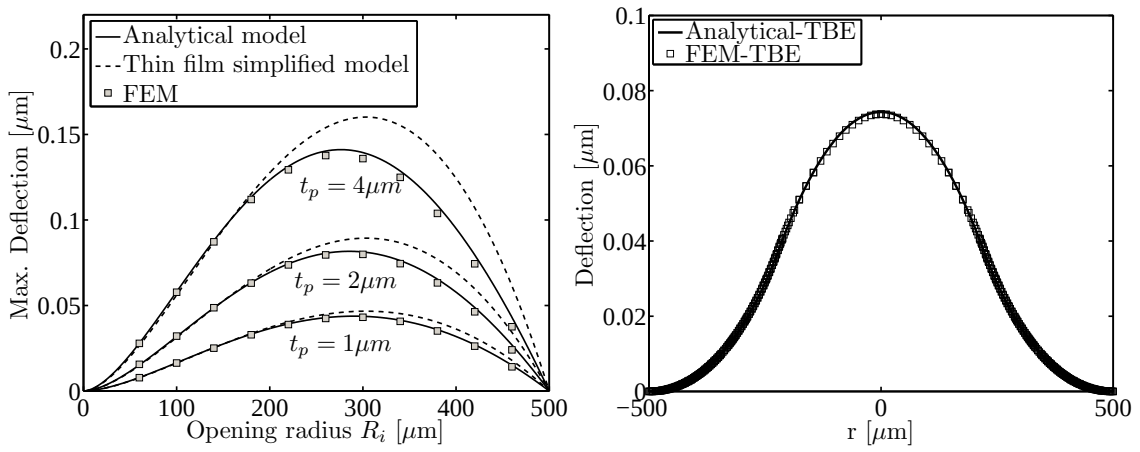

(a) (b)

Figure 3.4: (a) Deflection of the TBE actuator at different piezoelectric layer thicknesses = 1 - 4μm and opening radius R_o= 500 μm. (b) The deflection shapes of the TBE actuator at R_i=220μm, the piezoelectric thickness t_p=2μm, the applied potential is $V_{\text{TBE}} = 2$V.

2.3 Plate with d_{33} coupling

The structure shown in Fig.3.5 is investigated in this section. The electrodes are not patterned on the surface but on the two edges of the piezoelectric layer. We refer to this transducer as a non-patterned electrode (NPE) actuator. If an in-plane radial polarization can be established, the d_{33} coupling is employed.

For the NPE configuration, the coupling matrix of the piezoelectric layer $\{d_{3i}^m, d_{3j}^m\}$ becomes $\{d_{33}^m, d_{31}^m\}$, the stress-strain stiffness matrices in others elastic layer are similar as (3.13) but inside the piezoelectric layer

$$[Q_p] = \frac{1}{1-\nu_{11}\nu_{33}} \begin{bmatrix} Y_{33} & \nu_{33}Y_{11} \\ \nu_{11}Y_{33} & Y_{11} \end{bmatrix} \tag{3.34}$$

where $Y_{33} = 1/s_{33}$, $Y_{11} = 1/s_{11}$, $\nu_{33} = -s_{13}/s_{33}$ and $\nu_{11} = -s_{13}/s_{11}$.

Different from the d_{31} case, the electric field distribution in the d_{33} coupling actuator is dependent on radial distance:

$$E_3^p(r) = \frac{V_{\text{NPE}}}{r \ln\left(\frac{R_o}{R_i}\right)}. \tag{3.35}$$

Following the same procedure as in the d_{31} case, the equations for the layered plate with d_{33} actuation are

$$\frac{A_{11}}{R_o}\left(\frac{\partial^2\hat{u}}{\partial\hat{r}^2} + \frac{1}{\hat{r}}\frac{\partial\hat{u}}{\partial\hat{r}} - \frac{A_{22}}{A_{11}}\frac{\hat{u}}{\hat{r}^2}\right) - \frac{B_{11}}{R_o^2}\left(\frac{\partial^3\hat{w}}{\partial\hat{r}^3} + \frac{1}{\hat{r}}\frac{\partial^2\hat{w}}{\partial\hat{r}^2} - \frac{B_{22}}{B_{11}}\frac{\partial\hat{w}}{\hat{r}^2\partial\hat{r}}\right) = \frac{-N_\theta^p}{r}, \tag{3.36}$$

$$\frac{B_{11}}{R_o}\left(\frac{\partial^2\hat{u}}{\partial\hat{r}^2} + \frac{1}{\hat{r}}\frac{\partial\hat{u}}{\partial\hat{r}} - \frac{B_{22}}{B_{11}}\frac{\hat{u}}{\hat{r}^2}\right) - \frac{D_{11}}{R_o^2}\left(\frac{\partial^3\hat{w}}{\partial\hat{r}^3} + \frac{1}{\hat{r}}\frac{\partial^2\hat{w}}{\partial\hat{r}^2} - \frac{D_{22}}{D_{11}}\frac{\partial\hat{w}}{\hat{r}^2\partial\hat{r}}\right) = \frac{-M_\theta^p}{r}. \tag{3.37}$$

The terms $A_{11}, B_{11}, D_{11}, A_{22}, B_{22}, D_{22}$ are elements of the **A, B, D** matrices in (3.9), (3.10). N_θ^p, M_θ^p are given by (3.11), (3.12). These parameters are calculated from the stiffness matrices of (3.13), (3.34) and the electric field (3.35).

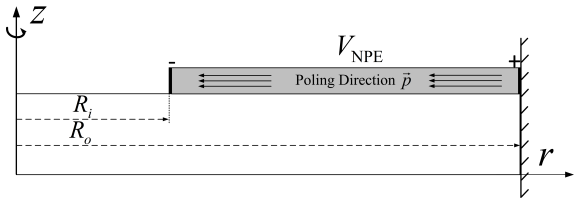

Figure 3.5: Circular plate actuator with the NPE configuration. The electrodes are patterned on two edges of the piezoelectric layer. The voltage difference V_{NPE} is applied between these electrodes.

For a thin piezoelectric film $A_{11} \approx A_{22}$, $B_{11} \approx B_{22}$, $D_{11} \approx D_{22}$, the left hand side of (3.36, 3.37) and (3.14, 3.15) will share the similar expressions. Hence, the general solutions of (3.36) and (3.37) are the superposition of the homogeneous solutions of (3.16), (3.17) and the particular solutions and can be written as

$$\hat{w} = c_1\hat{r}^2 + c_2 \ln \hat{r} + c_3 - k_2\hat{r}, \tag{3.38}$$

$$\hat{u} = c_4\hat{r} + \frac{c_5}{\hat{r}} - k_1 \tag{3.39}$$

where $k_1 = \frac{r}{R_o}\frac{-D_{11}N_\theta^p + B_{11}M_\theta^p}{A_{11}D_{11} - B_{11}^2}$, $k_2 = r\frac{-B_{11}N_\theta^p + A_{11}M_\theta^p}{A_{11}D_{11} - B_{11}^2}$. Notice that these parameters are independent of r due to the factor $1/r$ in the electric field formula (3.35) inside M_θ^p and N_θ^p.

For the partially covered elastic substrate Fig.3.5, the expressions for the vertical deflection and radial extension of the exterior annulus and interior opening regions are

$$\hat{w}^{\mathrm{ext}} = C_1^{33}\hat{r}^2 + C_2^{33}\ln\hat{r} + C_3^{33} - K_2\hat{r}; \quad \hat{u}^{\mathrm{ext}} = C_4^{33}\hat{r} + \frac{C_5^{33}}{\hat{r}} - K_1, \tag{3.40}$$

$$\hat{w}^{\mathrm{int}} = C_6^{33}\hat{r}^2 + C_7^{33}; \quad \hat{u}^{\mathrm{int}} = C_8^{33}\hat{r} \tag{3.41}$$

where the index '33' refers to the d_{33} coupling and K_1, K_2 are obtained by the formulas for k_1, k_2 by substituting A_{11}, B_{11}, D_{11} with $A_{11,33}^{\mathrm{ext}}, B_{11,33}^{\mathrm{ext}}, D_{11,33}^{\mathrm{ext}}$. The same boundary conditions as before now lead to equations for the unknown constants on the form

$$\begin{bmatrix}
1 & 0 & 1 & 0 & 0 & 0 & 0 & 0 \\
2 & 1 & 0 & 0 & 0 & 0 & 0 & 0 \\
0 & 0 & 0 & 1 & 1 & 0 & 0 & 0 \\
\frac{R_i^2}{R_i^2} & \ln(\frac{R_i}{R_o}) & 1 & 0 & 0 & -\frac{R_i^2}{R_i^2} & -1 & 0 \\
\frac{2R_i}{R_o} & \frac{R_o}{R_i} & 0 & 0 & 0 & -\frac{2R_i}{R_o} & 0 & 0 \\
0 & 0 & 0 & \frac{R_i}{R_o} & \frac{R_o}{R_i} & 0 & 0 & -\frac{R_i}{R_o} \\
\frac{2(D_{11}^{\mathrm{ext}}+D_{12}^{\mathrm{ext}})_{33}}{R_o} & \frac{-R_o(D_{11}^{\mathrm{ext}}-D_{12}^{\mathrm{ext}})_{33}}{R_i^2} & 0 & -(B_{11}^{\mathrm{ext}}+B_{12}^{\mathrm{ext}})_{33} & \frac{R_o^2(B_{11}^{\mathrm{ext}}-B_{12}^{\mathrm{ext}})_{33}}{R_i^2} & -\frac{2(D_{11}^{\mathrm{int}}+D_{12}^{\mathrm{int}})}{R_o} & 0 & (B_{11}^{\mathrm{int}}+B_{12}^{\mathrm{int}}) \\
\frac{2(B_{11}^{\mathrm{ext}}+B_{12}^{\mathrm{ext}})_{33}}{R_o} & \frac{-R_o(B_{11}^{\mathrm{ext}}-B_{12}^{\mathrm{ext}})_{33}}{R_i^2} & 0 & -(A_{11}^{\mathrm{ext}}+A_{12}^{\mathrm{ext}})_{33} & \frac{R_o^2(A_{11}^{\mathrm{ext}}-A_{12}^{\mathrm{ext}})_{33}}{R_i^2} & -\frac{2(B_{11}^{\mathrm{int}}+B_{12}^{\mathrm{int}})}{R_o} & 0 & (A_{11}^{\mathrm{int}}+A_{12}^{\mathrm{int}})
\end{bmatrix}$$

$$\begin{Bmatrix} C_1^{33} \\ C_2^{33} \\ C_3^{33} \\ C_4^{33} \\ C_5^{33} \\ C_6^{33} \\ C_7^{33} \\ C_8^{33} \end{Bmatrix} = \begin{Bmatrix} K_2 \\ K_2 \\ K_1 \\ K_2\frac{R_i}{R_o} \\ K_2 \\ K_1 \\ -M_{r=R_i}^p - \frac{R_o B_{12,33}^{\mathrm{ext}} K_1}{R_i} + \frac{D_{12,33}^{\mathrm{ext}} K_2}{R_i} \\ -N_{r=R_i}^p - \frac{R_o A_{12,33}^{\mathrm{ext}} K_1}{R_i} + \frac{B_{12,33}^{\mathrm{ext}} K_2}{R_i} \end{Bmatrix} \tag{3.42}$$

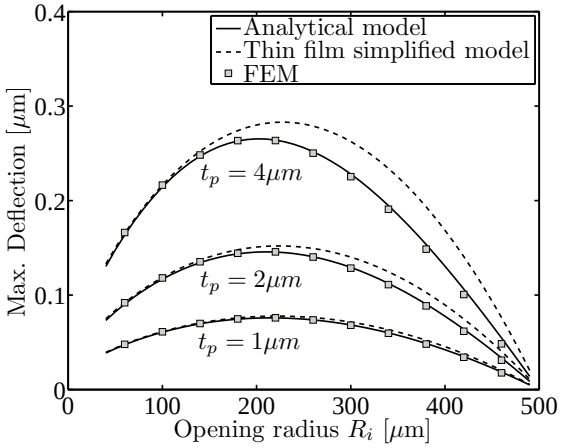

Figure 3.6: Deflection of the NPE actuator at different piezoelectric layer thicknesses t_p=1-4 μm and opening radius R_o= 500 μm.

where $M^p_{r=R_i}, N^p_{r=R_i}$ follow from equations (3.11), (3.12) by using (3.13), (3.34), and (3.35) at $r = R_i$. It is noticed that M^p_r, N^p_r in the d_{33} mode are dependent on radial distance. Here, we do not distinguish the interior stiffness constants $(A^{\text{int}}_{xy}, B^{\text{int}}_{xy}, D^{\text{int}}_{xy})$ for the d_{33} and the d_{31} mode because they are identical.

We again apply the thin-film simplification which removes the extensional-bending coupling and treats the interior stiffness constants equal the exterior ones as in the d_{31} case. The formula for the maximum deflection of the plate is

$$(\hat{w}^{33})_{\max} \approx \frac{\bar{\gamma}}{2D^{\text{ext}}_{11,33}} \left(\frac{X-1}{\ln X} - X \left(\frac{\bar{\beta}}{\bar{\gamma}} \frac{2D^{\text{ext}}_{11,33}}{D^{\text{ext}}_{11,33} + D^{\text{int}}_{11}} + \frac{2D^{\text{int}}_{11}}{D^{\text{ext}}_{11,33} + D^{\text{int}}_{11}} \right) \right) \qquad (3.43)$$

where $\bar{\beta} = \frac{Y_{33}d_{33}+\nu_{33}Y_{11}d_{31}}{2(1-\nu_{11}\nu_{33})}(z^2_{p+1} - z^2_p)V_{\text{NPE}}$ and $\bar{\gamma} = \frac{Y_{11}d_{31}+\nu_{11}Y_{33}d_{33}}{2(1-\nu_{11}\nu_{33})}(z^2_{p+1} - z^2_p)V_{\text{NPE}}$. From (3.43), if the actuator is fully covered ($X = 0$), the center deflection is also zero.

Different from the d_{31} coupling, the optimum radius of the d_{33} actuator with thin-film simplification (found by forcing the first derivative of (3.43) with respect to X to zero) is dependent on material choice. For our case, the optimum value is $X = R_i/R_o = 0.44$.

Fig. 3.6 compares the FEM and the analytical model for the d_{33} plate actuator at different piezoelectric layer thickness. The analytical results agree well with the FEM simulation. This conclusion also applies to the simplified thin film approximation as seen from the results on the deflection of the plate. The maximum deflection at a radius of about 220μm is consistent with the ratio of 0.44 calculated above.

2.4 Plate with IDE configuration

The NPE is an ideal case of the d_{33} coupling actuator. However, since the distance between the two electrodes is large, it requires a very large voltage (≈10kV) to pole the piezoelectric material. Hence, poling of this thin piezoelectric layer seems impractical. As a typical implementation of the d_{33} coupling, the interdigital electrode (IDE) actuator shown in Fig.3.7a is investigated. Some plate actuators with the IDE configuration have been fabricated [128--130]. Nevertheless, the IDE actuators is mostly modelled by using the finite element method [131, 132]. In this Section, an analytical model of the IDE actuator is presented.

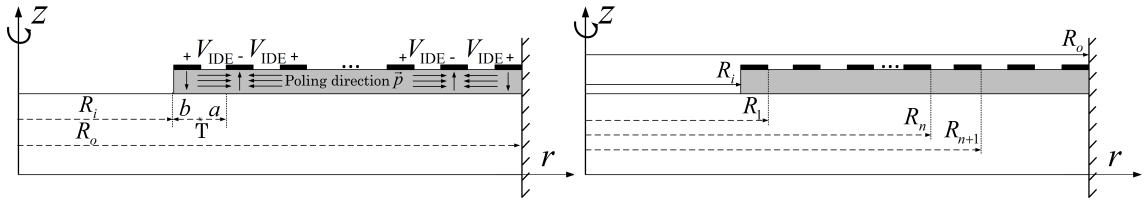

Figure 3.7: a) Circular plate actuator with the IDE configuration, the voltage difference between the neighbouring electrodes is V_{IDE}. (b) The definition of R_n, R_n is the distance from the center of the plate to the start of the n^{th} gap.

The IDE actuator is poled in different directions in the piezoelectric material when the same electrodes are used for the poling. Our model assumes a radial uniform polarization in regions between the neighbouring IDE fingers (active regions) while the polarization in regions beneath the fingers (passive regions) are vertically orientated as illustrated in Fig.3.7a. By assuming homogeneous electric field in the active regions, this field is found as

$$E_3^p(r) = \frac{V_{\text{IDE}}}{r \ln\left(\frac{R_n+a}{R_n}\right)} \tag{3.44}$$

where R_n is defined in Fig.3.7b.

To calculate the deflection of the IDE actuator, we use a recursive method.

By chosing the reference plane at $z = t_b/2$ and with a thin piezoelectric film assumption, the solution for the deflection $\hat{w}$ in the active regions is given as (3.40). Then, at position R_n

$$\mathbf{w}(R_n) = \begin{Bmatrix} \hat{w}(R_n) \\ \hat{w}'(R_n) \\ \hat{u}(R_n) \\ N_r(R_n) \\ M_r(R_n) \end{Bmatrix} \tag{3.45}$$

can be derived using (3.9), (3.10) and (3.40), which is

$$\mathbf{w}(R_n) = \begin{bmatrix} \frac{R_n^2}{R_o^2} & \ln(\frac{R_n}{R_o}) & 1 & 0 & 0 \\ \frac{2R_n}{R_o} & \frac{R_o}{R_n} & 0 & 0 & 0 \\ 0 & 0 & 0 & \frac{R_n}{R_o} & \frac{R_o}{R_n} \\ -\frac{2(B_{11}^{\text{ext}}+B_{12}^{\text{ext}})_{33}}{R_o} & \frac{R_o(B_{11}^{\text{ext}}-B_{12}^{\text{ext}})_{33}}{R_n^2} & 0 & (A_{11}^{\text{ext}}+A_{12}^{\text{ext}})_{33} & -\frac{R_o^2(A_{11}^{\text{ext}}-A_{12}^{\text{ext}})_{33}}{R_n^2} \\ -\frac{2(D_{11}^{\text{ext}}+D_{12}^{\text{ext}})_{33}}{R_o} & \frac{R_o(D_{11}^{\text{ext}}-D_{12}^{\text{ext}})_{33}}{R_n^2} & 0 & (B_{11}^{\text{ext}}+B_{12}^{\text{ext}})_{33} & -\frac{R_o^2(B_{11}^{\text{ext}}-B_{12}^{\text{ext}})_{33}}{R_n^2} \end{bmatrix} \begin{Bmatrix} C_{1,n}^{33} \\ C_{2,n}^{33} \\ C_{3,n}^{33} \\ C_{4,n}^{33} \\ C_{5,n}^{33} \end{Bmatrix} + \begin{Bmatrix} -K_2\frac{R_n}{R_o} \\ -K_2 \\ -K_1 \\ -\frac{R_o A_{12,33}^{\text{ext}} K_1}{R_n} + \frac{B_{12,33}^{\text{ext}} K_2}{R_n} \\ -\frac{R_o B_{12,33}^{\text{ext}} K_1}{R_n} + \frac{D_{12,33}^{\text{ext}} K_2}{R_n} \end{Bmatrix} + \begin{Bmatrix} 0 \\ 0 \\ 0 \\ -N_{r=R_n}^p \\ -M_{r=R_n}^p \end{Bmatrix}. \tag{3.46}$$

Denoting the four matrices on the right side of (3.46) by $\mathbf{R}_{33}(R_n)$, $\mathbf{C}_{33}^n$, $\mathbf{K}_{33}(R_n)$ and $\mathbf{M}^p(R_n)$, we can rewrite (3.46)

$$\mathbf{w}(R_n) = \mathbf{R}_{33}(R_n)\mathbf{C}_{33}^n + \mathbf{K}_{33}(R_n) + \mathbf{M}^p(R_n). \tag{3.47}$$

The coefficient matrix $\mathbf{C}_{33}^{n}$ is

$$\mathbf{C}_{33}^{n} = \mathbf{R}_{33}^{-1}(R_n)\left[\mathbf{w}(R_n) - \mathbf{K}_{33}(R_n) - \mathbf{M}^{p}(R_n)\right]. \tag{3.48}$$

Similar to (3.47), we can formulate $\mathbf{w}(R_n + a)$, which is

$$\mathbf{w}(R_n + a) = \mathbf{R}_{33}(R_n + a)\mathbf{C}_{33}^{n} + \mathbf{K}_{33}(R_n + a) + \mathbf{M}^{p}(R_n + a). \tag{3.49}$$

Substituting (3.48) to (3.49) and denoting $\mathbf{R}_{33,\text{act}}(R_n) = \mathbf{R}_{33}(R_n + a)\mathbf{R}_{33}^{-1}(R_n)$, we get

$$\mathbf{w}(R_n+a) = \mathbf{R}_{33,\text{act}}(R_n)\left[\mathbf{w}(R_n) - \mathbf{K}_{33}(R_n) - \mathbf{M}^{p}(R_n)\right] + \mathbf{K}_{33}(R_n+a) + \mathbf{M}^{p}(R_n+a). \tag{3.50}$$

In the passive regions, by using the solution for the deflection as given (3.18), together with (3.9) and (3.10), $\mathbf{w}(R_n + a)$ is

$$\mathbf{w}(R_n + a) = \begin{bmatrix} \frac{(R_n+a)^2}{R_o^2} & \ln(\frac{R_n+a}{R_o}) & 1 & 0 & 0 \\ \frac{2(R_n+a)}{R_o} & \frac{R_o}{R_n+a} & 0 & 0 & 0 \\ 0 & 0 & 0 & \frac{R_n+a}{R_o} & \frac{R_o}{R_n+a} \\ -\frac{2(B_{11}^{\text{ext}}+B_{12}^{\text{ext}})_{31}}{R_o} & \frac{R_o(B_{11}^{\text{ext}}-B_{12}^{\text{ext}})_{31}}{(R_n+a)^2} & 0 & (A_{11}^{\text{ext}}+A_{12}^{\text{ext}})_{31} & -\frac{R_o^2(A_{11}^{\text{ext}}-A_{12}^{\text{ext}})_{31}}{(R_n+a)^2} \\ -\frac{2(D_{11}^{\text{ext}}+D_{12}^{\text{ext}})_{31}}{R_o} & \frac{R_o(D_{11}^{\text{ext}}-D_{12}^{\text{ext}})_{31}}{(R_n+a)^2} & 0 & (B_{11}^{\text{ext}}+B_{12}^{\text{ext}})_{31} & -\frac{R_o^2(B_{11}^{\text{ext}}-B_{12}^{\text{ext}})_{31}}{(R_n+a)^2} \end{bmatrix} \begin{Bmatrix} C_{1,n}^{31} \\ C_{2,n}^{31} \\ C_{3,n}^{31} \\ C_{4,n}^{31} \\ C_{5,n}^{31} \end{Bmatrix}. \tag{3.51}$$

By using the similar notation convention as in (3.47), we rewrite (3.51) as

$$\mathbf{w}(R_n + a) = \mathbf{R}_{31}(R_n + a)\mathbf{C}_{31}^{n}. \tag{3.52}$$

Then

$$\mathbf{C}_{31}^{n} = \mathbf{R}_{31}^{-1}(R_n + a)\mathbf{w}(R_n + a). \tag{3.53}$$

Similar to (3.52), $\mathbf{w}(R_{n+1})$ is

$$\mathbf{w}(R_{n+1}) = \mathbf{R}_{31}(R_{n+1})\mathbf{C}_{31}^{n}. \tag{3.54}$$

Substituting (3.53) into (3.54) and denoting $\mathbf{R}_{31,\text{pass}}(R_n+a) = \mathbf{R}_{31}(R_{n+1})\mathbf{R}_{31}^{-1}(R_n+a)$, then

$$\mathbf{w}(R_{n+1}) = \mathbf{R}_{31,\text{pass}}(R_n + a)\mathbf{w}(R_n + a). \tag{3.55}$$

Finally, substituting (3.50) to (3.55) and denoting $\mathbf{R}(R_n) = \mathbf{R}_{31,\text{pass}}(R_n + a)\mathbf{R}_{33,\text{act}}($ $R_n)$, the recursive relation between $\mathbf{w}(R_{n+1})$ and $\mathbf{w}(R_n)$ is

$$\mathbf{w}(R_{n+1}) = \mathbf{R}(R_n)\left[\mathbf{w}(R_n) - \mathbf{K}_{33}(R_n) - \mathbf{M}^{p}(R_n)\right] + \mathbf{R}_{31,\text{pass}}\left[\mathbf{K}_{33}(R_n + a) + \mathbf{M}^{p}(R_n + a)\right]. \tag{3.56}$$

In the opening region, the deflection are given in (3.19) or (3.41), then $\mathbf{w}(R_{\text{i}})$ is

$$\mathbf{w}(R_{\text{i}}) = \begin{Bmatrix} \hat{w}(R_{\text{i}}) \\ \hat{w}'(R_{\text{i}}) \\ \hat{u}(R_{\text{i}}) \\ N_r(R_{\text{i}}) \\ M_r(R_{\text{i}}) \end{Bmatrix} = \begin{bmatrix} \frac{R_{\text{i}}^2}{R_o^2} & 1 & 0 \\ \frac{2R_{\text{i}}}{R_o} & 0 & 0 \\ 0 & 0 & \frac{R_{\text{i}}}{R_o} \\ -\frac{2(B_{11}^{\text{int}}+B_{12}^{\text{int}})}{R_o} & 0 & (A_{11}^{\text{int}}+A_{12}^{\text{int}}) \\ -\frac{2(D_{11}^{\text{int}}+D_{12}^{\text{int}})}{R_o} & 0 & (B_{11}^{\text{int}}+B_{12}^{\text{int}}) \end{bmatrix} \begin{Bmatrix} C_6^{\text{IDE}} \\ C_7^{\text{IDE}} \\ C_8^{\text{IDE}} \end{Bmatrix}. \tag{3.57}$$

Similar to (3.55), we can get

$$\mathbf{w}(R_1) = \mathbf{w}(R_{\text{i}} + b) = \mathbf{R}_{31}(R_{\text{i}} + b)\mathbf{R}_{31}^{-1}(R_{\text{i}})\mathbf{w}(R_{\text{i}}), \tag{3.58}$$

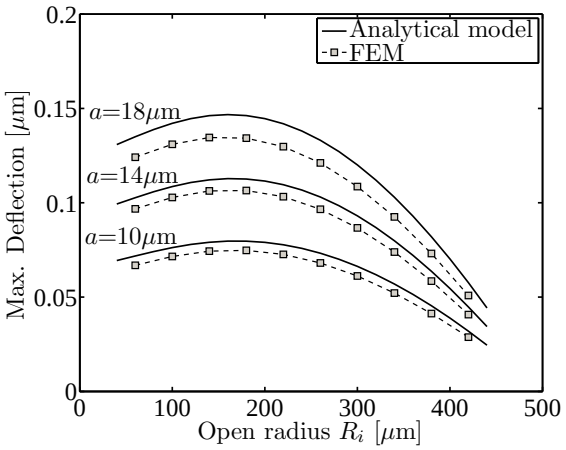

Figure 3.8: Deflection of the IDE actuator. The piezoelectric layer thickness is t_p=2μm and the pitch is T= 20μm.

the matrices $\mathbf{R}_{31}(R_\mathrm{i}+b)$ or $\mathbf{R}_{31}(R_\mathrm{i})$ are defined in a similar way with the matrix $\mathbf{R}_{31}(R_n+a)$ in (3.52) and $\mathbf{w}(R_\mathrm{i})$ is given in (3.57).

Using (3.58) and the recursive relation (3.56), we can find $\mathbf{w}(R_o)$. Applying the clamped boundary condition i.e., $w(R_o)=w'(R_o)=u(R_o)=0$, the values of $C_6^{\mathrm{IDE}}, C_7^{\mathrm{IDE}}, C_8^{\mathrm{IDE}}$, N_r and M_r can be found. Therefore, the maximum deflection of the circular plate actuator is

$$(\hat{w}^{\mathrm{IDE}})_{\max} = C_7^{\mathrm{IDE}}. \tag{3.59}$$

Figure 3.8 presents maximum deflection of the IDE plate actuator with different gaps calculated by the FEM and the analytical model. The analytical and FEM results are qualitatively agreed. Both models predict the optimal opening radius around 180μm, larger gaps give higher deflection.

3 Deflection comparison between plate actuators

The comparison between actuators with different electrode configurations is demonstrated at the same electric field strength. The potential difference applied across the electrodes is chosen to set the electric field strength in the piezoelectric layers to a fixed value of 1MV/m. The applied electric potential in the different cases (as indicated by subscripts) are related by

$$\frac{V_{\mathrm{IDE}}}{a} = \frac{V_{\mathrm{NPE}}}{R_o - R_i} = \frac{V_{\mathrm{TBE}}}{t_p}. \tag{3.60}$$

For the thin-film simplification, from the equations (3.31) and (3.43), the maximum deflection ratio between the NPE and the TBE actuators is found. The results shown in Fig.3.9a demonstrate that the ratio is always larger than 1. Hence, the d_{33} actuator gives more deflection than the d_{31} counterpart if the same electric field strength is applied. The ratio is decreased when the opening radius is increased. Actually, designing the actuator with very large opening radius ratio ($R_i \approx R_o$) is not interesting because such a design gives very small deflection as shown in Fig.3.4a, Fig.3.6, Fig.3.8 and equations (3.31), (3.43).

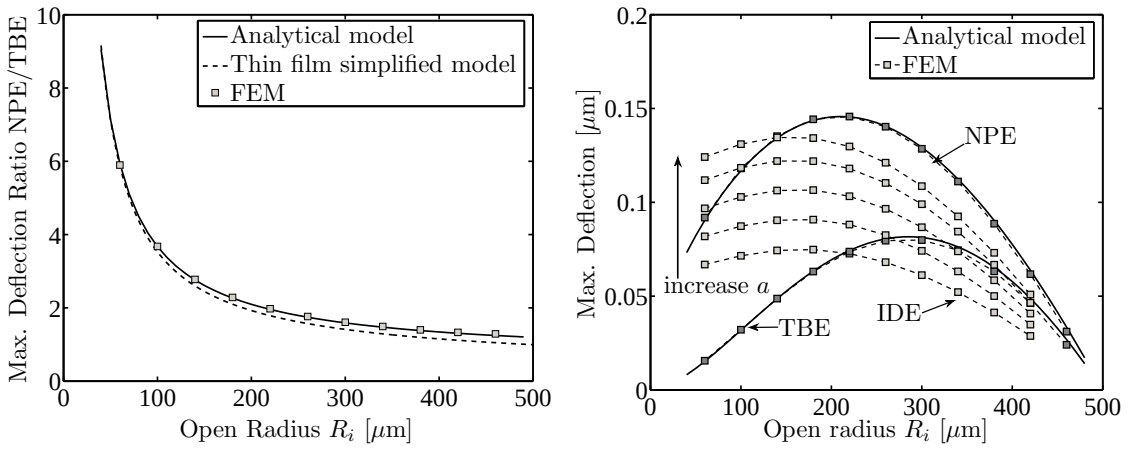

Figure 3.9: Comparison between actuators with different electrode configurations: (a) ratio of maximum deflections between NPE and TBE actuator, the piezoelectric layer thickness is t_p= 2 μm. (b) IDE plate actuator deflection at different gap a=10-18 μm. The pitch and piezoelectric thickness are fixed at T=20μm and t_p= 2μmm. The IDE deflection has a tendency to approach the NPE deflection when the gap is increased.

Fig.3.9b compares different actuator deflections at the same electric field strength (3.60). By increasing the gap to pitch ratio, the maximum deflection of the IDE actuator is increased and asymptotically approaches the NPE curve. It means that the IDE actuator can be designed to have larger deflection than the TBE actuator.

The comparison between the IDE and the TBE actuator at the same opening radius $R_i/R_o = 0.44$ is presented in Fig.3.10a. For both cases of the pitch length, the IDE actuator gives larger deflection than the TBE actuator when a/T is higher than 0.5. The higher gap to pitch ratio enables larger deflection. The deflection is smaller if the pitch is small. This can be attributed to the non-uniform electric field penetration inside the piezoelectric layer.

Fig.3.10b compares the plate actuators at different values of the piezoelectric layer thickness. In the TBE actuator case, the maximum plate deflection increases almost linearly as the piezoelectric thickness is increased. The IDE actuator at a fixed gap to pitch ratio $a/T = 0.8$ is analysed, the maximum deflection increase if the piezoelectric layer thickness is increased. However, the slope of the curve observe a reduction when piezoelectric layer thickness is increased. The slope has smaller value if the pitch is small. This phenomenon can be attributed to the non-uniform field inside the piezoelectric layer with IDE on top. For the whole range of the investigated piezoelectric layer thickness, the IDE actuator has higher deflection than the TBE actuator. For instance, if the piezoelectric thickness is 2 μm, IDE can be designed to have 20 - 50% larger deflection than the TBE actuator.

4 Electrode configurations for microactuators

4.1 The electrode configurations

Both longitudinal and transversal coupling causes the actuator to bend as observed in Section 2. With the same electric field strength, the actuators deflect differently

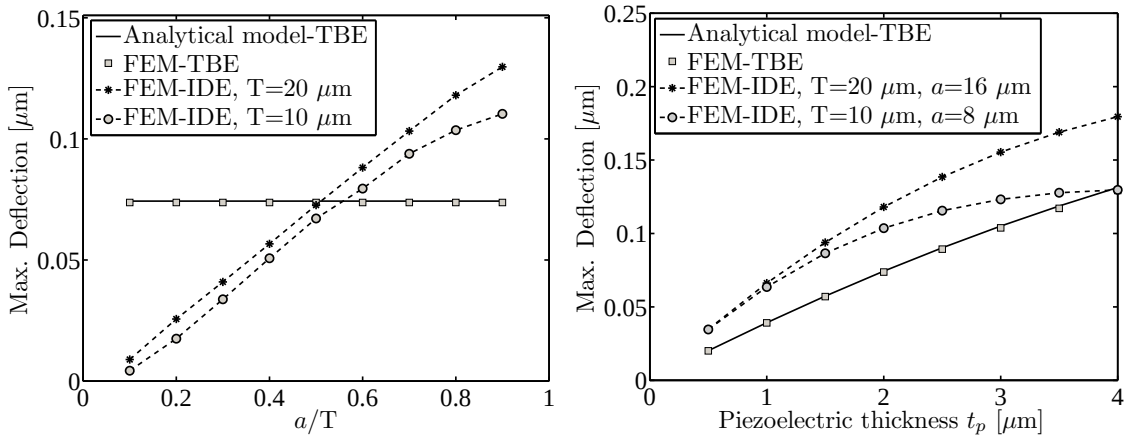

(a) (b)

Figure 3.10: Comparison of the maximum deflection between the IDE and TBE actuators at (a) t_p= 2 μm and (b) $0 < t_p \leq 4\mu$m.

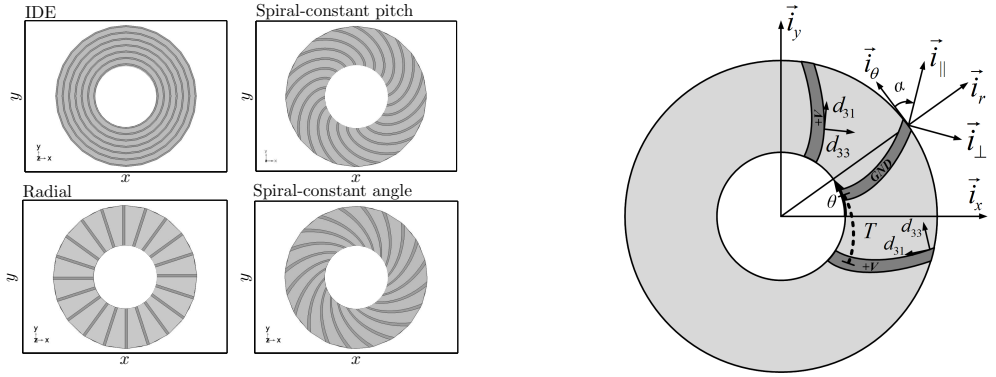

(a) (b)

Figure 3.11: (a) Four electrode configurations, (b) The polarization direction inside the spiral configuration, d_{33} coupling, is oriented differently in a same piezoelectric sheet.

for different coupling. Therefore, it is a motivation for further investigation on the effects of other coupling to the actuation.

In this section, different types of electrode configurations, see Fig.3.11a, are investigated. The spirals (constant pitch and angle), which are motivated by the design of piezoelectric torsion actuators [133], and the radial electrodes are expected to produce a mix of longitudinal and transversal direction coupling. No electrical interconnect lines are included in the micro-actuator models because of our focus on conceptual matters in this study.

In polar coordinates (r, θ), the spiral constant-angle and the spiral constant-pitch curves are by respectively

$$\theta_{r,n} = \frac{\ln r - \ln R_i}{\tan \alpha} + \frac{2\pi n}{N}, \; R_i < r < R_o \tag{3.61}$$

and

$$\theta_{r,n} = \frac{\sqrt{r^2 - R_i^2}}{R_i} - \cos^{-1} \frac{R_i}{r} + \frac{2\pi n}{N}, R_i < r < R_o. \tag{3.62}$$

where R_i and R_o are the inner and outer radii of the transducer, and the index

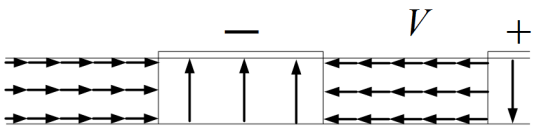

Figure 3.12: Four different polarization regions have uniform poling assumption.

$n = \{0, 1, ..., N-1\}$ is denotes the n^{th} spiral electrode. The spiral angle α is defined in Fig.3.11b. In the spiral constant-angle configuration, we set α to 45^o, which is recommended to gain the maximum shear strain [133]. In the spiral constant-pitch configuration, α is a radius-dependent parameter

$$\alpha = \sin^{-1} \frac{R_i}{r}. \tag{3.63}$$

The pitch T of these spiral curves is

$$T = \frac{2\pi r \sin \alpha}{N} \tag{3.64}$$

From (3.61)-(3.64), the radial configuration is a special case of the spiral constant-angle configuration with $\alpha = 90^o$. The pitch T of the spiral constant-pitch configuration equals $2\pi R_i/N$.

In this study, we neglected elastic properties of the thin electrode films. The piezoelectric is 2μm thick and their properties are given in Table 2.1. The electrode width b is 20μm and the actuator diameter is 3mm for all devices. The IDE device has 50% metallization or the pitch is $T = 2b = 40\mu$m. It is should be noticed that if we increase the gap to pitch ratio, the deflection and curvature of the IDE device will be further increased as shown in Fig.3.9b. The number of 50% is chosen as a conservative choice for the IDE actuator when compared with the other alternatives.

4.2 Electromechanical performance

In operation, a potential difference is then applied across neighbouring electrode fingers to create an electric field. The polarization direction follows the electric field. Hence, different electrode configurations lead to different polarization. And even within the same configuration, the polarisation vector may vary throughout the material.

The finite element method using Comsol Multiphysics is used to analyse the electromechanical properties of the device concepts. We assume that the polarization is uniform across the thickness of the piezoelectric layer as shown in Fig.3.12. The polarization direction is always perpendicular to the electrode since it is aligned with the electric field during poling.

The piezoelectric film of all the concepts can be divided into four different polarization regions. We use cylindrical coordinates (r, θ, z) as shown in Fig.3.11b. In the IDE configuration, the polarization direction is in the positive or negative z direction under respectively the negative and positive electrodes. In the regions between two neighbouring electrodes, which we refer to as active regions, the polarization is along the radial direction. Neighbouring active regions have oppositely directed polarization that is always towards the negative electrode as shown in Fig.3.12. In the spiral and radial configurations, the normal and the tangential

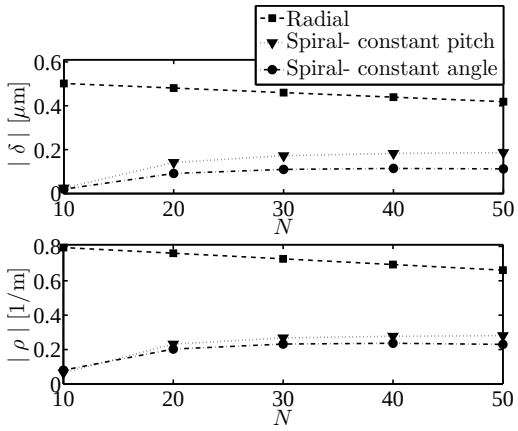

Figure 3.13: Centre deflection and curvature at sag vertex for the actuators with different values of the active region N at 1MV/m

directions with respect to the electrode are rotated an angle α as illustrated in Fig.3.11b and have unit vectors

$$\vec{i}_{\perp} = \cos(\theta - \alpha)\vec{i}_x + \sin(\theta - \alpha)\vec{i}_y, \tag{3.65}$$

$$\vec{i}_{\parallel} = -\sin(\theta - \alpha)\vec{i}_x + \cos(\theta - \alpha)\vec{i}_y. \tag{3.66}$$

Hence, the four regions have polarization directions that are in the positive or negative z or normal directions.

We compare different actuators with equal average field-strengths in the piezoelectric layers between the electrodes. For the configurations with variable electrode distances or gaps, we use the smallest gap. The average electric field is

$$\bar{E} = \frac{V}{T - b}. \tag{3.67}$$

We consider spiral and radial configurations with the same number N of active regions. Figure 3.13 presents the absolute value of the center deflection δ and curvature ρ of the bending with respect to the number of the active regions at an equal field-strength of 1MV/m. For spiral configurations, both deflection and curvature increase if N is increased. When N is large, the deflection and curvature become saturated. For the radial configuration, these quantities are slightly decreased as N is increased. Therefore, if we chose N to maximize the performance of the radial configuration, then the spiral ones will perform worse and vice versa. In our study, we choose $N = 30$ as a trade off. Then the spiral and radial configurations achieve more than 90% of their maximum displacement and curvature. We could have chosen N larger, resulting in slightly reduced performance of the radial configuration. The maximum possible value of N is limited by the available space at the inner radius R_i. A smaller N would reduce performance of the spiral configuration. Moreover, very small values of N can lead to an impractical poling process due to very large gaps.

Comparisons of performance parameters are shown in Fig.3.14a. They show that the IDE actuator produces larger deflection and curvature than the other alternatives. It is followed by the radial electrode. The spiral electrodes give the smallest vertical bending because a part of the work is made in torsional actuation.

If the actuator is configured as a micro-pump, the volume change

$$\Delta\text{Vol} = \int_y \int_x \delta(x, y)\mathrm{d}x\mathrm{d}y \tag{3.68}$$

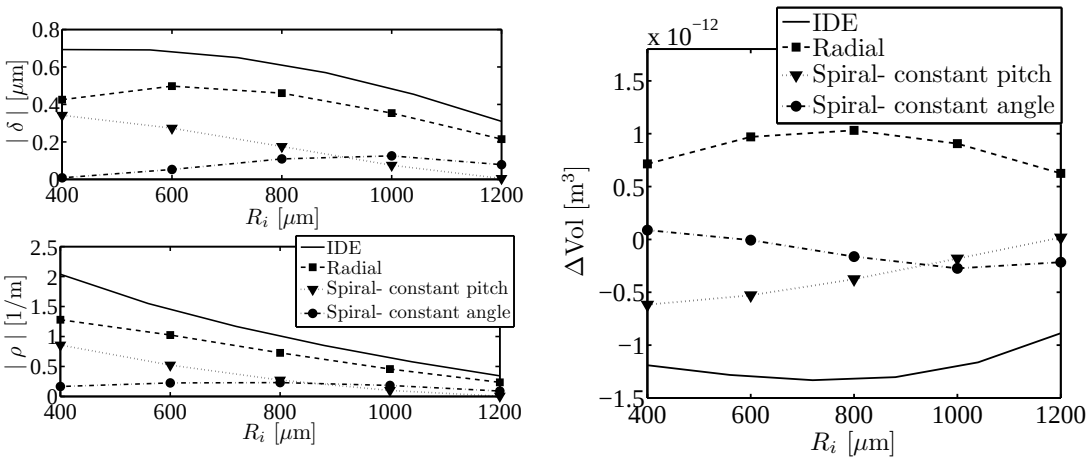

Figure 3.14: Comparison between the actuators with different electrode configuration at different opening radius R_i at 1MV/m. (a) The centre deflection and curvature at sag vertex, (b) The volume change.

is of interest.

Figure 3.14b shows that the IDE configuration has the largest volume change. It is followed by the radial and the spiral configurations. The radial configuration has opposite diection of deflection from the other alternatives, which is designated by the sign of the volume change.

Chapter 4

Conclusion

In this thesis, the modelling, simulation and characterization of piezoelectric actuators with the interdigitated electrode (IDE) configuration has been presented. Beginning with the constitutive equation for piezoelectricity, we have derived and validated models of the IDE piezoelectric actuators. The beam and plate structures have been investigated.

First, a new governing equation was derived for bending of a beam actuator with the IDE configuration. Many researchers have published the governing equation for a TBE beam. For the TBE beam structure, the material electromechanical coupling factor adds a correction term to the flexural rigidity of the entire structure. For IDE beams, we discovered that there is no need for such a correction term for either cantilever or clamped-clamped actuators if they are mechanically unloaded.

Next, the new governing equation led to the establishment of a deflection formula for the beam actuators. Under the same applied electric potential, and with the assumption of a uniform electric field, the deflection was found to be proportional to the number of the electrodes. However, if the electric field remains the same, the deflection is then proportional to the gap-to-pitch ratio. For clamped-clamped beam actuators, a model of the optimal transducer length is presented. If the piezoelectric layer is thin, then the optimal transducer lengths are equal half of the beam length for both the TBE and the IDE actuators.

Then, a general two-port model of the IDE cantilever was established. The effects of the piezoelectricity on the mechanical properties, e.g., the flexural rigidity and stiffness, and the electrical properties, e.g., the capacitance, of the IDE transducer under different stimuli were investigated. As mentioned above, when the beam is mechanically unloaded and electrically stimulated, we proved that no correction terms were needed for the flexural rigidity. However, when the beam is loaded mechanically, i.e., by a tip force, the mechanical stiffness is then affected by the electromechanical coupling factor of the piezoelectric material. However, if the piezoelectric layer is thin, this contribution is then negligible. The free capacitance and the transducer's electromechanical coupling factor are not only dependent on the dimensions and the properties of the piezoelectric layer but are also dependent on the detailed layer structure on the basis of the flexural rigidity ratio.

This thesis is then followed by an investigation of the nonuniform electric field. Normally, Laplace's equation represents the starting point for derivation of formulas for the capacitance and the electric field. However, in piezoelectric transducers, the electromechanical coupling property adds a mechanically-dependent term to the equation. For a transducer with a thin piezoelectric film, this new equation can be

simplified and transformed into Laplace's equation. The transformation shows that we can treat the piezoelectric material as an isotropic material with an equivalent permittivity and thickness.

The simplest models that can be used for the IDE configuration are the uniform-field models. The capacitance and the electric field are reciprocally proportional to the gap size. This simple estimation process always overestimates both the electric field and the capacitance. More accurate models can be produced using the conformal mapping technique. If the piezoelectric layer is thin, these models can then be simplified. The simplified models show that the capacitance and the electric field are reciprocally proportional to the sum of the gap and a correction term. This correction term is solely dependent on the piezoelectric layer thickness.

In practice, these new models of e.g., the electric field, the capacitance, and the coupling constant can be used to characterize thin film ferroelectric materials. All parasitic contributions must be subtracted from the measurement results. To do this, we introduced a phenomenological model of the parasitic capacitance. Then, the CV and PV and the stress-field loops of the material were calculated. At the peaks of the CV loops, the data spread of 9% around the average value produced when using the uniform models was reduced to less than 1% when using the new models. Almost zero coercive field spreading was observed in the PV loops. Additionally, the data spread of more than 20% for the piezoelectric coupling coefficient was reduced to less than 7%. In ferroelectric materials, we observed that the inhomogeneous permittivity distribution can be treated as an homogeneous distribution with an equivalent relative permittivity.

Bending models of the microactuators were also established for the plate-type actuators. We derived explicit formulas for the center deflections of the d_{31} and d_{33} coupling plates. From these formulas, the optimal opening radius ratios were also derived. For the d_{31} coupling plate with the TBE configuration, the optimal opening radius ratio was found to be $1/\sqrt{e}$ and was independent of the material choice. For the d_{33} coupling plate, the optimal ratio was dependent on the material choice. An analytical model was also introduced to calculate the deflection of the IDE circular plate actuator. Different electrode configurations, including interdigital, spiral, and radial configurations, were investigated for the plate actuators. Under an equal-field comparison, the IDE configuration was found to be the best for bending characteristics.

Finally, with regard to the possibility of use of the IDE concept to replace TBEs in piezoelectric tunable lenses, we compared the deflection properties of the IDE and TBE actuators with both beam and plate structures. Under equal-voltage comparison, the IDE actuators showed worse performance than the TBE devices. Under equal-electric field comparisons, however, the IDE actuators could produce higher deflections than the TBE devices. Additionally, the actuators with the IDE configuration could provide higher electromechanical coupling factors than the TBE devices. This serves as a motivation for use in a variety of different applications, including optical image stabilization, microsensors and microgenerators.

Bibliography

[1] S. D. Senturia, *Microsystem Design*. Norwell, MA, USA: Kluwer Academic Publishers, 2001.

[2] C. S. Smith, ''Piezoresistance effect in germanium and silicon,'' *Phys. Rev.*, vol. 94, pp. 42--49, Apr 1954.

[3] W. P. Eaton and J. H. Smith, ''Micromachined pressure sensors: review and recent developments,'' *Smart Materials and Structures*, vol. 6, no. 5, p. 530, 1997.

[4] R. Wood, R. Mahadevan, V. Dhuler, B. Dudley, A. Cowen, E. Hill, and K. Markus, ''MEMS microrelays,'' *Mechatronics*, vol. 8, no. 5, pp. 535 -- 547, 1998.

[5] P. Dario, R. Valleggi, M. C. Carrozza, M. C. Montesi, and M. Cocco, ''Microactuators for microrobots: a critical survey,'' *Journal of Micromechanics and Microengineering*, vol. 2, no. 3, p. 141, 1992.

[6] M. Esashi, S. Shoji, and A. Nakano, ''Normally close microvalve and micropump fabricated on a silicon wafer,'' in *Micro Electro Mechanical Systems, 1989, Proceedings, An Investigation of Micro Structures, Sensors, Actuators, Machines and Robots. IEEE*, pp. 29--34, Feb 1989.

[7] H. V. Lintel, F. V. D. Pol, and S. Bouwstra, ''A piezoelectric micropump based on micromachining of silicon,'' *Sensors and Actuators*, vol. 15, no. 2, pp. 153--167, 1988.

[8] J. Stasiak, S. Richards, and S. Angelos, ''Hewlett packard's inkjet mems technology: past, present, and future,'' in *Proc. SPIE*, vol. 7318, p. 73180U, 2009.

[9] L. Henriksen, M. Eliassen, V. Kartashov, J. H. Ulvensøen, I.-R. Johansen, K. H. Haugholt, D. T. Wang, F. Tyholdt, and W. Booij, ''Compact adjustable lens,'' Oct. 25 2011. US Patent 8,045,280.

[10] K. Haugholt, D. Wang, F. Tyholdt, W. Booij, and I. Johansen, ''Polymer lens,'' June 12 2012. US Patent 8,199,410.

[11] N. Binh-Khiem, K. Matsumoto, and I. Shimoyama, ''Polymer thin film deposited on liquid for varifocal encapsulated liquid lenses,'' *Applied Physics Letters*, vol. 93, no. 12, p. 124101, 2008.

[12] S. Shian, R. M. Diebold, and D. R. Clarke, ''Tunable lenses using transparent dielectric elastomer actuators,'' *Opt. Express*, vol. 21, pp. 8669--8676, Apr 2013.

[13] S. Y. Lee, H. W. Tung, W. C. Chen, and W. Fang, ''Thermal actuated solid tunable lens,'' *IEEE Photonics Technology Letters*, vol. 18, pp. 2191--2193, Nov 2006.

[14] N. Weber, D. Hertkorn, H. Zappe, and A. Seifert, ''Polymer/silicon hard magnetic micromirrors,'' *Journal of Microelectromechanical Systems*, vol. 21, pp. 1098--1106, Oct 2012.

[15] M.-H. Kiang, O. Solgaard, K. Y. Lau, and R. S. Muller, ''Electrostatic combdrive-actuated micromirrors for laser-beam scanning and positioning,'' *Journal of Microelectromechanical Systems*, vol. 7, pp. 27--37, Mar 1998.

[16] K. H. Koh and C. Lee, ''A two-dimensional mems scanning mirror using hybrid actuation mechanisms with low operation voltage,'' *Journal of Microelectromechanical Systems*, vol. 21, pp. 1124--1135, Oct 2012.

[17] T. Bakke, A. Vogl, O. Zero, F. Tyholdt, I.-R. Johansen, and D. Wang, ''A novel ultra-planar, long-stroke and low-voltage piezoelectric micromirror,'' *Journal of Micromechanics and Microengineering*, vol. 20, no. 6, p. 064010, 2010.

[18] R. Topliss, ''MEMS autofocus actuator,'' Apr. 29 2014. US Patent 8,711,495.

[19] C. W. Chiu, P. C. P. Chao, and D. Y. Wu, ''Optimal design of magnetically actuated optical image stabilizer mechanism for cameras in mobile phones via genetic algorithm,'' *IEEE Transactions on Magnetics*, vol. 43, pp. 2582--2584, June 2007.

[20] J. Shi, D. Ahmed, X. Mao, S.-C. S. Lin, A. Lawit, and T. J. Huang, ''Acoustic tweezers: patterning cells and microparticles using standing surface acoustic waves (ssaw),'' *Lab Chip*, vol. 9, pp. 2890--2895, 2009.

[21] X. Ding, S.-C. S. Lin, B. Kiraly, H. Yue, S. Li, I.-K. Chiang, J. Shi, S. J. Benkovic, and T. J. Huang, ''On-chip manipulation of single microparticles, cells, and organisms using surface acoustic waves,'' *Proceedings of the National Academy of Sciences*, vol. 109, no. 28, pp. 11105--11109, 2012.

[22] A. Hajati, D. Latev, D. Gardner, A. Hajati, D. Imai, M. Torrey, and M. Schoeppler, ''Three-dimensional micro electromechanical system piezoelectric ultrasound transducer,'' *Applied Physics Letters*, vol. 101, no. 25, p. 253101, 2012.

[23] O. Oralkan, A. S. Ergun, C.-H. Cheng, J. A. Johnson, M. Karaman, T. H. Lee, and B. T. Khuri-Yakub, ''Volumetric ultrasound imaging using 2-d cmut arrays,'' *IEEE Transactions on Ultrasonics, Ferroelectrics, and Frequency Control*, vol. 50, pp. 1581--1594, Nov 2003.

[24] W. C. Tang, T.-C. H. Nguyen, M. W. Judy, and R. T. Howe, ''Electrostatic-comb drive of lateral polysilicon resonators,'' *Sensors and Actuators A: Physical*, vol. 21, no. 1, pp. 328 -- 331, 1990. Proceedings of the 5th International Conference on Solid-State Sensors and Actuators and Eurosensors III.

[25] D. Senkal, M. Ahamed, A. Trusov, and A. Shkel, ''Electrostatic and mechanical characterization of 3-d micro-wineglass resonators,'' *Sensors and Actuators A: Physical*, vol. 215, pp. 150 -- 154, 2014.

[26] G. K. Ho, R. Abdolvand, A. Sivapurapu, S. Humad, and F. Ayazi, ''Piezoelectric-on-silicon lateral bulk acoustic wave micromechanical resonators,'' *Journal of Microelectromechanical Systems*, vol. 17, pp. 512--520, April 2008.

[27] A. L. Herrera-May, L. A. Aguilera-Corts, P. J. Garca-Ramrez, and E. Manjarrez, ''Resonant magnetic field sensors based on mems technology,'' *Sensors*, vol. 9, no. 10, pp. 7785--7813, 2009.

[28] M. Tabib-Azar, *Microactuators: electrical, magnetic, thermal, optical, mechanical, chemical & smart structures*, vol. 4. Springer Science & Business Media, 2013.

[29] M. Ataka, A. Omodaka, N. Takeshima, and H. Fujita, ''Fabrication and operation of polyimide bimorph actuators for a ciliary motion system,'' *Journal of Microelectromechanical Systems*, vol. 2, pp. 146--150, Dec 1993.

[30] L. Que, J.-S. Park, and Y. B. Gianchandani, ''Bent-beam electrothermal actuators-part i: Single beam and cascaded devices,'' *Journal of Microelectromechanical Systems*, vol. 10, pp. 247--254, Jun 2001.

[31] J.-S. Park, L. L. Chu, A. D. Oliver, and Y. B. Gianchandani, ''Bent-beam electrothermal actuators-part ii: Linear and rotary microengines,'' *Journal of Microelectromechanical Systems*, vol. 10, pp. 255--262, Jun 2001.

[32] J. H. Comtois, M. A. Michalicek, and C. C. Barron, ''Electrothermal actuators fabricated in four-level planarized surface micromachined polycrystalline silicon,'' *Sensors and Actuators A: Physical*, vol. 70, no. 1, pp. 23 -- 31, 1998.

[33] H. C. Nathanson, W. E. Newell, R. A. Wickstrom, and J. R. Davis, ''The resonant gate transistor,'' *IEEE Transactions on Electron Devices*, vol. 14, pp. 117--133, March 1967.

[34] R. Legtenberg, J. Gilbert, S. D. Senturia, and M. Elwenspoek, ''Electrostatic curved electrode actuators,'' *Journal of Microelectromechanical Systems*, vol. 6, pp. 257--265, Sep 1997.

[35] T. Akiyama and K. Shono, ''Controlled stepwise motion in polysilicon microstructures,'' *Journal of Microelectromechanical Systems*, vol. 2, pp. 106--110, Sep 1993.

[36] L. J. Hornbeck, ''Digital light processing: A new mems-based display technology,'' 1996.

[37] W. C. Tang, T.-C. H. Nguyen, and R. T. Howe, ''Laterally driven polysilicon resonant microstructures,'' *Sensors and Actuators*, vol. 20, no. 1, pp. 25 -- 32, 1989. A Special Issue Devoted to Micromechanics.

[38] E. J. Garcia and J. J. Sniegowski, ''Surface micromachined microengine,'' *Sensors and Actuators A: Physical*, vol. 48, no. 3, pp. 203 -- 214, 1995.

[39] L.-S. Fan, Y.-C. Tai, and R. S. Muller, ''Ic-processed electrostatic micromotors,'' *Sensors and Actuators*, vol. 20, no. 1, pp. 41 -- 47, 1989. A Special Issue Devoted to Micromechanics.

[40] M. Mehregany, S. D. Senturia, J. H. Lang, and P. Nagarkar, ''Micromotor fabrication,'' *IEEE Transactions on Electron Devices*, vol. 39, pp. 2060--2069, Sep 1992.

[41] R. Maeda, J. Tsaur, S. Lee, and M. Ichiki, ''Piezoelectric microactuator devices,'' *Journal of Electroceramics*, vol. 12, pp. 89--100, Jan 2004.

[42] J. Korvink and O. Paul, *MEMS: A practical guide of design, analysis, and applications*. Springer Science & Business Media, 2010.

[43] D. J. Bell, T. J. Lu, N. A. Fleck, and S. M. Spearing, ''Mems actuators and sensors: observations on their performance and selection for purpose,'' *Journal of Micromechanics and Microengineering*, vol. 15, no. 7, p. S153.

[44] S. Bijoyraj, T. Curtis, and L. Kam, ''Emerging challenges of microactuators for nanoscale positioning, assembly, and manipulation,'' *Journal of Manufacturing Science and Engineering*, vol. 132, no. 3, p. 141, 2010.

[45] ''IEEE standard on piezoelectricity,'' *ANSI/IEEE Std 176-1987*, 1988.

[46] J. F. Nye, *Physical properties of crystals: their representation by tensors and matrices*. Oxford university press, 1985.

[47] K. Tsubouchi, K. Sugai, and N. Mikoshiba, ''AlN material constants evaluation and SAW properties on AlN/Al2O3 and AlN/Si,'' in *1981 Ultrasonics Symposium*, pp. 375--380, Oct 1981.

[48] P. Muralt, J. Antifakos, M. Cantoni, R. Lanz, and F. Martin, ''Is there a better material for thin film BAW applications than AlN?,'' in *IEEE Ultrasonics Symposium, 2005.*, vol. 1, pp. 315--320, Sept 2005.

[49] B. A. Auld, *Acoustic fields and waves in solids, VolI*. Krieger Publishing Company, 1990.

[50] J. B. Jaffe, W. R. Cook and H. Jaffe, *Piezoelectric Ceramics*. London: Academic Press, 1971.

[51] N. Ledermann, P. Muralt, J. Baborowski, S. Gentil, K. Mukati, M. Cantoni, A. Seifert, and N. Setter, ''1 0 0-textured, piezoelectric $Pb(Zr_xTi_{1-x})O_3$ thin films for MEMS: integration, deposition and properties,'' *Sensors and Actuators A: Physical*, vol. 105, no. 2, pp. 162 -- 170, 2003.

[52] M.-A. Dubois, P. Muralt, D. V. Taylor, and S. Hiboux, ''Which PZT thin films for piezoelectric microactuator applications?,'' *Integrated Ferroelectrics*, vol. 22, no. 1-4, pp. 535--543, 1998.

[53] J. Yin, B. Jiang, and W. Cao, ''Elastic, piezoelectric, and dielectric properties of $0.955Pb(Zn_{1/3}Nb_{2/3})O_3 - 0.45PbTiO_3$ single crystal with designed multidomains,'' *IEEE Transactions on Ultrasonics, Ferroelectrics, and Frequency Control*, vol. 47, pp. 285--291, Jan 2000.

[54] R. Zhang, B. Jiang, and W. Cao, ''Elastic, piezoelectric, and dielectric properties of multidomain $0.67Pb(Mg_{1/3}Nb_{2/3})O_3 - 0.33PbTiO_3$ single crystals,'' *Journal of Applied Physics*, vol. 90, no. 7, pp. 3471--3475, 2001.

[55] N. Chidambaram, *Advanced sol-gel processing of PZT thin films for piezoelectric MEMS structures*. PhD thesis, STI, Lausanne, 2014.

[56] C. G. Oakley and M. J. Zipparo, ''Single crystal piezoelectrics: a revolutionary development for transducers,'' in *2000 IEEE Ultrasonics Symposium. Proceedings. An International Symposium (Cat. No.00CH37121)*, vol. 2, pp. 1157--1167 vol.2, Oct 2000.

[57] N. Chidambaram, D. Balma, R. Nigon, A. Mazzalai, R. Matloub, C. S. Sandu, and P. Muralt, ''Converse mode piezoelectric coefficient for lead zirconate titanate thin film with interdigitated electrode,'' *Journal of Micromechanics and Microengineering*, vol. 25, no. 4, p. 045016, 2015.

[58] K. Uchino, *Piezoelectric Actuators and Ultrasonic Motors*. Boston, MA: Kluwer, 1996.

[59] K.-H. Kim, S.-Y. Lee, and S. Kim, ''A mobile auto-focus actuator based on a rotary vcm with the zero holding current,'' *Opt. Express*, vol. 17, pp. 5891--5896, Mar 2009.

[60] L. K. Lai, C. L. Tsai, and T. S. Liu, ''Design of compact linear electromagnetic actuator for auto-focusing in phone camera,'' *IEEE Transactions on Magnetics*, vol. 47, pp. 4740--4744, Dec 2011.

[61] ''Tlens compared to vcm.'' `http://polight.com/technology/tlens-compared-to-vcm/`.

[62] ''Oppo places order for mems cameras.'' `https://www.dpreview.com/articles/6253298840/oppo-mems-camera`.

[63] ''How does it work.'' `http://polight.com/technology/how-does-it-work/`.

[64] C. L. Stanfield, *Principles of human physiology*. Pearson Higher Ed, 2012.

[65] W. J. Smith, *Modern optical engineering*. McGraw-Hill, 2000.

[66] N. W. Hagood, R. Kindel, K. Ghandi, and P. Gaudenzi, ''Improving transverse actuation of piezoceramics using interdigitated surface electrodes,'' *Proc. SPIE*, vol. 1917, pp. 341--352, 1993.

[67] E. Hong, S. Krishnaswamy, C. Freidhoff, and S. Trolier-McKinstry, ''Micromachined piezoelectric diaphragms actuated by ring shaped interdigitated transducer electrodes,'' *Sensors and Actuators A: Physical*, vol. 119, no. 2, pp. 521 -- 527, 2005.

[68] C. Wang, Z. Wang, T.-L. Ren, Y. Zhu, Y. Yang, X. Wu, H. Wang, H. Fang, and L. Liu, ''A micromachined piezoelectric ultrasonic transducer operating in d_{33} mode using square interdigital electrodes,'' *Sensors Journal, IEEE*, vol. 7, pp. 967--976, July 2007.

[69] Y. Jeon, R. Sood, J.-H. Jeong, and S.-G. Kim, ''MEMS power generator with transverse mode thin film PZT,'' *Sensors and Actuators A: Physical*, 2005.

[70] N. Tesla, ''Electric condenser,'' Dec. 8 1891. US Patent 464,667.

[71] R. M. White and F. W. Voltmer, ''Direct piezoelectric coupling to surface elastic waves,'' *Applied Physics Letters*, vol. 7, pp. 314--316, Dec. 1965.

[72] D. P. Morgan, ''History of saw devices,'' in *Proceedings of the 1998 IEEE International Frequency Control Symposium (Cat. No.98CH36165)*, pp. 439--460, May 1998.

[73] A. V. Mamishev, K. Sundara-Rajan, F. Yang, Y. Du, and M. Zahn, ''Interdigital sensors and transducers,'' *Proceedings of the IEEE*, vol. 92, pp. 808--845, May 2004.

[74] N. F. Sheppard, D. R. Day, H. L. Lee, and S. D. Senturia, ''Microdielectrometry,'' *Sensors and Actuators*, vol. 2, pp. 263 -- 274, 1981.

[75] M. C. Zaretsky, P. Li, and J. R. Melcher, ''Estimation of thickness, complex bulk permittivity and surface conductivity using interdigital dielectrometry,'' *IEEE Transactions on Electrical Insulation*, vol. 24, pp. 1159--1166, Dec 1989.

[76] M. C. Zaretsky, J. R. Melcher, and C. M. Cooke, ''Moisture sensing in transformer oil using thin-film microdielectrometry,'' *IEEE Transactions on Electrical Insulation*, vol. 24, pp. 1167--1176, Dec 1989.

[77] N. J. Goldfine, A. P. Washabaugh, J. V. Dearlove, and P. A. von Guggenberg, ''Imposed $\omega - \mathrm{k}$ magnetometer and dielectrometer applications,'' *Review of Progress in Quantitative Nondestructive Evaluation*, 1993.

[78] M. E. V. Steenberg, A. Washabaugh, and N. Goldfine, ''Inductive and capacitive sensor arrays for in situ composition sensors,'' in *2001 IEEE Aerospace Conference Proceedings (Cat. No.01TH8542)*, vol. 1, pp. 1/299--1/309 vol.1, 2001.

[79] N. Goldfine, V. Zilberstein, J. S. Cargill, D. Schlicker, I. Shay, A. Washabaugh, V. Tsukernik, D. Grundy, and M. Windoloski, ''Meandering winding magnetometer array eddy current sensors for detection of cracks in regions with fretting damage,'' *Materials evaluation*, vol. 60, no. 7, pp. 870--877, 2002.

[80] E. Benes, M. Groschl, W. Burger, and M. Schmid, ''Sensors based on piezoelectric resonators,'' *Sensors and Actuators A: Physical*, vol. 48, no. 1, pp. 1 -- 21, 1995.

[81] R. Nigon, T. M. Raeder, and P. Muralt, ''Characterization methodology for lead zirconate titanate thin films with interdigitated electrode structures,'' *Journal of Applied Physics*, vol. 121, no. 20, p. 204101, 2017.

[82] S. J. Gross, S. Tadigadapa, T. N. Jackson, S. Trolier-McKinstry, and Q. Q. Zhang, ''Lead-zirconate-titanate-based piezoelectric micromachined switch,'' *Applied Physics Letters*, vol. 83, no. 1, pp. 174--176, 2003.

[83] P. Muralt, R. G. Polcawich, and S. Trolier-McKinstry, ''Piezoelectric thin films for sensors, actuators, and energy harvesting,'' *MRS Bulletin*, vol. 34, pp. 658--664, 9 2009.

[84] M. C. Zaretsky, L. Mouayad, and J. R. Melcher, ''Continuum properties from interdigital electrode dielectrometry,'' *IEEE Transactions on Electrical Insulation*, vol. 23, pp. 897--917, Dec 1988.

[85] Y. Sheiretov and M. Zahn, ''Dielectrometry measurements of moisture dynamics in oil-impregnated pressboard,'' *IEEE Transactions on Dielectrics and Electrical Insulation*, vol. 2, pp. 329--351, Jun 1995.

[86] J. Wei, ''Distributed capacitance of planar electrodes in optic and acoustic surface wave devices,'' *IEEE Journal of Quantum Electronics*, vol. 13, pp. 152--158, April 1977.

[87] O. Ramer, ''Integrated optic electrooptic modulator electrode analysis,'' *IEEE Journal of Quantum Electronics*, vol. 18, pp. 386--392, Mar 1982.

[88] H.-D. Wu, Z. Zhang, F. Barnes, C. M. Jackson, A. Kain, and J. D. Cuchiaro, ''Voltage tunable capacitors using high temperature superconductors and ferroelectrics,'' *IEEE Transactions on Applied Superconductivity*, vol. 4, pp. 156--160, Sept 1994.

[89] S. S. Gevorgian, T. Martinsson, P. L. J. Linner, and E. L. Kollberg, ''Cad models for multilayered substrate interdigital capacitors,'' *IEEE Transactions on Microwave Theory and Techniques*, vol. 44, pp. 896--904, Jun 1996.

[90] R. Igreja and C. Dias, ''Analytical evaluation of the interdigital electrodes capacitance for a multi-layered structure,'' *Sensors and Actuators A: Physical*, vol. 112, no. 23, pp. 291 -- 301, 2004.

[91] K. Prume, S. Hoffmann, and R. Waser, ''Finite element simulations of interdigital electrode structures on high permittivity thin films,'' *Integrated Ferroelectrics*, vol. 32, no. 1-4, pp. 63--72, 2001.

[92] C. R. Bowen, L. J. Nelson, R. Stevens, M. G. Cain, and M. Stewart, ''Optimisation of interdigitated electrodes for piezoelectric actuators and active fibre composites,'' *Journal of Electroceramics*, vol. 16, pp. 263--269, Jul 2006.

[93] R. Paradies and B. Schläpfer, ''Finite element modeling of piezoelectric elements with complex electrode configuration,'' *Smart Materials and Structures*, vol. 18, no. 2, p. 025015, 2009.

[94] R. R. Knight, C. Mo, and W. W. Clark, ''MEMS interdigitated electrode pattern optimization for a unimorph piezoelectric beam,'' *Journal of Electroceramics*, vol. 26, no. 1, pp. 14--22, 2011.

[95] A. Toprak and O. Tigli, ''Interdigitated-electrode-based mems-scale piezoelectric energy harvester modeling and optimization using finite element method,'' *IEEE Transactions on Ultrasonics, Ferroelectrics, and Frequency Control*, vol. 60, pp. 2162--2174, Oct 2013.

[96] C. Mo, S. Kim, and W. W. Clark, ''Theoretical analysis of energy harvesting performance for unimorph piezoelectric benders with interdigitated electrodes,'' *Smart Materials and Structures*, vol. 18, no. 5, p. 055017, 2009.

[97] E. Tadmor and G. Kosa, ''Electromechanical coupling correction for piezoelectric layered beams,'' *Microelectromechanical Systems, Journal of*, vol. 12, pp. 899--906, Dec 2003.

[98] J. G. Smits and W. Choi, ''The constituent equations of piezoelectric heterogeneous bimorphs,'' *IEEE Transactions on Ultrasonics, Ferroelectrics, and Frequency Control*, vol. 38, pp. 256--270, May 1991.

[99] J. G. Smits, S. I. Dalke, and T. K. Cooney, ''The constituent equations of piezoelectric bimorphs,'' *Sensors and Actuators A: Physical*, vol. 28, no. 1, pp. 41 -- 61, 1991.

[100] T. Ikeda, *Fundamentals of piezoelectricity*. Oxford University Press, 1990.

[101] M. Weinberg, ''Working equations for piezoelectric actuators and sensors,'' *Microelectromechanical Systems, Journal of*, vol. 8, pp. 529--533, Dec 1999.

[102] S. K. Kaldor and I. C. Noyan, ''Differentiating between elastically bent rectangular beams and plates,'' *Applied Physics Letters*, vol. 80, no. 13, pp. 2284--2286, 2002.

[103] S. R. Swanson, ''Anticlastic effects and the transition from narrow to wide behavior in orthotropic beams,'' *Composite Structures*, vol. 53, no. 4, pp. 449 -- 455, 2001.

[104] Q.-M. Wang, X.-H. Du, B. Xu, and L. E. Cross, ''Electromechanical coupling and output efficiency of piezoelectric bending actuators,'' *IEEE Transactions on Ultrasonics, Ferroelectrics, and Frequency Control*, vol. 46, pp. 638--646, May 1999.

[105] W. Liao, W. Liu, Y. Zhu, Y. Tang, B. Wang, and H. Xie, ''A tip-tilt-piston micromirror with symmetrical lateral-shift-free piezoelectric actuators,'' *IEEE Sensors Journal*, vol. 13, no. 8, pp. 2873--2881, 2013.

[106] P. Ramesh, S. Krishnamoorthy, S. Rajan, and G. N. Washington, ''Fabrication and characterization of a piezoelectric gallium nitride switch for optical mems applications,'' *Smart Materials and Structures*, vol. 21, no. 9, p. 094003, 2012.

[107] B. Svardal, T. Spatcheck, and V. Kartashov, ''Device for providing stabilized images in a hand held camera,'' June 30 2011. US Patent App. 12/776,288.

[108] C. H. Nguyen, M. A. Farghaly, M. N. Akram, U. Hanke, and E. Halvorsen, ''Electrode configurations for layered-plate piezoelectric micro-actuators,'' *Microelectronic Engineering*, vol. 174, pp. 59 -- 63, 2017.

[109] K. Prume, P. Muralt, F. Calame, T. Schmitz-Kempen, and S. Tiedke, ''Piezoelectric thin films: evaluation of electrical and electromechanical characteristics for mems devices,'' *IEEE Transactions on Ultrasonics, Ferroelectrics, and Frequency Control*, vol. 54, pp. 8--14, January 2007.

[110] A. Mazzalai, D. Balma, N. Chidambaram, R. Matloub, and P. Muralt, ''Characterization and fatigue of the converse piezoelectric effect in PZT films for MEMS applications,'' *Journal of Microelectromechanical Systems*, vol. 24, no. 4, pp. 831--838, 2015.

[111] C. H. Nguyen, U. Hanke, and E. Halvorsen, ''Actuation of piezoelectric layered beams with d_{31} and d_{33} coupling,'' Unpublished.

[112] S. Sherrit, H. D. Wiederick, and B. K. Mukherjee, ''Complete characterization of the piezoelectric, dielectric, and elastic properties of motorola PZT3203HD, including losses and dispersion,'' 1997.

[113] I. S. Gradsbteyn and I. M. Ryzbik, *Table of Integrals, Series, and Products*. Academic Press, 2000.

[114] W. Hilberg, ''From approximations to exact relations for characteristic impedances,'' *IEEE Transactions on Microwave Theory and Techniques*, vol. 17, no. 5, pp. 259--265, 1969.

[115] E. Weber, *Electromagnetic Theory: Static fields and their mapping*. Dover Publications, Inc., New York, 1965.

[116] C. H. Nguyen, R. Nigon, T. Raeder, U. Hanke, E. Halvorsen, and P. Muralt, ''Probing-models for interdigitated electrode systems with ferroelectric thin lms,'' Unpublished.

[117] P. W. Cattaneo, ''Capacitances in micro-strip detectors: A conformal mapping approach,'' *Solid-State Electronics*, vol. 54, no. 3, pp. 252 -- 258, 2010.

[118] T. M. Raeder, ''Self-poling and ageing in PZT thin films with interdigitated electrodes,'' Master's thesis, NTNU, Norway, 2015.

[119] W. Hassenpflug, ''Elliptic integrals and the Schwarz-Christoffel transformation,'' *Computers and Mathematics with Applications*, vol. 33, no. 12, pp. 15 -- 114, 1997.

[120] G. G. Stoney, ''The tension of metallic films deposited by electrolysis,'' vol. 82, no. 553, pp. 172--175, 1909.

[121] J. Reddy, *Mechanics of Laminated Composite Plates: Theory and Analysis*. CRC Press, Boca Raton, 1997.

[122] M. Deshpande and L. Saggere, ''An analytical model and working equations for static deflections of a circular multi-layered diaphragm-type piezoelectric actuator,'' *Sensors and Actuators A: Physical*, 2007.

[123] S. Timoshenko and S. Woinowsky-Krieger, *Theory of Plates and Shells*. New York: McGraw-Hill, 1959.

[124] A. Ugural, *Stresses in Plate and Shells*. WCB/McGraw Hill, Boston, 1999.

[125] S. Prasad, B. V. Sankar, L. Cattafesta, S. Horowitz, Q. Gallas, and M. Sheplak, ''Two-port electroacoustic model of an axisymmetric piezoelectric composite plate,'' in *43rd AIAA/ASME/ASCE/AHS/ASC Structures, Structural Dynamics, and Materials Conference, AIAA Paper 2002-1365*, April 2002.

[126] S. A. Prasad, Q. Gallas, S. B. Horowitz, B. D. Homeijer, B. V. Sankar, L. N. Cattafesta, and M. Sheplak., ''Analytical electroacoustic model of a piezoelectric composite circular plate,'' *AIAA Journal*, vol. 44, no. 10, pp. 2311--2318, 2006.

[127] C. Mo, R. Wright, W. S. Slaughter, and W. W. Clark, ''Behaviour of a unimorph circular piezoelectric actuator,'' *Smart Materials and Structures*, vol. 15, no. 4, p. 1094, 2006.

[128] H. G. Yu, L. Zou, K. Deng, R. Wolf, S. Tadigadapa, and S. Trolier-McKinstry, ''Lead zirconate titanate MEMS accelerometer using interdigitated electrodes,'' *Sensors and Actuators A: Physical*, vol. 107, no. 1, pp. 26 -- 35, 2003.

[129] E. Hong, S. Krishnaswamy, C. Freidhoff, and S. Trolier-McKinstry, ''Micromachined piezoelectric diaphragms actuated by ring shaped interdigitated transducer electrodes,'' *Sensors and Actuators A: Physical*, vol. 119, no. 2, pp. 521 -- 527, 2005.

[130] M. C. Wapler, J. Brunne, and U. Wallrabe, ''A new dimension for piezo actuators: free-form out-of-plane displacement of single piezo layers,'' *Smart Materials and Structures*, vol. 22, no. 10, p. 102001.

[131] E. Hong, S. Trolier-McKinstry, R. Smith, S. Krishnaswamy, and C. Freidhoff, ''Design of mems PZT circular diaphragm actuators to generate large deflections,'' *Microelectromechanical Systems, Journal of*, vol. 15, pp. 832--839, Aug 2006.

[132] O. J. Myers, M. Anjanappa, and C. B. Freidhoff, ''Comparative analysis of the planar capacitor and idt piezoelectric thin-film micro-actuator models,'' *Journal of Micromechanics and Microengineering*, vol. 21, no. 3, p. 035013, 2011.

[133] G. J. Xiao, C. L. Pan, Y. B. Liu, and Z. H. Feng *Sensors and Actuators A: Physical*, vol. 227, pp. 1 -- 10, 2015.

This thesis includes five manuscripts that set the basis for the content. The journal articles are omitted from online edition due to publisher's restrictions

Article 1:
Cuong H. Nguyen, Ulrik Hanke, Einar Halvorsen, Actuation of Piezoelectric Layered Beams with d31 and d33 Coupling, accepted, IEEE Transactions on Ultrasonics, Ferroelectrics, and Frequency Control.

Article 2:
Cuong H. Nguyen, Ulrik Hanke, Einar Halvorsen, The Constitutive Equations of Piezoelectric Layered Beams with Interdigitated Electrodes, under review.

Article 3:
Cuong H. Nguyen, Robin Nigon, Trygve Raeder, Ulrik Hanke, Einar Halvorsen, Paul Muralt, Probing-models for interdigitated electrode systems with ferroelectric thin films, under review.

Article 4:
Cuong H. Nguyen, Mahmoud A. Farghaly, Muhammad N. Akram, Ulrik Hanke, Einar Halvorsen, Electrode configurations for layered-plate piezoelectric micro-actuators, In Microelectronic Engineering, Volume 174, 2017, Pages 59-63, ISSN 0167-9317.

Article 5:
Cuong H. Nguyen, Ulrik Hanke, Einar Halvorsen, Comparison of microactuators based on piezoelectric layered plates with d31 and d33 coupling, Active and Passive Smart Structures and Integrated Systems 2016, Proc. of SPIE Vol. 9799, 97991C.